HAPTIC SURGICAL AID SYSTEM WITH MAGNETORHEOLOGICAL BRAKES FOR DENTAL IMPLANTS

By

DORUK SENKAL

A dissertation/thesis submitted in partial fulfillment of
the requirements for the degree of

MASTER OF SCIENCE IN MECHANICAL ENGINEERING

WASHINGTON STATE UNIVERSITY
School of Engineering and Computer Science

DECEMBER 2009

To the Faculty of Washington State University:

The members of the Committee appointed to examine the dissertation/thesis of DORUK SENKAL find it satisfactory and recommend that it be accepted.

_____

Hakan Gurocak, Ph.D., Chair

_____

Xiaolin (Linda) Chen, Ph.D.

_____

Wei Xue, Ph.D.

ACKNOWLEDGMENT

I am deeply indepted to Dr. Hakan Gurocak, my thesis advisor, for his valuable support through my Master's studies. Not only he helped me through every step of the research with his supervision and advice, but he also helped me with matters outside the lab. I believe his guidance will be influential throughout the rest of my career.

I gratefully thank Dr. Ilhan Konukseven, my professor at the Middle East Technical University, for pointing me in the right direction while I was working for my Bachelor's Degree.

I would also like to express my sincere gratitude to Troy Dunmire and Chad Swanson for machining numerous intricate parts, and their helpful input during the manufacturing phase of this project.

Finally, my sincere appreciation and thanks are due to my family for their encouragement and continued support.

HAPTIC SURGICAL AID SYSTEM WITH MAGNETORHEOLOGICAL BRAKES FOR DENTAL IMPLANTS

Abstract

by Doruk Senkal, M.S.
Washington State University
December 2009

Chair: Hakan Gurocak

This research explored a passive haptic interface as a surgical aid tool for dental implant surgery. The placement of a dental implant is critical since mistakes can lead to permanent damage in the nerves controlling the lips, long lasting numbness and failure of the implant and the crown on it. Haptic feedback to the surgeon in real time can decrease the dependence on the surgeon's skills and experience for accurate implant positioning and increase the overall safety of the procedure. The device developed in this research is a lightweight mechanism with weight compensation. Rotary magnetorheological (MR)-brakes were custom designed for this application using the serpentine flux path concept. The resulting MR Brakes were 33% smaller in diameter than the only commercially available brake yet produces 2.7 times more torque at 10.9 Nm. Another contribution of the research was a ferro-fluidic sealing technique which decreased the off-state torque. A spherical brake as a multi-DOF actuator was also developed as a possible candidate for actuation of the wrist joint of the haptic interface. To the best of our knowledge, our design is the first ever multi-DOF spherical brake using MR fluid. The control system implemented the passive force manipulability ellipsoid as an analytical tool for force rendering to follow rigid virtual walls with the passive device. Usability experiments were conducted to drill holes with haptic feedback. The maximum average positioning error was 2.88 mm along the x-axis. The errors along the y- and z-axes were 1.9 mm and 1.16 mm, respectively. The results are on the same order of magnitude as optical tracking systems and other dental robots, hence passive haptic devices can be considered a viable alternative to active (servo controlled) haptic devices.

TABLE OF CONTENTS

Page

LIST OF TABLES

LIST OF FIGURES

CHAPTER 1

INTRODUCTION

Dental implants have become a routine procedure in prosthetic dentistry to replace missing teeth (Figure 1.1). With the use of dental implants, a patient with missing teeth has a chance to gain the full functionality of his teeth without having to sacrifice aesthetics.

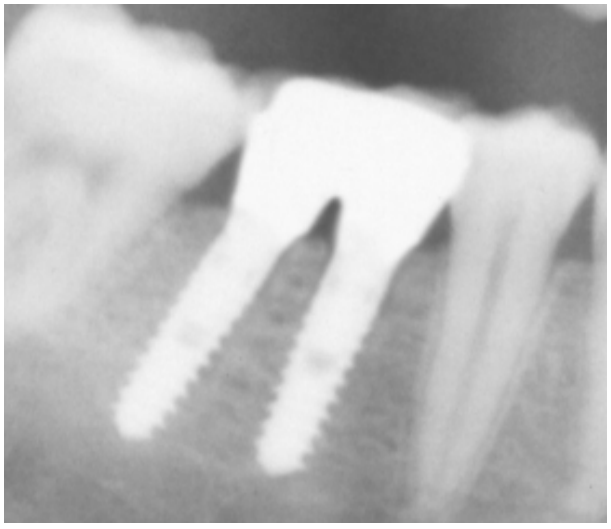

Figure 1.1. X-Ray image of two dental implants.

A successful procedure results in osseointegration of the implant and an acceptable prosthodentic outcome [1]. To achieve these outcomes, the implant must not damage critical structures, namely mandibular nerve in the lower jaw (Figure 1.2) and scheiderian membrane of the maxillary sinus in the upper jaw. When implants are placed too close to the mandibular nerve, permanent nerve damage in different peripheral nerves may occur [2, 3]. This is a very serious concern as it can lead to permanent damage in

the nerves controlling the lips. It can also result in long lasting paraesthesia (tingling, pricking and numbness feeling). [2-6].

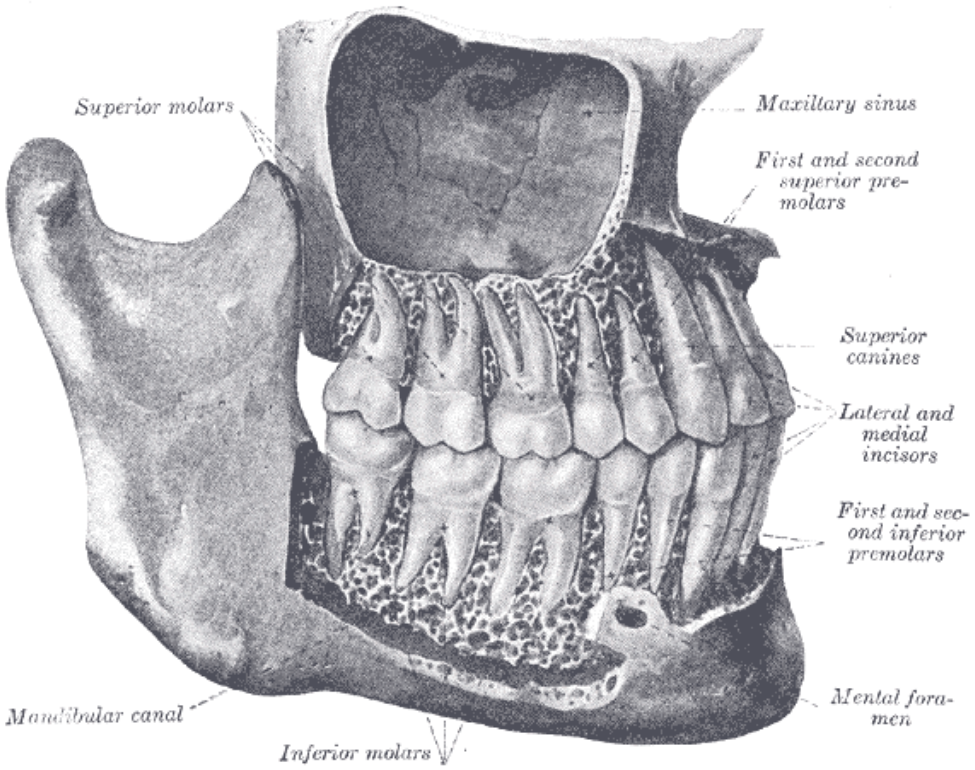

Figure 1.2. Mandibular canal with Mandibular Nerve [7]

The placement of the implant must also allow enough bone structure at the bottom and sides of it for proper support [8]. After the implant is in place, a crown is mounted on it during prosthetic treatment to achieve the desired aesthetic affect [9]. If the implant is not accurately placed, then the crown cannot be aligned properly. Over time the implant and the crown cannot support the loads put on them.

Systems for guiding the implantologist can provide additional safety. One approach is to use templates. However, they have significant shortcomings. Conventionally fabricated templates which are based on wax model of the patient's teeth

structure do not take the thickness of the mucosa, topography of the underlying bone or vital anatomical structures into consideration. In addition, limitations of current fabrication techniques do not allow fabrication of a template that remains stable during surgery [10]. Hence, they can only be used to optimize the position of the implants for later prosthodontics treatment. For this reason methods that use templates based on volume image data (Figure 1.3a) have recently been developed [11, 12]. These methods usually use volume image data of the patient's underlying jaw structure-obtained through computer tomography (CT) or digital volume tomography (DVT). Advanced manufacturing techniques, such as stereo-lithography, together with specialized implant planning software [13] are used to manufacture drilling templates [14]. Although these templates take the hidden anatomy into consideration and significant improvement in placement accuracy is reported, they suffer from high costs of CAD/CAM processing [15] and added lead time. In addition, they lack flexibility, as any change in the planning requires the manufacturing of new templates [8].

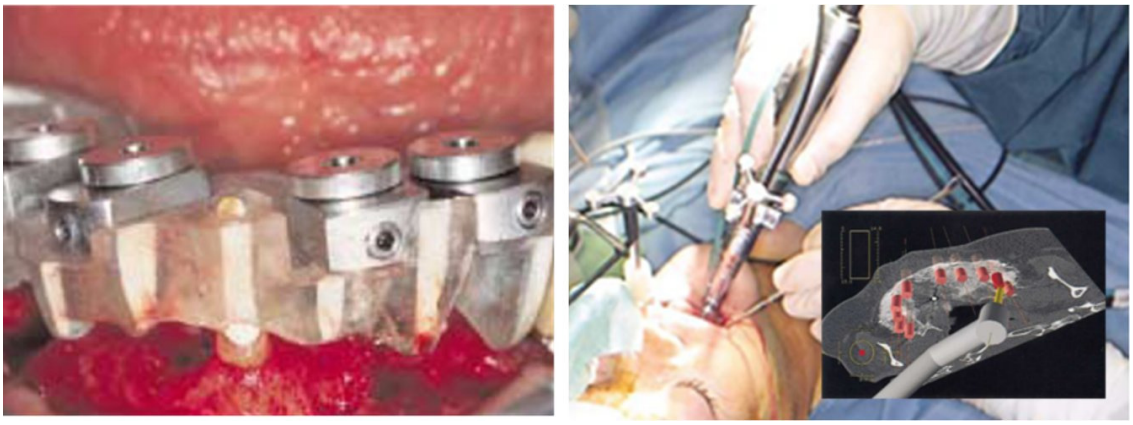

(a) (b)

Figure 1.3. (a) Computer milled surgical template [14]. (b) Opto-electronic sensors with light emitting diodes on the hand-piece with Graphical User Interface of the system [16].

Another method for implant placement uses Image Guidance Implantology systems (IGI) [17, 18]. These systems use optical sensors with light emitting diodes (Figure 1.3b), attached to the hand-piece of the drill and to the patient to track their relative positions. Combining this information with the volume data of the patient's jaw structure makes it possible to view the preoperative planning together with the drill position in real-time. Using these systems intra-operative safety can be increased as critical anatomic structures such as nerves can be avoided with the aid of the graphical user interface from the system [16]. However, even with the help of the graphical user interface, it is difficult to achieve proper position and angulation as random factors such as trembling cannot be eliminated without the guidance of a mechanical system. Errors as high as 1.23 ± 0.28 mm on average and a maximum of 1.87 ± 0.47 mm between the planned position of the fiducial point marker have been reported [19]. For this reason, the quality of the intervention is still largely dependent on the surgeon's skills and experience [1].

A surgical robot system for maxillofacial surgery [20] has been developed. With this system the surgeon interactively programs the robot during the surgery after which the robot performs the pre-programmed tasks. A haptic system for bone drilling has also been developed [21]. This system uses a PHANToM Haptic Device [22] for "virtual" bone drilling. The system was intended for training and not for actual surgery. The average misalignment was reported to be less than 0.2 mm, indicating that the system is potentially applicable to oral implant surgery. A robotic assistant for dental implantology was built which used a robot arm and CT scans to hold a drill guide over a phantom jaw [23, 24]. Deviations of approximately 1 to 2 mm were obtained using this system.

1.1 Passive Haptic Interface

Due to the complexity of the anatomic structure and the procedure, a surgical aid system for dental implants is highly desirable to ensure the success of the procedure. Such a system can decrease the dependence on surgeon's skills and experience for implant position accuracy, and increase the overall safety of the procedure. The system would track the surgeon's hand-piece and the patient to provide graphical user interface and haptic feedback to the surgeon in real time to guide him during the operation.

In this research we explored a passive haptic interface to be used in such a surgical aid system for dental implants (Figure 1.4). The interface uses magnetorheological (MR) fluid brakes as they are inherently safe and have excellent characteristics in providing rigid interaction forces to the user.

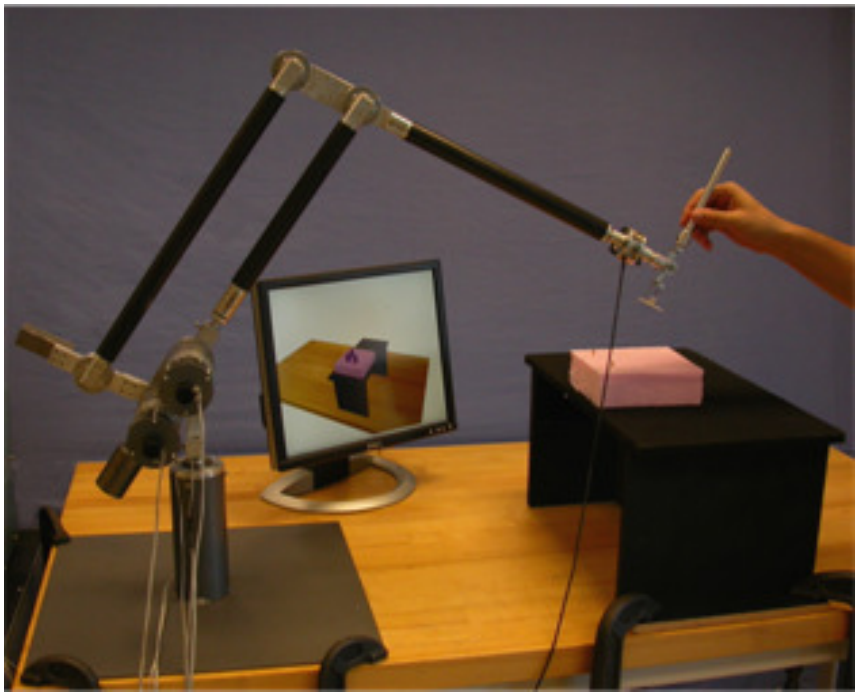

Figure 1.4. Passive Haptic Interface

We developed a new rotary MR brake as the actuator for the dental haptic interface (Figure 1.5). The new brake uses a serpentine magnetic flux path which leads to a more compact brake design. Our prototype brake has 63.5 mm diameter and 10.9 Nm torque at 1.5 A current input. Another contribution of the research is a ferro-fluidic seal. In general, MR brakes use O-rings to prevent leakage of the fluid. The O-Ring increases the off-state friction of the brake. In our design we used a ferro-fluidic sealing technique which reduced the off-state torque and sealed the fluid.

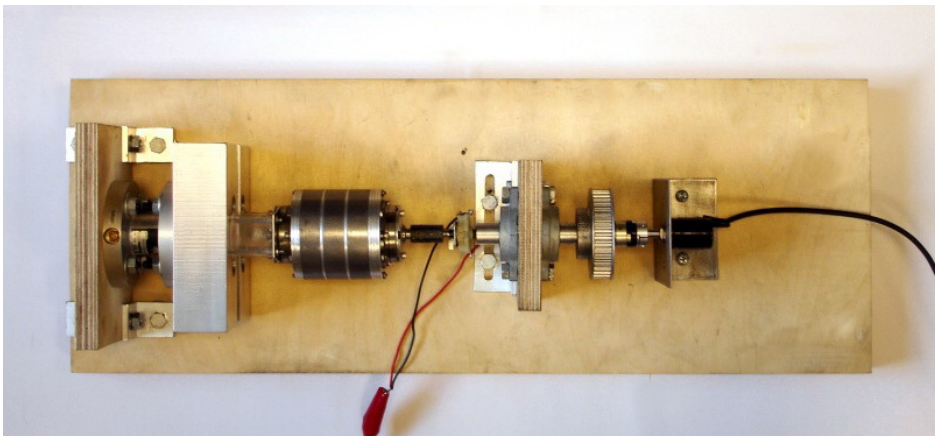

Figure 1.5. Experiment setup for rotary MR brake

All MR actuators are single degree-of-freedom (DOF). The wrist joint of the passive haptic interface is a 3 DOF spherical joint, with individual yaw, pitch and roll axis. In order to create a 3-DOF spherical joint three rotational MR brakes are needed in a gimbal arrangement. In this configuration, the resulting mechanism is usually rather large. In this research we explored design of a MR spherical brake as a multi-DOF actuator (Figure 1.6). Unlike the single-DOF brakes, the spherical brake allows motion about any arbitrary axes. When it is activated, it can restrict or lock all three DOFs

simultaneously. To the best of our knowledge, our design is the first ever multi-DOF spherical brake using MR fluid [25].

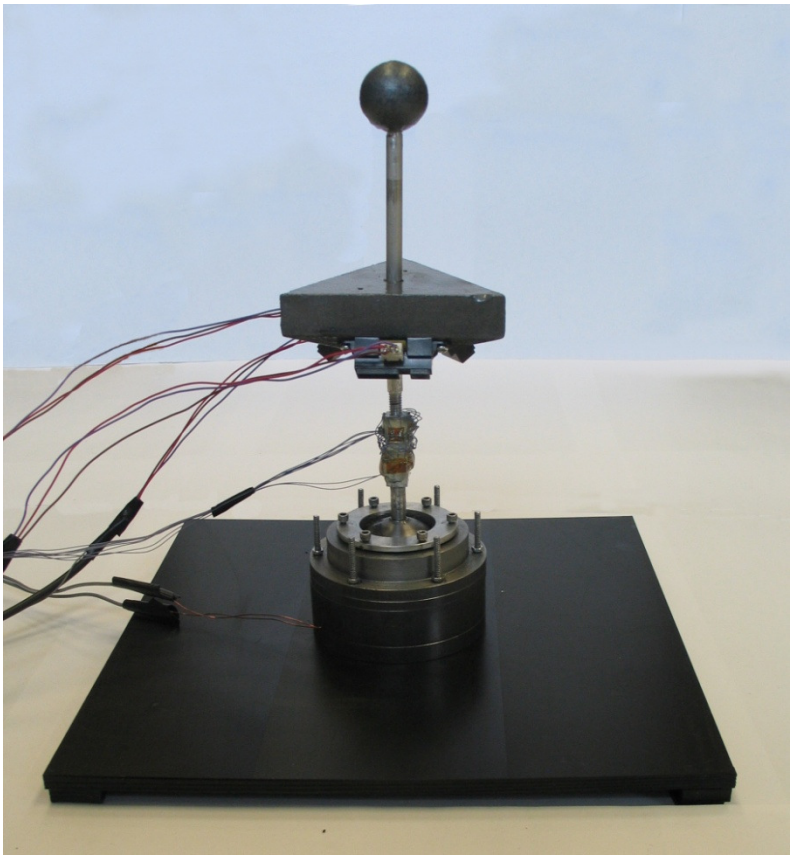

Figure 1.6. Spherical MR brake

The MR spherical brake has a diameter of 76.2 mm and can apply up to 3.7 Nm braking torque. Another contribution of the research is an optical position measurement system that eliminates the gimbal mechanisms that are typically used in spherical joints for position measurement.

In the following sections, a review of the relevant studies in the literature is provided for MR Brakes.

1.1.1 MR Brakes

MR brakes create braking torque by changing the viscosity of the MR fluid inside the brake. In the inactive state the fluid has a viscosity similar to low-viscosity oil. Upon activation with a magnetic flux, it changes to a thick consistency similar to peanut butter. MR brakes are used in many applications including prosthetics, automotive, vibration stabilization and haptics.

The MR brakes provide quick response with simple control. When used alone or in combination with motors, MR brakes have been shown to provide realistic rigid virtual object simulations in haptics applications [26-29]. However, to obtain significant braking forces/torques, the brakes are required to be rather large and use high input current. There is a commercially available MR brake by Lord Corporation [30]. This brake (model RD-2087-01) has 96.6 mm diameter, 43.7 mm width and can provide 4 Nm torque with 1.5 A current input. An MR brake was designed as a clutch for automotive applications [31]. The clutch had 152 mm diameter and required 4 A to generate a braking torque of 6.9 Nm. A single-disk MR brake was designed for haptic rendering [32]. The brake had a diameter of about 80 mm. It was smaller than some of the other examples in literature but could only provide 1.4 Nm torque in spite of the 4 A input current. Another single-disk MR brake with about 130 mm diameter was designed and experimentally tested [33]. This brake provided 1.4 Nm maximum braking torque at 0.75 A input current. To improve the performance of MR brakes a design optimization method using Finite Element Analysis was proposed [34]. The method resulted in 25% height reduction leading to a brake with 120 mm diameter and 38 mm height. At 5 A input current the brake provided 4.25 Nm torque output.

1.1.2 Spherical MR Brake

A two-DOF joystick was developed for haptics applications [35]. The design integrated two one-DOF MR disc brakes into a joystick using a gimbal mechanism. The MR disc brakes had 78 mm diameter. The overall prototype joystick had a base of about 160 mm × 160 mm and provided up to 10 Nm braking force to the joystick handle. Another multi-DOF device was designed using two groups of MR actuators to simulate virtual forces in 2D [36]. The system used four MR rotary brakes each with 170 mm diameter and 10 mm height. The overall system size was 630 mm × 540 mm × 970 mm. The maximum output torque on the handle was 10 Nm. Two other multi-DOF devices were reported that used electrorheological (ER) fluids. The first device used both clutch and brake mechanisms to achieve active and passive force feedback [37]. The device integrated four AC motors with a spherical ER joint at the center. The spherical joint assembly had an estimated diameter of 110 mm. When the motors were included, the system took up about 45 cm × 45 cm area. A complex controller was implemented resulting in about 7 N force output on the joystick handle from the spherical joint. The second device consisted of a metal sphere which was concentrically mounted in a metal half sphere [38]. The gap between them was filled with ER fluid. The spherical joint had 102 mm diameter. At 2.8 kV/mm electric field strength, the device produced 1.2 Nm output torque.

CHAPTER 2

PROBLEM STATEMENT AND SCOPE OF RESEARCH

The long term goal is to develop a dental robot to assist in oral implant surgery. Development of a first prototype robot as an initial step towards this goal is the basis of this research. The objective is to design a lightweight robot with passive actuators to assess the advantages and limitations of such a design. The research contains four phases:

2.1 Development of Compact and Powerful Rotary MR Brakes

A dental robot that would be placed in a dentist‘s office needs to be lightweight and strong, as the surgeon already needs to work in a very limited work volume such as the patient’s mouth cavity. Actuators are one of the primary components that affect the size of a robot arm. Traditionally, DC-motors are used for controlling a haptic arm. However DC-motors usually have rather small torque-to-size ratios. For that reason, either very large motors need to be used or a very high reduction ratio needs to be employed by using transmission mechanisms such as gears or pulleys. The transmission elements add to the overall robot size as well as unwanted effects such as backlash, deflection or slippage. As MR brakes usually have several orders of magnitude higher torque to size ratios than DC-motors, a design that uses MR brakes with direct coupling to the joint axis was chosen for the haptic interface.

To the best of our knowledge, there is only one commercially available rotary MR brake in the market [31]. Although this brake provides comparably higher torque to same

sized DC-motors, it is a disc-type MR brake, along with many other MR brakes in the literature. In this research we explored the design of new type of brake based on serpentine flux path concept. Using this method we aimed to build compact yet high torque drum-type MR brakes.

Another contribution of this research was in sealing of MR fluid inside the MR brakes. Traditionally rubber seals are used to keep the MR fluid from leaking out. Although this is a perfectly viable method for MR brakes that are used in applications such as exercise equipment or automobile clutches, the friction created by such a sealing method is highly undesirable in haptics applications. Any unwanted off-state friction would reduce the back-drivability of the haptic device, effectively decreasing the realism of the haptic feedback. In this reaserch we explored an alternative sealing method called ferro-fluidic sealing. Ferro-fluidic seals are normally used for sealing the lubricants inside rotating assemblies like gearboxes, bearings etc. By placing permanent ring magnets at the two ends of the rotor shaft, we aimed to solidify the MR fluid inside the end-caps and hence prevent rest of the fluid from leaking out.

2.2 Development of a Spherical MR Brake as a Potential Wrist Mechanism

In this first prototype, the commonly used pen-based haptic devices [21] were taken as the basis. Hence, three joints were actuated with MR-brakes for creating the haptic feedback and the remaining three joints at the wrist were left un-actuated to provide motion in 6 DOF. In essence when the MR brakes are activated, the position of the base of the hand-piece is constrained, whereas the orientation of the hand-piece is not. In the future prototypes, the last 3 DOF need to be actuated if orientation also needs to be

constrained. This can be accomplished by using smaller MR brakes at the wrist. However since rotary MR brakes are 1 DOF devices, a gimbal mechanism need to be employed with 3 rotary MR brakes to create the spherical joint at the wrist. We explored another alternative, by designing a spherical MR brake. The spherical brake allows motion about any arbitrary axes. When it is activated, it restricts motion around all three DOFs simultaneously. To the best of our knowledge, this is the first ever multi-DOF spherical brake using MR fluid.

2.3 Design of the First Prototype Dental Robot

Our primary design goal is to provide haptic feedback to the surgeon through the hand-piece. Such a system does not have the usual master-slave relationship of a teleoperated system. In this case, they are collocated since the surgeon uses the hand-piece as he/she normally would and haptic feedback is added to it. By eliminating the need for a programmable robotic manipulator we aimed to obtain a high level of transparency, which is much desired in surgical procedures.

For such a system to be useful in a dental implant surgery the system must be lightweight. As the surgeon has to work inside the patient‘s mouth cavity, he/she has very limited reach. A bulky design would seriously deteriorate the surgeon’s performance. The system must also be safe. Due to the nature of the operation, any malfunction in the surgical aid system might result in catastrophic results.

With these design requirements in mind, a passive haptic interface with MR-brakes has been designed. The MR-brakes have very high torque-to-size ratio [25, 39, 40], hence they are a very good choice for a lightweight design. Since MR-brakes are

passive devices they are inherently safe. They cannot add energy into the system, but can only dissipate it. They have excellent wall collision characteristics enabling near rigid interaction forces to be delivered to the hand-piece. They do not require sophisticated controllers.

2.4 Integration with the virtual reality environment and controller

As in other pen-based haptic devices, the user interacts with the virtual environment by grasping the hand-piece and moving it. The base of the hand-piece (center of the gimbal mechanism at the wrist joint) is represented by a point in the virtual environment. The device creates the haptic feedback by selectively locking the MR brakes. The resulting resistance forces are used to render virtual surfaces.

As MR brakes can only apply forces opposing the user's motion, traditional control algorithms for haptics cannot be used for the control of MR-brakes. For this reason a two-tiered control algorithm has been implemented in this research. First, required output forces based on the position of the haptic arm are calculated using a penalty based haptic renderer [41, 42]. Later these command forces are passed through a force approximation algorithm to create the closest force output that can be obtained by using MR brakes [43, 44]. This way haptic feedback of tasks such as wall following could be approximated.

CHAPTER 3

MR BRAKES

3.1 Rotary MR Brake

Rotary MR brake designs have two varieties: (1) Disk type, and (2) Drum type. In these designs the braking torque is due to the shear stress of the MR fluid placed in a gap between two rotating surfaces. Often the behavior of controllable fluids is represented as a Bingham plastic having variable yield strength [33]. The flow is governed by:

$$\tau = \tau_{yd}(B) + \eta \frac{\omega \cdot r}{h} \tag{3.1}$$

where the first term is the dynamic yield stress as a function of the magnetic flux. The second term is the shear strain rate with ω is the angular velocity, r is the radial position, η is the viscous friction coefficient and h is the fluid gap. In practical applications, a small torque due to friction (e.g. due to the seals) also exists as a third component in the total braking torque. The significant portion of the braking torque is from the dynamic yield stress acting on the outer surface of the rotor (Figure 3.1). In haptics applications, the brakes rotate slowly. Hence, the second term in Equation 1 is ignored. The total braking torque can then be written as:

$$T = 2\pi \cdot r^2 \cdot L \cdot \tau_{yd}(B) + T_{Coulomb} \tag{3.2}$$

where $\tau_{yd}(B)$ is the MR fluid shear stress as a function of magnetic flux and $T_{Coulomb}$ is the mechanical friction.

While the MR brakes are widely used in a variety of applications from exercise equipment to automobiles they are usually too bulky to be effectively used in haptics applications. Also, the off-state friction is an issue in their usage in haptics applications.

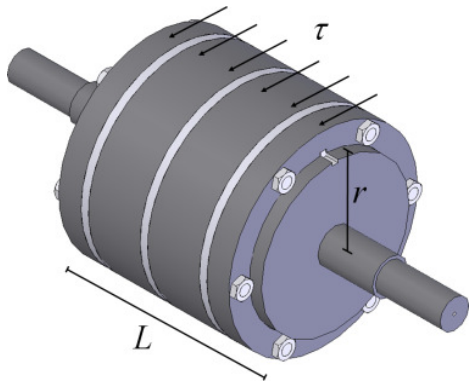

Figure 3.1. Braking torque in rotary MR brakes is a function of the dynamic shear stress on the rotor controlled by the magnetic flux.

In the existing designs only a limited area of MR fluid in the gap can be kept at the required magnetic field strength to activate the fluid. Also, since magnetic field strength is more or less inversely proportional to flux path cross-sectional area, the maximum MR fluid gap that can be actuated is limited. As a result, the only options to obtain high levels of torque are to increase the brake radius, coil windings and current. All of these options lead to a bulky design due to the size of the coil and the disk or drum.

3.1.1 Serpentine Flux Path

To design an MR brake with higher torque without increasing the size of the brake, more surface area of the MR fluid must be activated by the magnetic flux. We

achieved this by creating a serpentine flux path. By strategically placing magnetically conductive 1018 steel rings and non-conductive Aluminum rings it is possible to bend the magnetic field and weave it through the MR fluid gap multiple times (Figure 3.2). This led to a more compact brake design and enabled us to increase the braking torque without increasing the size of the brake.

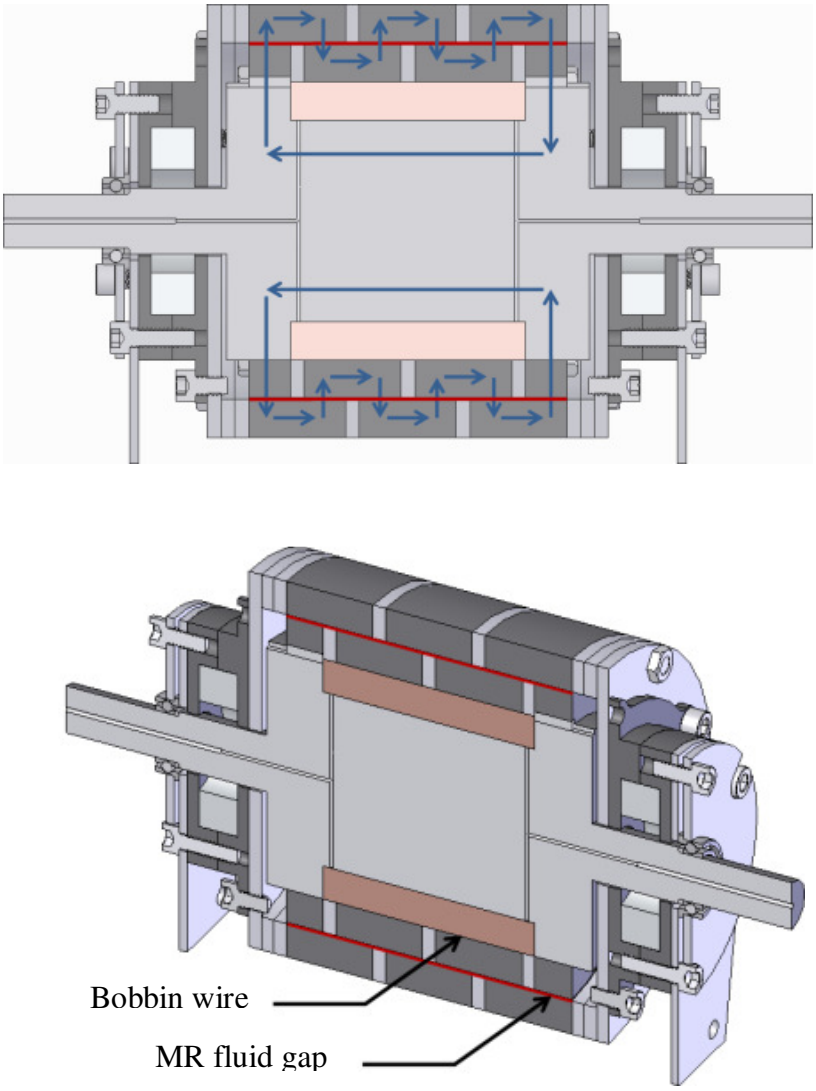

Figure 3.2. Serpentine magnetic flux path weaving through the drum and the outer shell (top). It enables activation of more of the MR fluid for increased braking torque. MR fluid between the outer shell and the rotor with the coil (bottom).

Due to the complex geometry, we modeled the brake using the MagNet Finite Element Analysis (FEA) software by Infolytica Corp. [45]. The design was optimized based on the magnetic flux density computed in the fluid gap. The goal was to maximize the flux density in the fluid, hence the braking torque, while keeping the outer diameter of the brake around 65 mm. The torque requirement was set at 10 Nm. The magnetic coil was formed by wrapping 800 turns of 26-gauge enameled magnet wire around the spool on the rotor. The MR fluid (MRF-132LD) was purchased from Lord Corp. [46]. The rotor is a solid steel part that works both as a steel core for the electromagnet and a transmission element for the torque. The magnet wire is wound into the groove on the shaft. The two ends of the magnet wire pass through tiny holes along the shaft axis to be connected to power supply.

The shear stress generated by the MR fluid is proportional to the magnetic flux through the fluid. If the number of coil turns and the current are increased, the flux will increase. However, this requires thicker wires and results in a larger coil. Using more turns of a thinner wire is possible but this time the wire overheats due to the increased current. The braking torque is also a function of the fluid gap, the drum radius and width. The smaller the gap the larger the magnetic flux in the gap since the relative permeability of the MR fluid is much smaller than that of low-carbon steel. Increasing the drum radius provides larger torque arm as the shear force is applied on the surface of the drum by the fluid. Furthermore, if the width of the drum can be increased, the total surface area where the shear stress is applied will increase. Consequently, to increase the braking torque, the fluid gap must be minimized while the number of coil turns, current, drum radius and width must be maximized.

After much iteration, the optimal design had a rotor with 52 mm radius, 47 mm length and 0.25 mm fluid gap producing an average of 1.03 Tesla flux in the MR fluid (Figure 3.3). Based on the manufacturer's specifications for the MRF-132LD fluid, the shear stress corresponding to the 1.03 Tesla flux was 55 kPa [46]. With these dimensions and the shear stress value, the maximum braking torque output for an input of 1.5A current was calculated as 10.83 Nm using equation 2. The Coulomb friction was ignored since the design incorporates ball bearings reducing the mechanical friction between the shaft and its housing down to negligible levels. This assumption was later validated in experiments.

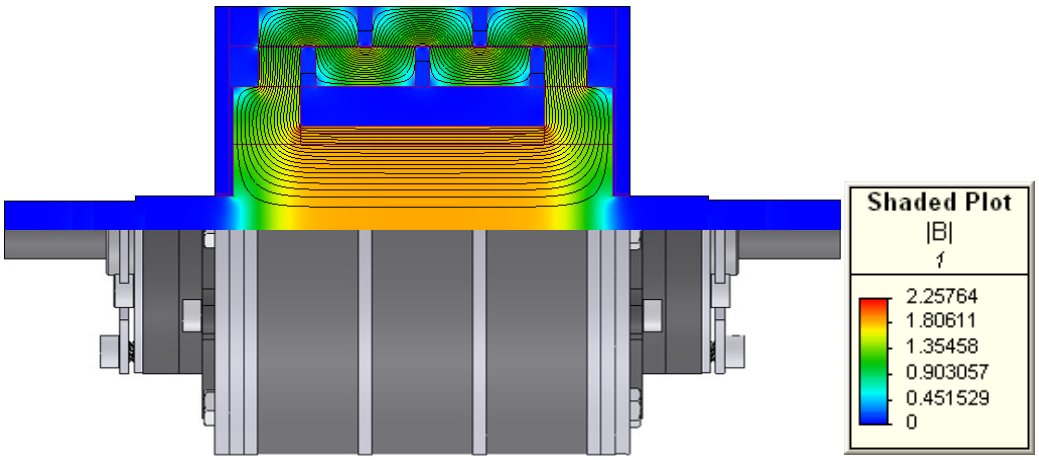

Figure 3.3. Quarter sectional view of the MR-Brake showing the serpentine magnetic flux using FEM analysis.

3.1.2 Ferro-fluidic Sealing

MR brakes usually employ an O-ring between the rotor and stator to seal the fluid in. Although this is an effective mechanism to prevent fluid leakage, the O-Rings increase the off-state friction of the MR brake. The off-state friction is an important parameter for haptic applications. Furthermore, the MR fluid has been shown to be very

abrasive on the O-rings. In this research, we developed a novel sealing approach using ferro-fluidic sealing assemblies on both sides of the brake shaft (Figure 3.4). The ferro-fluidic sealing assemblies have three primary roles in the brake assembly: (1) Prevent the leakage of the MR fluid, (2) hold the roller bearings necessary to keep the shaft in place, and (3) connect the chassis to a stationary point via aluminum flanges.

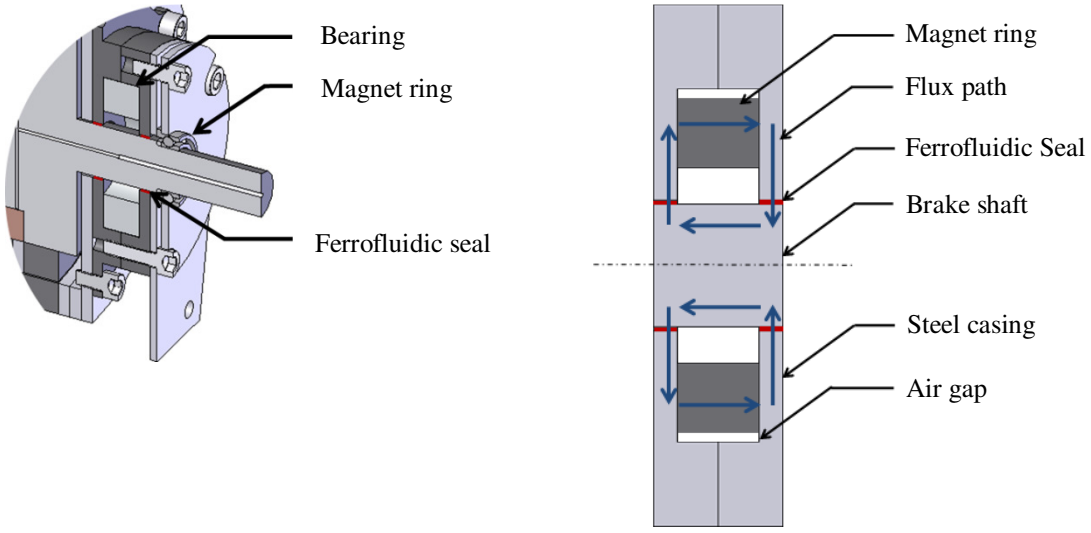

Figure 3.4. Ferro-fluidic sealing using a ring magnet (left). Ball bearing supports the rotor. Cross-sectional view of the ferro-fluidic seal and the flux path (right).

These ferro-fluidic seals work by using the MR fluid itself as a sealing element. Circular magnets placed at both ends produce magnetic flux paths that cross the gap between the shaft and the chassis (Figure 3.4). The magnetic field increases the yield stress of the MR fluid inside the gap, which builds a pressure differential that keeps the MR fluid from leaking out. As there is no active contact between solid bodies this approach helps decrease the off-state friction tremendously which is critical in haptic displays.

3.2 Spherical MR Brake

Devices that use MR fluids have several advantages over devices with ER fluids. Yield shear stress of MR fluids is much higher than ER fluids, this leads to higher torque output. The ER fluids require potential differences as high as 3 kV in order to be activated, whereas devices that use MR fluids have much lower voltage requirements usually in the range of a few volts. This becomes even more important if the device is to be used in environments, such as haptics, where human interaction will be present. Failure in a 3 kV circuit can be very dangerous to the user.

A big challenge in designing devices that use MR fluids is routing the magnetic flux path through the fluid while keeping the overall device size compact and the output torque high. Both in ER and MR fluids the fields that are applied to the fluid must be perpendicular to the fluid gap. This requirement is satisfied easily with ER devices as applying a potential difference between any two surfaces would automatically create electric fields perpendicular to those two surfaces hence also perpendicular to the ER fluid in the gap. With MR brakes it is more difficult since a coil for an electromagnet must be housed in the brake and the resulting flux path must be guided through the fluid by carefully designing the magnetic circuit.

Previously we designed single DOF rotary, compact and powerful MR brakes using a serpentine flux path concept [39, 40]. In this approach, aluminum and steel rings were employed to weave the magnetic flux path through the MR fluid gap. This led to activation of much more of the MR fluid in the same compact volume. The same concept was adapted in the design of the MR spherical brake.

The MR spherical brake consists of four main components: (1) Steel ball, (2) Steel socket with an aluminum ring, (3) Coil, and (4) MR fluid between the ball and the socket (Figure 3.5). The aluminum ring sits on the coil. It extends into the MR fluid gap to prevent the magnetic circuit from shorting around the coil and to force it to go through the MR fluid gap. Starting near the center of the coil the magnetic flux path jumps across the MR fluid gap into the ball. Once inside the ball, it continues until it passes to the other side of the aluminum ring. On the top side of the aluminum ring it jumps across the MR fluid gap once again going back into the socket where it completes its loop back to the center of the coil. Due to the difficulty of visualizing and calculating magnetic fields in such complex geometry we used Magnet FEM software by Infolytica Corp. [45].

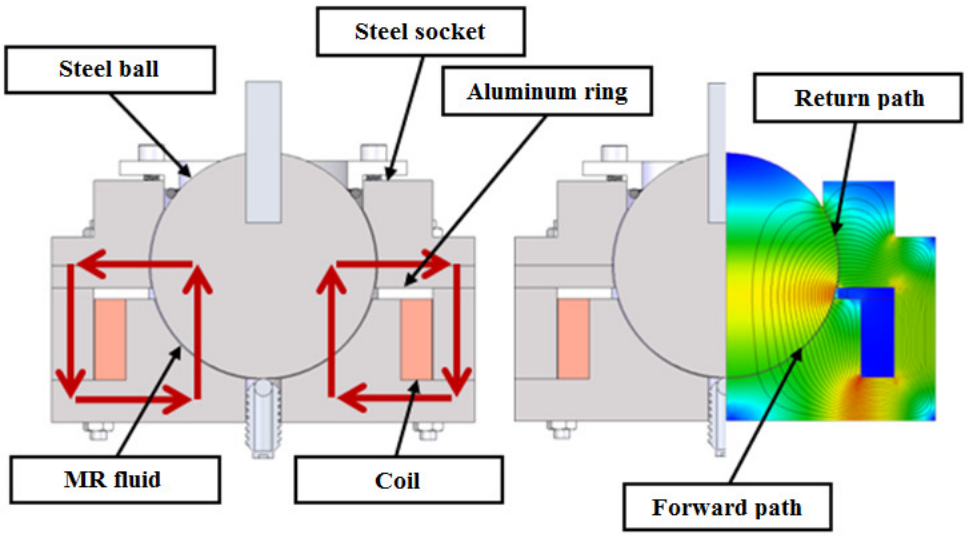

Figure 3.5. MR Spherical brake flux path (left) and FEM modeling (right).

Our primary design goal was to develop a compact multi-DOF actuator with the highest possible torque output. In order to obtain this, the MR fluid needs to be activated with a strong, homogeneous magnetic field.

The size of the magnetically conductive parts was one of the parameters conflicting with this requirement since reducing the cross-sectional area along the path of the magnetic circuit has a negative effect on the amount of magnetic flux that can pass through it. This phenomenon is also known as core saturation because the magnetic flux density in a magnetic circuit is ultimately limited by the saturation point of the magnetic material being used.

Another parameter that needed to be optimized was the homogeneity of the magnetic field across the MR fluid gap. For our design, we aimed at obtaining 1 Tesla throughout the MR fluid, which, according to manufacturer's specifications, is very close to the saturation point of the MR fluid (MRF-132LD from Lord Corp.) [46]. This helped make maximum use of the MR fluid in the gap but it also required design of a well-balanced magnetic circuit. An unbalanced magnetic circuit would cause the fluid to saturate in one part of the brake while leading to insufficient magnetic flux densities at other points. For this reason, the position of the aluminum ring along the MR fluid gap circumference is critical as it divides the surface area of the MR fluid gap to forward and return paths (Figure 3.6) which determine the ratio of magnetic flux density along these two surfaces. The magnetic flux Φ is the same at any point along the magnetic circuit:

$$\Phi_{forward} = \Phi_{return} \tag{3.3}$$

In terms of magnetic flux density "B" and the surface area "A" through which the flux flows, the same equation can be written as:

$$B_{forward} \cdot A_{forward} = B_{return} \cdot A_{return} \tag{3.4}$$

The ring must be placed at a location where the resulting surface areas on both the forward and return flux paths will allow equal flux densities on both sides. In other words, the forward and return cross-sectional areas need to be equal. To find the location of the aluminum ring the areas were computed as:

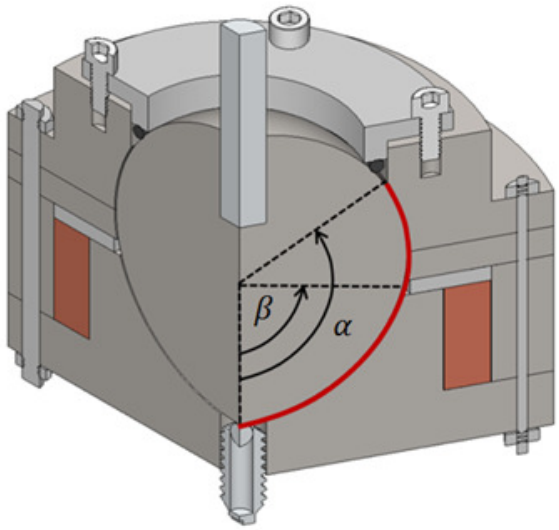

Figure 3.6. Calculating cross-sectional area for the forward and return paths.

$$\int_0^{\beta} 2\pi \cdot r^2 \cdot \sin\sigma \cdot d\sigma = \int_{\beta}^{\alpha} 2\pi \cdot r^2 \cdot \sin\sigma \cdot d\sigma \tag{3.5}$$

$$2\pi r^2(-\cos\sigma)|_0^{\beta} = 2\pi r^2(-\cos\sigma)|_{\beta}^{\alpha} \tag{3.6}$$

$$\beta = \cos^{-1}\left(\frac{1+\cos\alpha}{2}\right) \tag{3.7}$$

where β is the angle at which the aluminum ring is placed, α is the angle where the MR Fluid gap ends and "r" is the radius of the sphere. Increasing α has a positive effect on the torque output because of the increased MR fluid gap area, but at the same time it is a limiting factor for the spherical MR Brake's work volume since it reduces the motion

range of the handle attached to the ball. For this reason, first a moderate socket size of $\alpha = 120^0$ was selected. Then, $\beta = 75.5^0$ was computed as the location for the aluminum ring. Accuracy of this method was also verified using FEM. Thirteen data points inside the MR Fluid gap were taken (Figure 3.7). At 1.5 Amps 1.14 ± 0.02 Tesla was found throughout the MR Fluid gap. The flux density in the gap is fairly uniform as a result of the strategic placement of the aluminum ring.

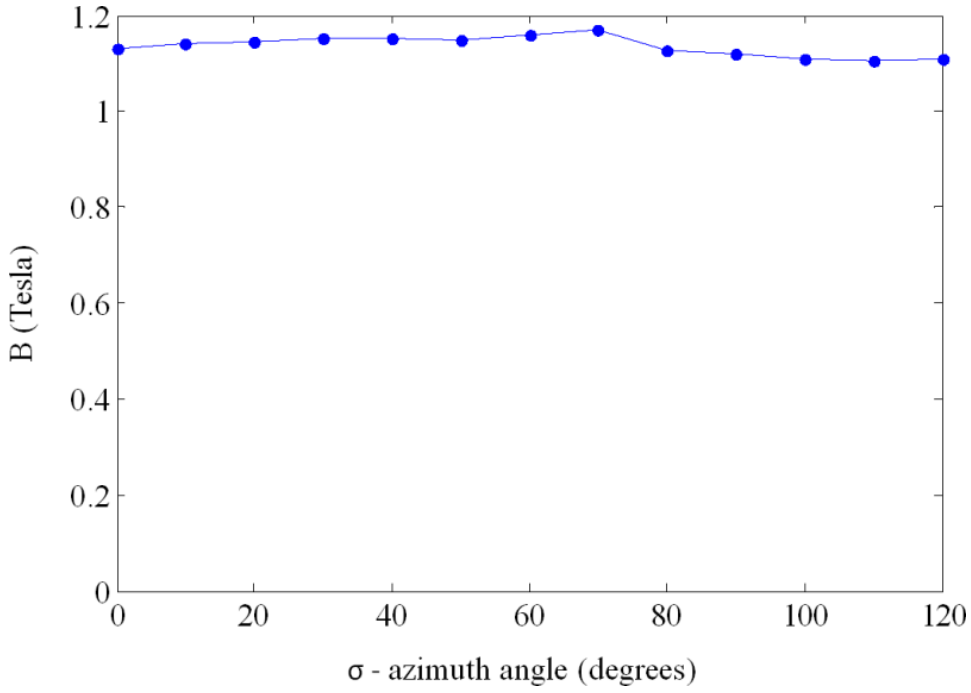

Figure 3.7. Magnetic flux density at different azimuth angles.

MR spherical brake can exert moments along all 3 axes, hence maximum torque along each axis should be individually calculated. This is accomplished by integrating the tangential component of yield stress along the ball surface for each axis. It should be noted that because of the symmetry along "z" axis, maximum torque that can be exerted along "x" and "y" axes will be equal.

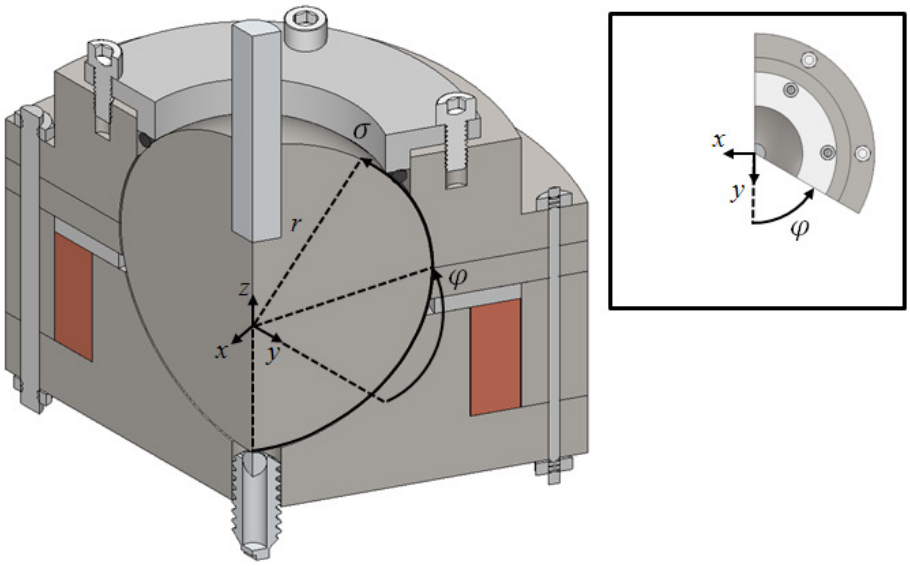

Figure 3.8. Calculating torque about the "x" and "z" axes. σ is the azimuth angle, φ is in the horizontal x-y plane.

Torque about the z-axis can be calculated by integrating shear stress on the sphere from $\sigma = 0$ to $\sigma = \alpha$ (Figure 3.8). By taking advantage of the symmetry along the z-axis, the moment arm can be written as: $r \cdot \sin\sigma$ and the shear force on an infinitesimally thick ring around the sphere can be written as: $\tau \cdot 2\pi \cdot r^2 \sin\sigma \cdot d\sigma$. Then the integral becomes:

$$T_z = \int_0^{\alpha} (r \cdot \sin\sigma) \cdot (\tau \cdot 2\pi \cdot r^2 \cdot \sin\sigma) d\sigma \tag{3.8}$$

$$T_z = \tau \cdot 2\pi \cdot r^3 \cdot \left(\frac{\sigma}{2} - \frac{\sin 2\sigma}{4}\right)\Big]_0^{\alpha} \tag{3.9}$$

Using a similar approach torque along the "x" and "y" axes can be calculated. However the absence of symmetry along the "x"-axis makes it impossible to use the above equation directly. Instead, the torque that can be created by the surface

area of the opening on the socket is subtracted from the torque that can be created by a complete sphere:

$$T_{x,y} = T_{complete} - T_{opening} \tag{3.10}$$

$T_{complete}$ can be calculated by using equation 8 with $\alpha = \pi$ to cover the whole surface area of the sphere:

$$T_{complete} = \tau \cdot \pi^2 \cdot r^3 \tag{3.11}$$

The torque that needs to be subtracted due to the opening can be calculated by a double integration over the opening. The moment arm can be written as: $\sqrt{(r \cdot \cos\sigma)^2 + (r \cdot \sin\sigma \cdot \sin\varphi)^2}$ and shear stress at any point on the opening can be written as: $\tau \cdot r^2 \cdot \sin\sigma \cdot d\varphi \cdot d\sigma$. Then, the double integral for the opening becomes:

$$T_{opening} = \int_0^{\pi-\alpha} 2 \int_0^{\pi} \tau \cdot r^3 \cdot \sin\sigma \cdot \sqrt{(\cos\sigma)^2 + (\sin\sigma \cdot \sin\varphi)^2} \cdot d\varphi \cdot d\sigma \tag{3.12}$$

Substituting into equation 9 gives:

$$T_{x,y} = \tau \cdot \pi^2 \cdot r^3 - \int_0^{\pi-\alpha} 2 \int_0^{\pi} \tau \cdot r^3 \cdot \sin\sigma \cdot \sqrt{(\cos\sigma)^2 + (\sin\sigma \cdot \sin\varphi)^2} \cdot d\varphi \cdot d\sigma \tag{3.13}$$

For $r = 20.32mm$ and $\tau_{yd}(1\ Tesla) = 55kPa$ for the fluid we used, the torque values that can be exerted by the MR Spherical Brake are found as $T_z = 3.66Nm$ and $T_{x,y} = 3.28N.m$.

Because of the r^3 term in equation 12, braking torque scales up very well with radius. Table 3.1 shows braking torques for spherical MR brakes at different sizes.

Table 3.1: Theoretical braking torques for different spherical MR brake sizes

Radius (mm)[1]	T_z (N.m)	$T_{x,y}$ (N.m)
5	0.06	0.05
10	0.44	0.39
20.32[2]	**3.66**	**3.28**
30	11.79	10.54
50	54.59	48.82

[1]: Calculations are done at $\alpha = 120°$

[2]: Prototype MR Brake

3.2.1 Force-feedback joystick with MR spherical brake

The MR spherical brake was used in the design of a force feedback joystick for haptics applications (Figure 3.9). The joystick handle, equipped with force sensing, was attached to the spherical MR-brake. An optical position measurement system was also attached to the handle.

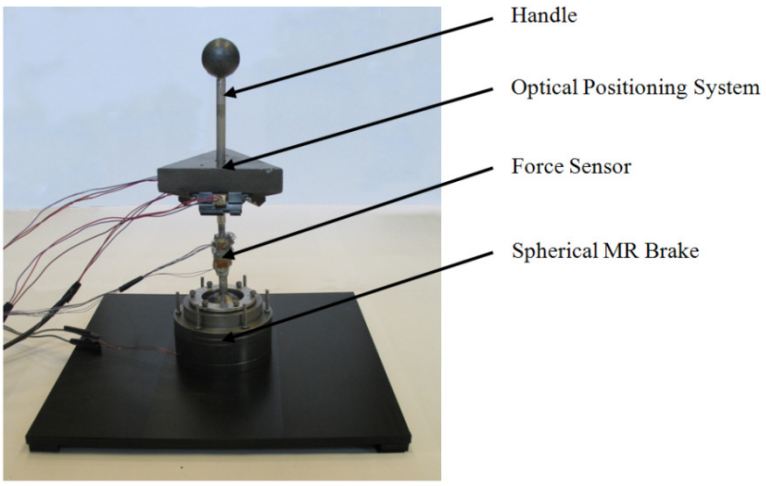

Figure 3.9. Force feedback joystick.

3.2.1.1 Optical Position Measurement System

Conventional spherical joints use encoders attached to three different axes of the joint through a gimbal mechanism to measure the orientation [47]. Although this is a viable approach, we explored another approach to meet the design goal of building a compact system.

Three IR sensors by Sharp, Inc. were used to build an optical triangulation system to measure the position of the joystick handle (Figure 3.10).

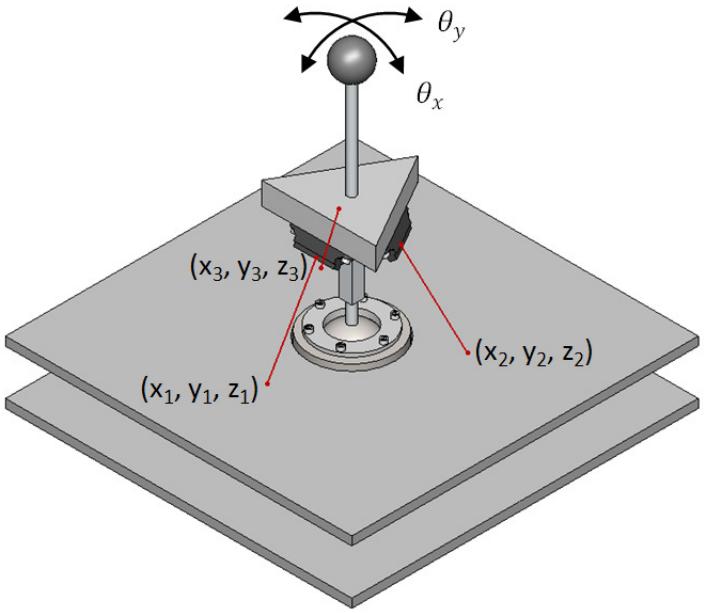

Figure 3.10. Optical triangulation system using IR sensors for position measurement.

The sensors measure distance by sending an infrared signal and receiving the signal that bounces back from a surface. They have a range of 4 to 30 cm and generate an analog signal corresponding to the measured distance. The sensors were placed in a triangular arrangement angled slightly outward and facing down.

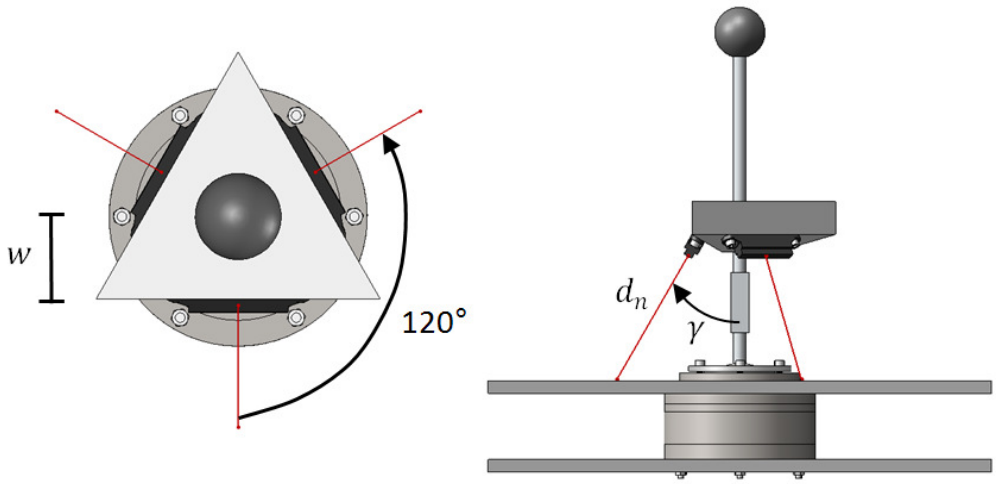

Figure 3.11. Position and orientation of the optical sensors on the joystick handle.

The data received from the sensors are the distance measurements to three points on the base plane. The coordinates of these three points with respect to the joystick handle can be found as:

$$(x_1, y_1, z_1) = (w + \sin\gamma \cdot d_1\,, 0\,, \cos\gamma \cdot d_1) \tag{3.14}$$

$$(x_2, y_2, z_2) = (-\cos 60° \cdot w - \cos 60° \cdot \sin\gamma \cdot d_2,\ \sin 60° \cdot w + \sin 60° \cdot \sin\gamma \cdot d_2,\ \cos\gamma \cdot d_2) \tag{3.15}$$

$$(x_3, y_3, z_3) = (-\cos 60° \cdot w - \cos 60° \cdot \sin\gamma \cdot d_3,\ -\sin 60° \cdot w - \sin 60° \cdot \sin\gamma \cdot d_3,\ \cos\gamma \cdot d_3) \tag{3.16}$$

where "w" is the distance of each sensor from the centre of the handle, γ ($\gamma = 30°$) is the angle between the handle and the direction of the optical sensors and d_n is the distance measurement for sensor n (Figure 3.11).

Once the three points on the base plate are known, position of a virtual plane overlapping the base plate can be calculated:

$$A \cdot x + B \cdot y + C \cdot z + D = 0 \tag{3.17}$$

where the coefficients "A", "B", "C" and "D" can be found by using the following determinants:

$$A = \begin{vmatrix} 1 & y_1 & z_1 \\ 1 & y_2 & z_2 \\ 1 & y_3 & z_3 \end{vmatrix} \quad B = \begin{vmatrix} x_1 & 1 & z_1 \\ x_2 & 1 & z_2 \\ x_3 & 1 & z_3 \end{vmatrix} \quad C = \begin{vmatrix} x_1 & y_1 & 1 \\ x_2 & y_2 & 1 \\ x_3 & y_3 & 1 \end{vmatrix} \quad D = -\begin{vmatrix} x_1 & y_1 & z_1 \\ x_2 & y_2 & z_2 \\ x_3 & y_3 & z_3 \end{vmatrix} \tag{3.18}$$

Then, the relative angles between the base plate and the handle (Figure 3.12) can be found through a unit vector that is collinear with the joystick handle:

$$\theta_x = \sin^{-1}\left(\frac{-B}{\sqrt{A^2+B^2+C^2}}\right) \tag{3.19}$$

$$\theta_y = \sin^{-1}\left(\frac{-A}{\sqrt{A^2+B^2+C^2}}\right) \tag{3.20}$$

The optical system can measure the joystick handle position in 3D as the user moves it in any direction. As the system works by measuring the relative orientation of the base plate, rotating the base plate would have absolutely no effect on the position sensor readings $(\mathrm{d}_1, \mathrm{d}_2, \mathrm{d}_3)$. Therefore, the system cannot measure rotation of the handle about its own axis. This would require an additional sensor, such as an absolute encoder, which was not implemented in this prototype due to the intended joystick application for virtual reality.

3.2.1.2 Force Measurement

When passive actuators, like the MR spherical brake, are used in haptics applications, it is necessary to measure the forces applied by the user in addition to position measurements to control the behavior of the device. If only position is measured, then the so called "sticky wall" [48] situation occurs where the joystick will not release the brake as the user tries to pull away from a collision with a virtual object.

We built a simple load cell with two sets of strain gage full bridges to measure the forces applied by the user on the handle. Although the spherical MR-brake is able to generate moments in all three DOF, in this study we concentrated only on measurement of the user forces in "x" and "y" directions. For the intended purpose of the prototype as a haptic joystick the moment around the handle was neglected since it was not needed. The load cell was made of aluminum and its design was optimized using finite element analysis. The strain gages were connected to strain gage amplifiers (5B38-05) by Analog Devices. The circuitry was interfaced to a data acquisition card (PCI-MIO-16E-4) by National Instruments.

3.2.1.3 Haptic Rendering and Control Architecture

Virtual environments integrated with haptic devices typically run two processes. The first process involves collision detection, haptic rendering and updating the graphics in the virtual world with about 15-30 frames per second. The second process is the control loop of the haptic device which usually runs at 1000 Hz. As shown in Figure 3.12, we implemented a two-layer control architecture consisting of a low-level and high-level controller.

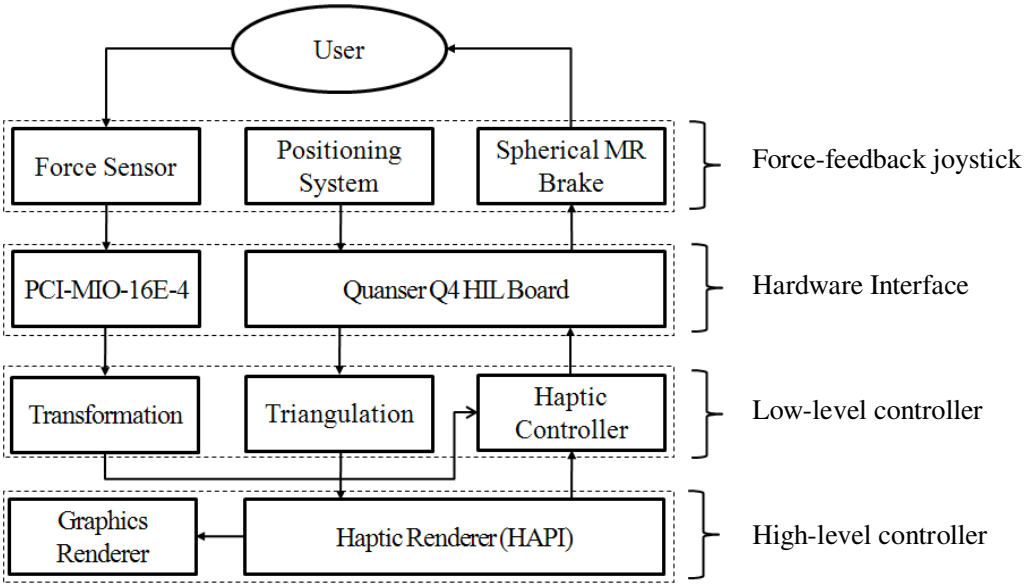

Figure 3.12. Control system architecture.

The low-level controller is to control the haptic device. It uses a Q4 hardware-in-the-loop card by Quanser, Inc. and a PCI-MIO-16E-4 data acquisition card by National Instruments. The control algorithm was implemented using Simulink by Mathworks, Inc. [49] along with the WinCon software which enables real-time code generation from Matlab/Simulink diagrams. The Q4 handles signals coming from the optical sensors and the command signal going out to the spherical MR-brake. The PCI-MIO-16E-4 handles the analog signals coming from the load-cell.

The high-level controller is for the virtual environment. We used H3DAPI which is an open source haptics package by SenseGraphics AB [41]. The H3DAPI uses OpenGL to render graphics and has its own haptics renderer called HAPI. We chose the proxy-based Ruspini algorithm for the haptic rendering [42].

Low-level controller computes coordinate transformations for the force sensor and the triangulation for the optical sensors. The data are then sent to the high-level

controller which generates the command force necessary to create the haptic sensation. The command force is returned to the low-level controller which processed the command signal and the force input from the user to compute the necessary braking torque signals. This signal then goes to the spherical MR-brake through a current-controlled servo amplifier. Details and implementation of the controller for the spherical MR brake can be found in Appendix B.1 along with the Simulink/H3DAPI interface code in Appendix B.3.

CHAPTER 4

PASSIVE HAPTIC INTERFACE FOR DENTAL IMPLANT SURGERY

4.1 Passive Haptic Interface Design

The prototype consists of four components: (1) MR-brakes (2) Position sensors (3) A 6-DOF force sensor and (4) Hand-piece for drilling (Figure 4.1). Pen-based haptic devices [22] were taken as an example in the design of this first prototype. Hence, three joints were actuated with MR-brakes for creating the haptic feedback and the remaining three joints were left un-actuated at its wrist to provide motion in 6 DOF. CAD drawings of the passive haptic interface can be found in Appendix A.

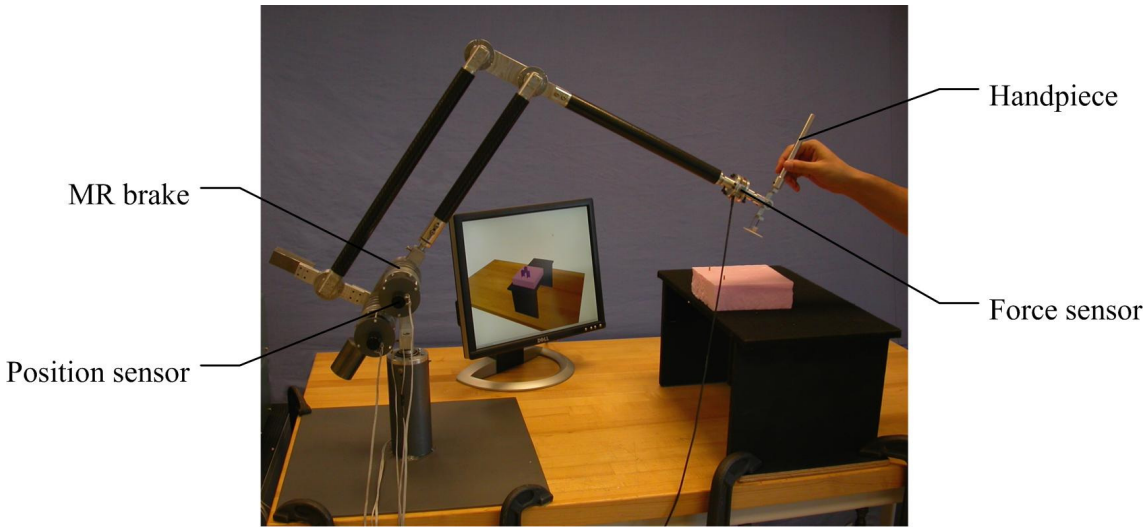

Figure 4.1. Passive haptic interface

4.2 Balancing

The weight of the arm should not be felt by the surgeon to ensure transparency of the system. Therefore, the arm was made out of lightweight components. Furthermore,

its weight was compensated. Since there are no active actuators in the system active weight compensation is not possible. For this reason, static mass balancing was done by using balancing weights and by strategically placing MR-brakes on the arm geometry. The brakes were positioned close to the center of rotation of joints 2 and 3 in order to minimize the inertia of the system (Figure 4.2). Brake 3 (at J_3) together with balancing weight "A" (m_a) were used to balance the arm around joint 2 (J_2). Balancing weight "B" (m_b) was used to balance the arm around joint 3 (J_3).

Torque applied to J_4 is transferred to J_3 by mechanical links. Hence, it can be assumed that joints J_4 and J_3 are overlapping and the link between m_b and m_2 is connected to the link between m_4 and m_6. Using this principle, the only weight that tries to rotate the arm in the clockwise direction is m_6. The rest of the weights try to rotate the arm in the counter-clockwise direction.

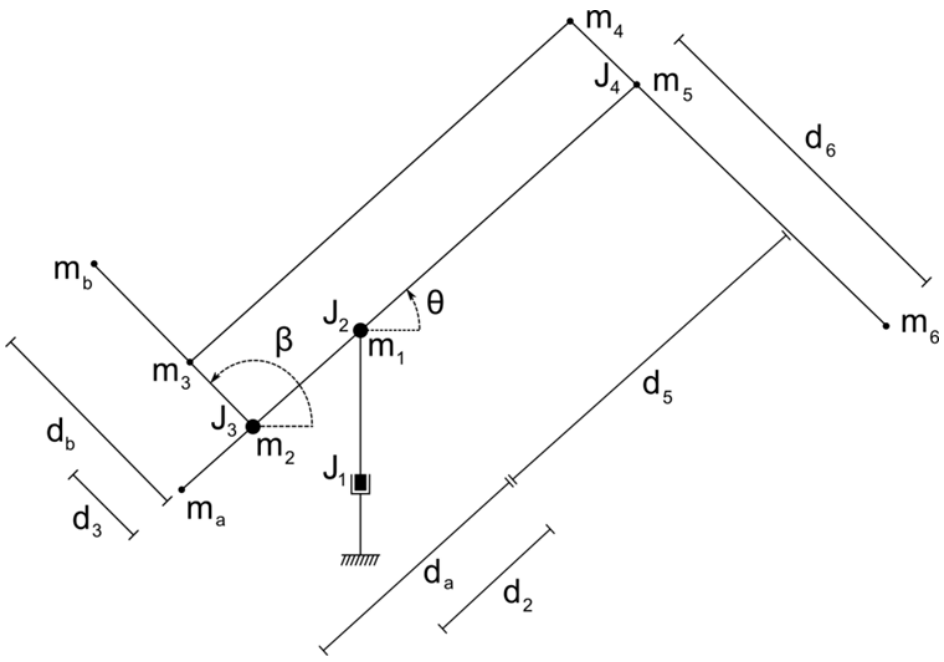

Figure 4.2. Mass balancing

Since the weight of the hand-piece is relatively small mass balancing around the un-actuated joints J_4, J_5 and J_6 was neglected. Also, as the first joint axis is in the direction of gravity, only joints 2 and 3 need to be balanced. The weight of the linkages is transferred equally to the joints they are attached. Therefore, mass balancing can be done by considering the joints as point masses.

For J_3:

$$d_b \cdot m_b + d_3 \cdot (m_3 + m_4) \cdot \cos(\pi - \beta) = (d_6 \cdot m_6) \cdot \cos(\pi - \beta) \qquad (4.1)$$

$\cos(\pi - \beta)$ terms cancel out giving:

$$d_b \cdot m_b + d_3 \cdot (m_3 + m_4) = (d_6 \cdot m_6) \qquad (4.2)$$

Since no position variables remain in equation 4.2, J_3 can be statically balanced.

Similarly, for J_2:

$$(d_2 \cdot m_2 + d_a \cdot m_a) \cdot \cos(\theta) + (d_2 \cdot \cos(\theta) + d_3 \cdot \cos(\pi - \beta)) \cdot m_3$$

$$+ (d_2 \cdot \cos(\theta) + d_b \cdot \cos(\pi - \beta)) \cdot m_b = (d_5 \cdot \cos(\theta)) \cdot m_5 \qquad (4.3)$$

$$+(d_5 \cdot \cos(\theta) - d_3 \cdot \cos(\pi - \beta)) \cdot m_4 + (d_5 \cdot \cos(\theta) + d_6 \cdot \cos(\pi - \beta)) \cdot m_6$$

Rearranging and substituting equation 4.1 into equation 4.3 cancels out the $\cos(\pi - \beta)$ term, leaving:

$$d_2 \cdot m_2 + d_a \cdot m_a + \mathrm{d_2 \cdot m_3 + d_2 \cdot m_b - d_5 \cdot m_5 - d_5 \cdot m_4 - d_5 \cdot m_6} = 0 \qquad (4.4)$$

Since no position variables remain in equation 4.4, J_2 can also be statically balanced. It should be noted that gravitational constant "g" was omitted in all of the above equations as it would cancel out in the end.

4.3 Prototype Implementation

Following the design principles of pen-based haptic devices [22], three joints were actuated with MR-brakes for creating the haptic feedback, leaving the remaining three joints un-actuated at the wrist to provide motion in 6 DOF. The links were made out of carbon fiber tubing and aluminum caps to keep the mass of the system low. The three un-actuated joints at the wrist were arranged such that the combined motion creates a spherical joint at the tip. The wrist joints use 2 ball bearings each to reduce friction and play. The brakes provide actuation and structural support for the remaining joints. They were built with a pair of tapered roller bearings under pretension to minimize play.

Three 10-turn precision potentiometers were used at the actuated joints for position sensing (Model 3509s-8-202 from Bourns, Inc. [50]). They were connected to analog input ports of a Q4 hardware-in-the-loop interface card by Quanser, Inc. [51]. The manufacturing specifications for these potentiometers are 0.021% resolution with 0.5% linearity. The range of motion is 360° around J_1, 70° around J_2 and 170° around J_3 with a maximum reach of approximately 0.86m. Table 4.1 shows the Denavit-Hartenberg parameters for the arm.

Table 4.1: Denavit-Hartenberg parameters for passive haptic arm

i	α_{i-1}	a_{i-1}	d_i	θ_i
1	0	0	0	θ_1
2	-π/2	0	0	θ_2
3	0	0.411m	0.3814m	θ_3
4	0	0	0	0

The haptic arm has a range of motion of 360° around J_1, 70° around J_2 and 170° around J_3. With these ranges of motion, given link lengths and the interference from the base plane the work volume of the arm can be constructed for the center of the wrist joint (Figure 4.3). This gives a maximum reach of ~0.86m for the arm.

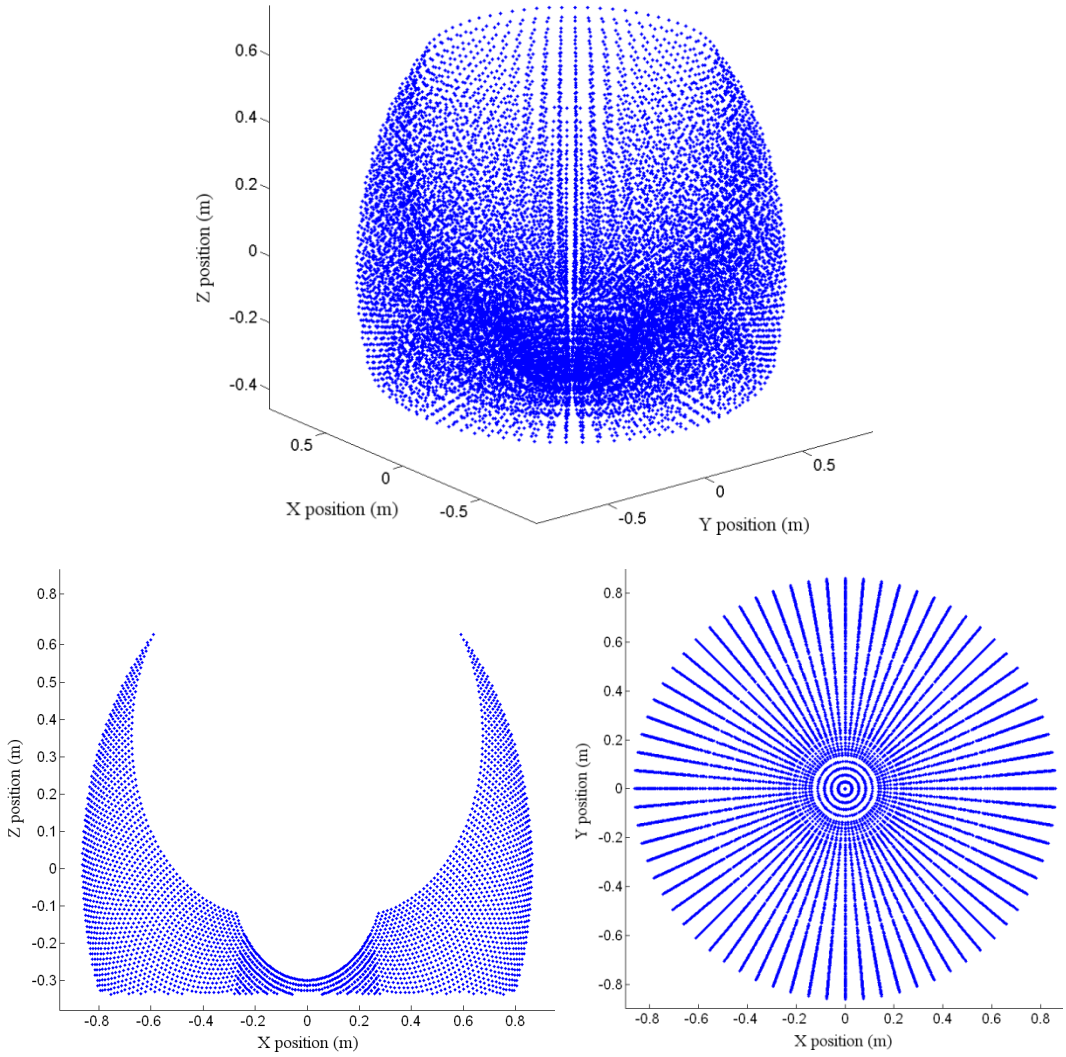

Figure 4.3. Work volume of the haptic arm

A 6-DOF load cell (Mini 45 from ATI Industrial [52]) was used for force sensing. It is capable of sensing torques and moments in 3D. The sensor was placed at the base of the wrist joint to measure the user input forces.

4.3.1 End Effector

The end-effector of the haptic interface uses a spherical joint at the wrist and a small drill bit at the end of the hand-piece (Figure 4.4). The x-y-z coordinate of the drill bit can be constrained using the haptic feedback created by the MR-brakes. In this first prototype orientation was not constrained. An alignment plate with a sleeve was attached onto the drill bit to provide angular guidance during user experiments (explained later).

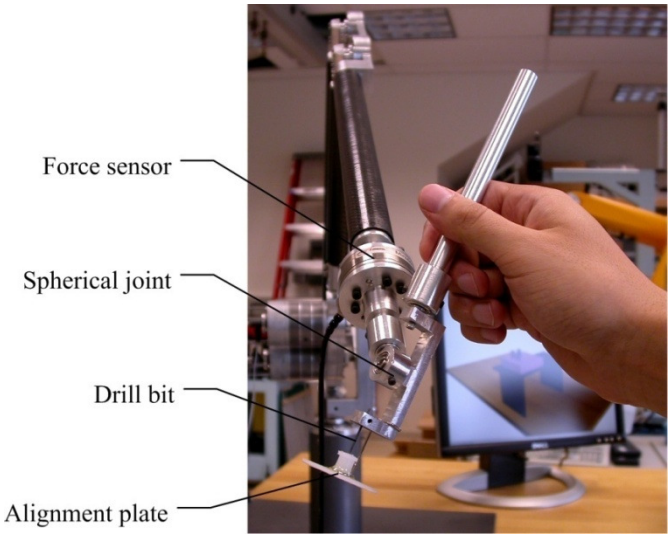

Figure 4.4. Handpiece

CHAPTER 5

SOFTWARE DEVELOPMENT

5.1 Control System

The system was interfaced to a computer using a Q4 hardware-in-the-loop card by Quanser, Inc. [51] and a PCI-MIO-16E-4 data acquisition card by National Instruments [53] (Figure 5.1).

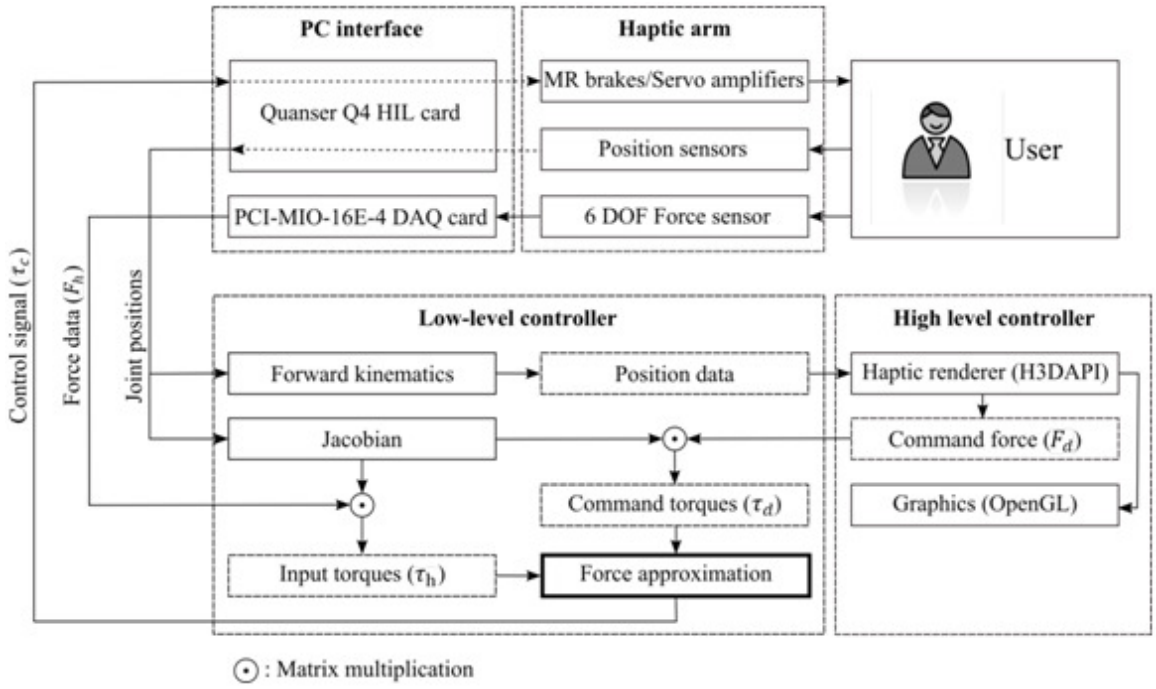

Figure 5.1. Haptic arm with the PC Interface and Haptic Rendering

The control algorithm was implemented using Simulink by Mathworks, Inc. [49] along with the WinCon software which enables real-time code generation from Matlab/Simulink diagrams. The Q4 handles signals coming from the position sensors

and the command signals going out to the MR-brakes. The PCI-MIO-16E-4 handles the analog signals coming from the force sensor.

For haptic rendering, we implemented a two-layer control architecture consisting of a low-level and high-level controller (Figure 5.1).

5.1.1 High-Level Controller

The high-level controller is for the virtual environment. We used H3DAPI which is an open source haptics package by SenseGraphics AB [41]. The H3DAPI uses OpenGL to render graphics and has its own haptics renderer called HAPI. The proxy-based Ruspini algorithm was chosen for the haptic rendering [42]. H3DAPI was interfaced to WinCon API using memory sharing to access I/O signals on the hardware-in-the-loop card. Code for interfacing between H3DAPI and simulink can be found in Appendix B.3

The controller receives the position of the tip of the arm, renders the virtual world graphics and computes collisions between the virtual objects and the tip to generate command forces to be applied to the user's hand.

5.1.2 Low-Level Controller

The low-level controller receives joint positions and force input data from the user's hand. It computes the forward kinematics and the Jacobian matrix for the haptic arm (Figure 5.1). Forward kinematics is used to find the Cartesian position of the tip. Then, the tip position is sent to the high-level controller which generates the command force necessary to create the haptic sensation. The command force is returned to the low-level controller which uses the Jacobian matrix to calculate the necessary command

torque at the joints. User‘s input force is also converted into joint torques. Both the input and the command torques need to be used to calculate the command signal going into the MR brake servo-amplifiers (Appendix C). This is accomplished using a force approximation algorithm explained next.

As passive devices can only apply forces opposing the user’s motion, traditional control algorithms for haptics cannot be used for the control of MR-brakes. The problem occurs mainly in tasks that require following a rigid surface (wall-following). In following an ideal frictionless wall, the force vector applied to the user’s hand must be normal to the surface regardless of the configuration of the mechanism or the direction of the user’s motion. However, with passive devices, this is rarely the case. In situations where the user is trying to push into the wall and slide on the surface at the same time the braking torques that are preventing the user from penetrating into the wall also prevent him from sliding on the surface. This creates a sticky feeling on the wall surface which greatly degrades the haptic feedback.

Algorithms to overcome this problem have been proposed. A method that uses a very narrow band along the virtual wall was proposed. By selectively locking the brakes to keep the tip position inside this narrow band the haptic device was forced to move along the wall surface in a zig-zag fashion [54]. This algorithm was implemented in a 5-bar planar mechanism using electro-rheological brakes. A force approximation method called “Passive Force Manipulability Ellipsoid Analysis” (FME) was also proposed [43, 44]. Because of its general applicability to the whole work volume of the haptic device and to the existing proxy-based rendering techniques we chose FME for the haptic rendering.

The controller converts the Cartesian command force coming from the high-level controller and the user input force coming from the force sensor into joint torques:

$$\tau_d = \boldsymbol{J^T} \cdot F_d \text{ and } \tau_{\mathrm{h}} = \boldsymbol{J^T} \cdot F_h \tag{5.1}$$

Where $\boldsymbol{J}$ is the Jacobian matrix for the haptic arm, F_d is the command force generated by the high-level controller in Cartesian coordinates, F_{h} is the input force from the user in Cartesian coordinates. τ_d and τ_h are the command torques in joint coordinates and user input force in joint coordinates, respectively.

The force approximation algorithm compares the two joint torques and computes command signals depending on their relative direction:

$$\tau_c = \tau_d \;\; if \;\; \tau_d \cdot \tau_h < 0$$

$$\tau_c = 0 \;\; if \;\; \tau_d \cdot \tau_h \geq 0 \tag{5.2}$$

Where τ_c is the command torque. The command torque is applied by the brake if its direction is opposing to the users input force. If the user‘s input and the command torques are in the same direction, then there is no need to activate the brakes ($\tau_c = 0$). Implementation of the low-level controller in simulink can be found in Appendix B.2.

CHAPTER 6

EXPERIMENTS AND RESULTS

6.1 Rotary MR Brake Experiments

A test setup was constructed to identify the parameters of the prototype MR brake (Figure 6.1). The setup consisted of a torque sensor (from Transducer Techniques, Inc. [52]) attached to the brake chassis, a brush assembly to allow multiple rotations of the shaft and a high precision potentiometer to measure position. Real time control was implemented using a Quanser Q4 Series hardware-in-the-loop board connected to SIMULINK via WinCon software [51].

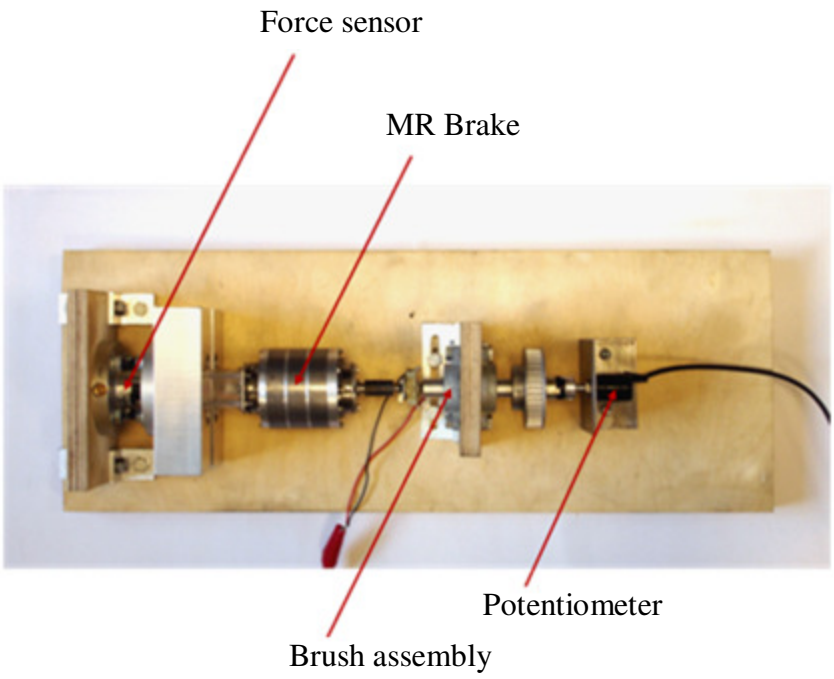

Figure 6.1. Experimental setup for rotary MR brake.

6.1.1 Braking Torque

In this experiment, the goal was to determine the braking torque as a function of coil current. The current on the coil was increased by 0.1 A starting from zero to 1.5 A. Then, the current was decreased using the same step size. The data from each step was taken in 3 minute intervals to achieve consistency in readings. Figure 6.2 shows torque/current curve for the full range of the braking torque. The minimum (off-state) and maximum torque were found as 0.08 Nm and 10.9 Nm, respectively. This gives a dynamic range of about 43 dB.

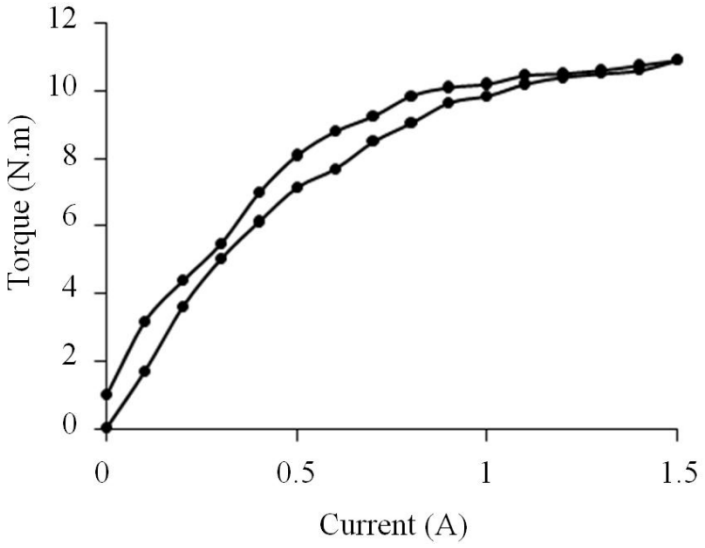

Figure 6.2. Braking torque of rotary MR brake versus current

6.1.2 Wall Collision

The experimental setup was converted into a 1-DOF haptic device by attaching a lever arm to the MR Brake. The purpose of this experiment was to observe how well the brake could simulate a collision with a virtual wall (surface). The control loop was running at 1000 Hz with 1 A current for the brake during collision. The current was

turned on fully when collision occurred. The experiment was first conducted in two modes: (1) without the torque sensor, and (2) with the torque, sensor to see the effect on the haptic behavior. Algorithm for the wall collision experiment with the torque sensor is as follows:

```
while simulation is running
    if position is inside the wall and torque is towards the wall
        activate brake in forward direction
    else if readyToDemagnetize is true and brake is active
        reset counter
        set readyToDemagnetize to false
        activate brake in reverse direction
    else
        deactivate brake
    end if
    if counter > demagnetizationDutation
        set readyToDemagnetize to true
        deactivate brake
    end if
end while
```

The results of virtual wall simulation without the torque sensor are presented in Figure 6.3a and 6.3b.

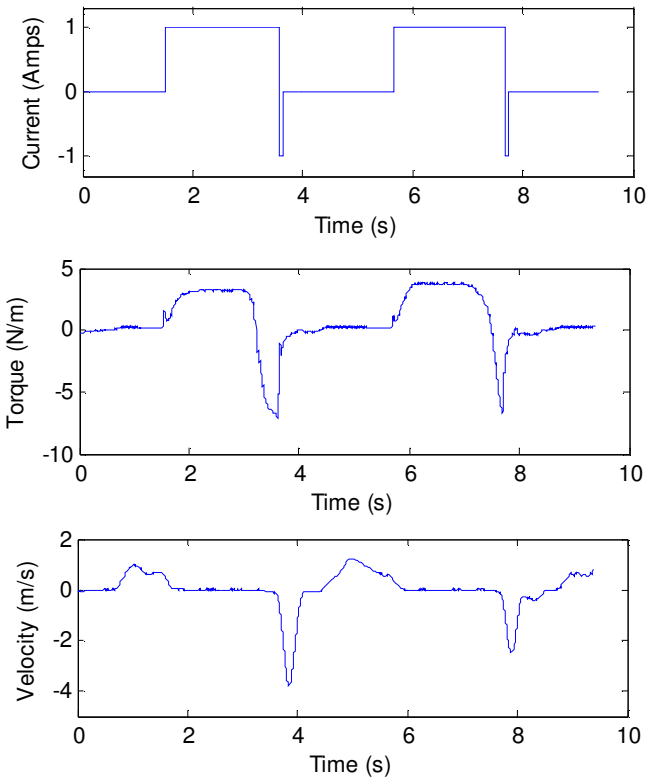

(a)

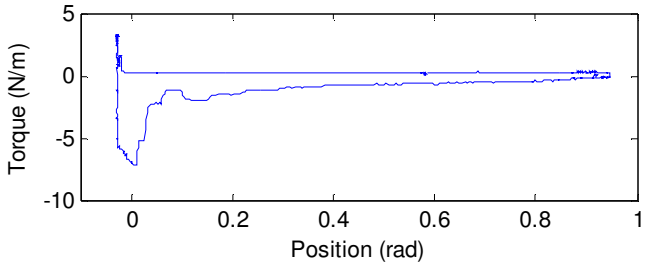

(b)

Figure 6.3. Simulation of collision with a virtual wall located at position zero without using the torque sensor. (a) Input current, torque and velocity. (b) Virtual wall at position 0. The lever arm is first rotated away from position zero through approximately 0.95 radians. Then, it is rotated back towards the virtual wall for collision simulation.

The results of virtual wall simulation with the torque sensor are presented in Figure 6.4a and 6.4b.

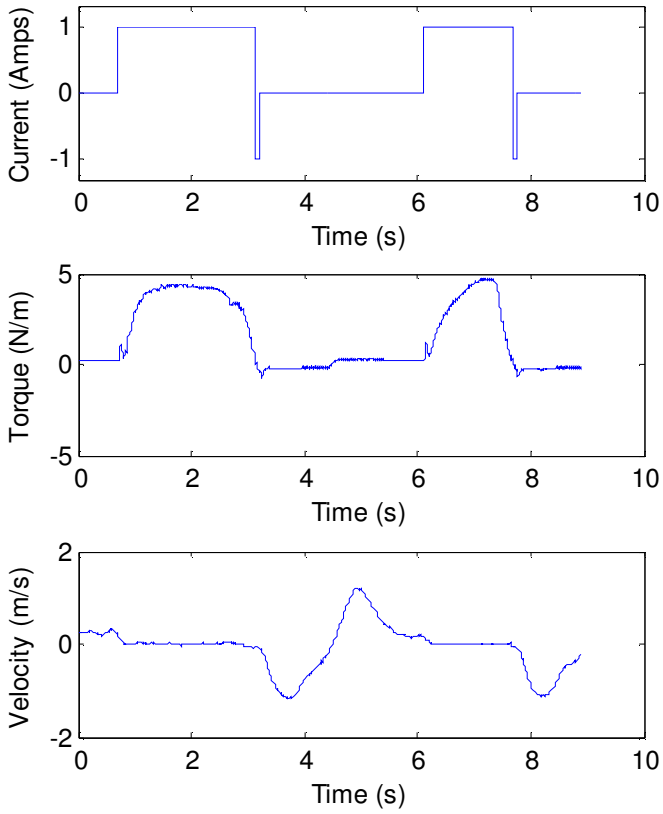

(a)

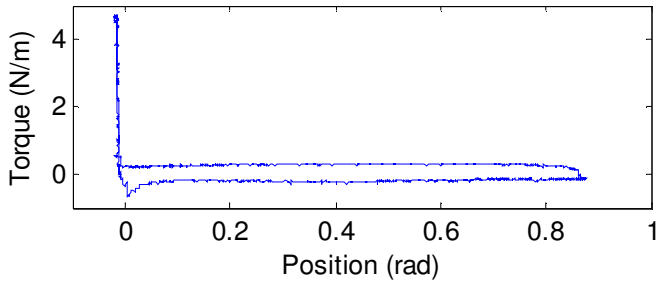

(b)

Figure 6.4. Simulation of collision with a virtual wall located at position zero with the torque sensor. (a) Input current, torque and velocity. (b) Virtual wall at position 0. The lever arm is first rotated away from position zero through approximately 0.9 radians. Then, it is rotated back towards the virtual wall for collision simulation.

6.1.3 Damping Experiment

A servo amplifier (DR100EE20A8BDC-QD1 from Advanced Motion Controls [55]) was added to the setup. This enabled us to supply variable current to the brake. Closed loop PI current control was performed by the servo amplifier. The purpose of the experiment was to see how well the MR brake could represent a virtual damper. Relationship between velocity and torque was denoted as:

$$T = b \cdot \omega \tag{6.1}$$

where damping ratio "b" was chosen as 1 Nm.s/rad.

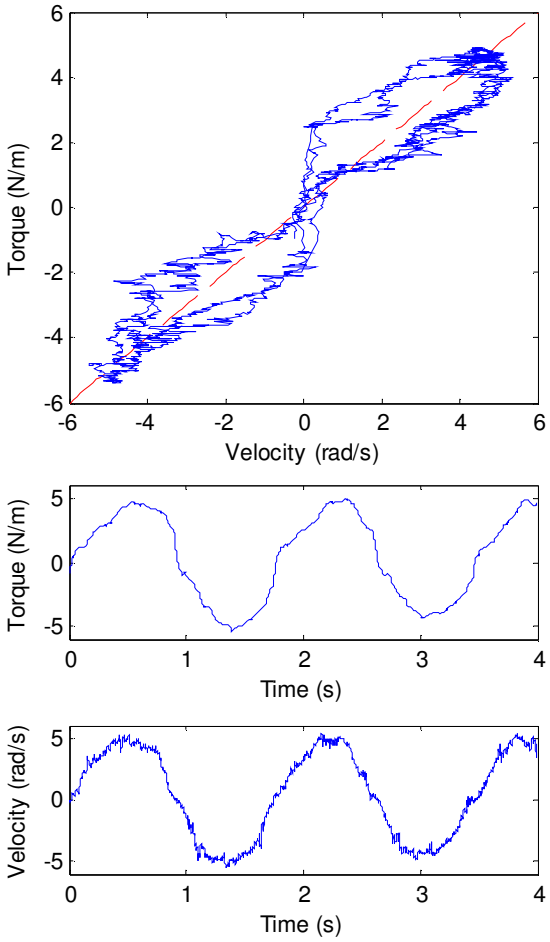

Figure 6.5. MR brake as a damper in haptics.

6.1.4 Coulomb Friction Experiment

We also explored the Coulomb friction characteristics of the MR brake. Karnopp model was used to represent Coulomb friction due to its simplicity and ease of implementation [56]. This model uses a velocity dead-band to define static friction range instead of using absolute zero velocity which is very difficult to obtain with digital systems due to discretization. The model can be represented as:

$$T_{friction} = \begin{cases} T_{dynamic} \cdot \mathrm{sgn}(\omega) & |\omega| > \Delta\omega \\ \max(T_{static}, T_{applied}) & |\omega| < \Delta\omega \end{cases} \tag{6.2}$$

where a 0.5 rad/s velocity-deadband (Δw) was used and static friction torque (T_{static}) was set at 5 Nm, dynamic friction torque ($T_{dynamic}$) was set at 3 Nm.

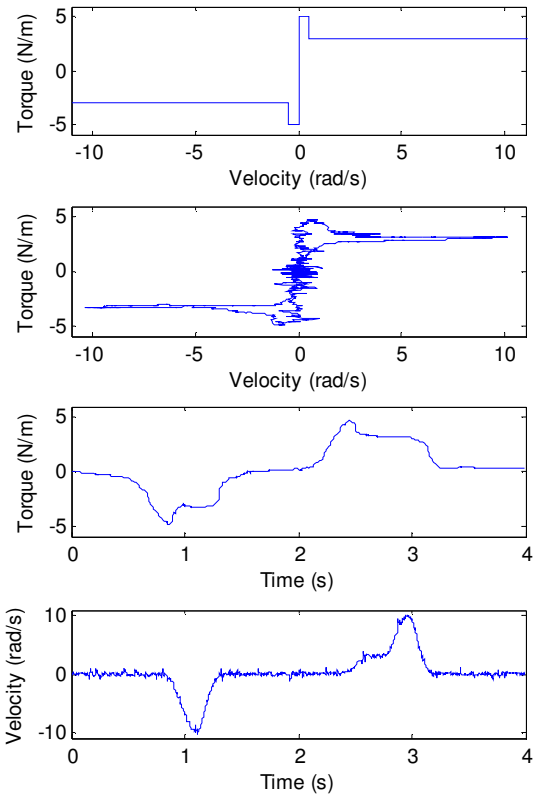

Figure 6.6. MR brake representing Coulomb friction.

6.1.5 Transient Response

The transient response was obtained using the wall collision results. The purpose of the experiment was to find the time constant of the brake and to explore the effect of input current on the response. The experiment was repeated for current levels of 0.25, 0.5, 0.75 and 1A. Transient response was recorded after the initial contact with the wall.

The torque output resembles a typical first order system response in reaction to step changes in current (Figure 6.7). The time constant was measured to be 60 milliseconds by overlaying a simulated first order system response on the experimental data.

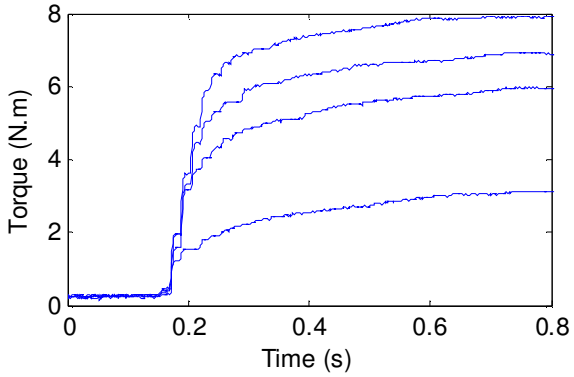

(a) Transient response at 0.25A, 0.5A, 0.75A and 1A.

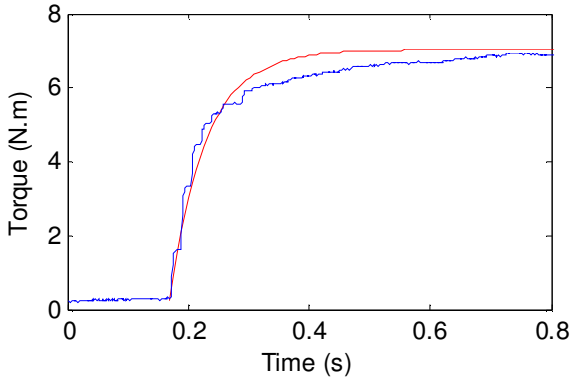

(b) Simulated first-order response overlaid on the experimental data at 0.75A.

Figure 6.7. Transient response and time constant of the MR brake.

6.1.6 Discussion

Hysteresis behavior can be observed in the torque/current curves in figure 6.2. This behavior is due to the magnetization of steel elements in the MR brake [57]. Magnetization in ferromagnetic elements does not relax back to zero even if the imposing magnetic field is removed. Unfortunately, this behavior not only adversely affects the controllability of the MR brake but also increases the off-state torque greatly. In our experiments the residual magnetization kept the off-state torque at 1.05 Nm after applying and removing 1.5A coil current. It caused unwanted off-state friction and reduced the backdrivability of the brake. To overcome this problem the controller was modified. At the instant the brake was turned off it was reactivated in the reverse direction with a very short current impulse. An impulse with amplitude of 1A and 55 ms duration (Current plot in Figure 6.3a and 6.4a) was found to be enough to collapse the residual magnetic field reducing the off-state torque to 0.08 Nm from 1.05 Nm.

The effect of hysteresis is even more apparent in the damper experiment (Figure 6.5). This was mainly caused by the continuous nature of this experiment leaving no time to apply current in the reverse direction in order to demagnetize the brake. As a result, the system output two different torque outputs for a given velocity and also limited the minimum amount of viscous torque that could be simulated with the system. Another difficulty in this experiment was the time lag of the system having an adverse effect on the simulation performance. Delays in discrete velocity calculations sometimes caused incorrect torque outputs during acceleration and deceleration.

When the torque sensor was used, our experiments with the virtual wall simulation produced a very crisp reaction force upon initial contact and very high rigidity

at the quasi-static contact with the wall (Figure 6.4). When the lever arm collided with the virtual wall, the brake locked the position of the arm at zero radian. This created a very rigid wall feeling. If the user tried to push the arm into the wall, the reaction torque increased sharply (top vertical part of the curve in Figure 6.4b). When the lever was pulled away from the wall, there was about 0.5 Nm torque acting in the reverse direction as the separation occurred. Then, the brake turned off completely providing nearly zero resistance. Most likely the time lag of the brake coupled with the delay in deactivating the brake due to the demagnetization action caused the small initial torque in the reverse direction. On the other hand, when the torque sensor was not used, the release action from the wall had a "sticky" feeling (Figure 6.3b). This was due to the fact that the brake was controlled only with position feedback. Once the wall penetration occurred, the controller had no way of knowing the direction of the user input. As the user tried to pull away from the wall, the release torque was almost as high as the maximum torque the brake could apply (bottom vertical part of the curve in Figure 6.3b). This caused the "sticky" wall feeling and also increased the observed velocities after the release since the user had to pull the handle very hard to break away from the virtual wall.

It was found that the MR brake could simulate coulomb friction with good accuracy. Although the mathematical model for such a simulation is rather simple, active actuators (actuators that can add energy into the system) such as servo motors have great difficulty in simulating discontinuous forces because of stability issues [56].

The transient response of the brake closely resembled first order system behavior with a time constant of 60 ms. The experiment was repeated for different input currents and it was found that input current had no effect on the time constant.

The 10.9 Nm maximum torque output obtained from the experiments was slightly higher than the 10.83 Nm obtained from the calculations. This small deviation can be attributed to mathematical simplifications, such as Bingham Plastic model, inherent errors that were caused by finite element analysis of the magnetic field and neglecting some physical effects such as Coulomb friction.

6.2 Spherical MR Brake Experiments

A series of experiments were conducted with two objectives in mind. First objective was to identify the parameters of prototype spherical MR-brake and the second objective was to test the applicability of the brake to a haptics environment.

6.2.1 Braking Torque

In this experiment, the goal was to determine the braking torque as a function of coil current. The current on the coil was increased by 0.1 A starting from zero to 1.5 A. Then, the current was decreased using the same step size. The data from each step was taken in one minute intervals to achieve consistency in readings.

As shown in Figure 6.8, the minimum (off-state) and maximum torque were found as 0.1 Nm and 3.7 Nm, respectively. This gives a dynamic range of about 31 dB.

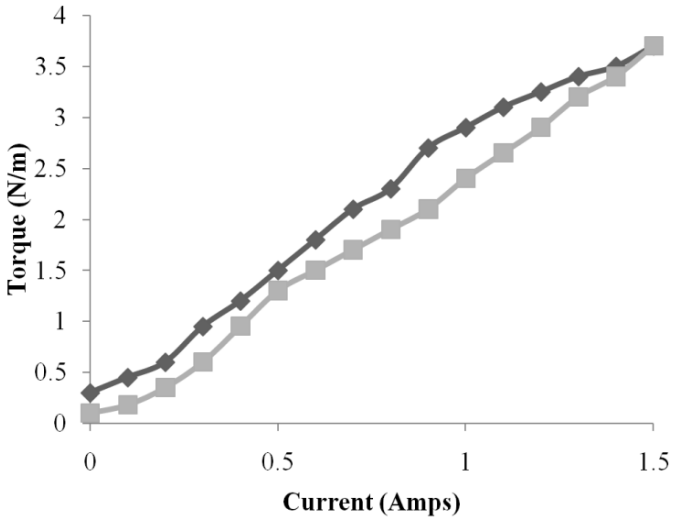

Figure 6.8. Hysteretic braking torque of spherical MR brake versus current (Light gray: zero to 1.5 A, dark gray: 1.5A to zero).

6.2.2 Wall Collision

A virtual wall was placed into the simulation environment. The purpose of this experiment was to assess how well the brake could simulate collision with a virtual surface (wall). A command force vector comes from the virtual environment and is normal to the wall surface. An input vector comes from the force applied to the joystick handle by the user indicating the intended motion. The control algorithm compares these vectors. If the dot product of the vectors is negative, this means the user is trying to penetrate the wall further and hence the brake is engaged. Furthermore, the controller implements a demagnetization algorithm to flush out the residual magnetic field in the brake after the joystick was pulled away from the wall.

The algorithm for the wall collision experiment is as follows:

while simulation is running do

if dotProduct(commandForce, userForce) < 0

(Condition for engaging the brake)

activate brake in forward direction

else if readyToDemagnetize is true and brake is active

(Condition for demagnetization)

reset counter

set readyToDemagnetize to false

activate brake in reverse direction

else

(Condition for deactivating the brake)

deactivate brake

end if

if counter > demagnetizationDutation

(Setting the demagnetization duration)

set readyToDemagnetize to true

deactivate brake

end if

end while loop

Where *"commandForce"* is the force vector from the virtual environment and *"userForce"* is the input force obtained through the force sensor; "*readyToDemagnetize"* and *"demagnetizationDutation"* are variables used for controlling the demagnetization.

To conduct the wall collision experiment the brake was driven at 1.5A current using the Quanser board.

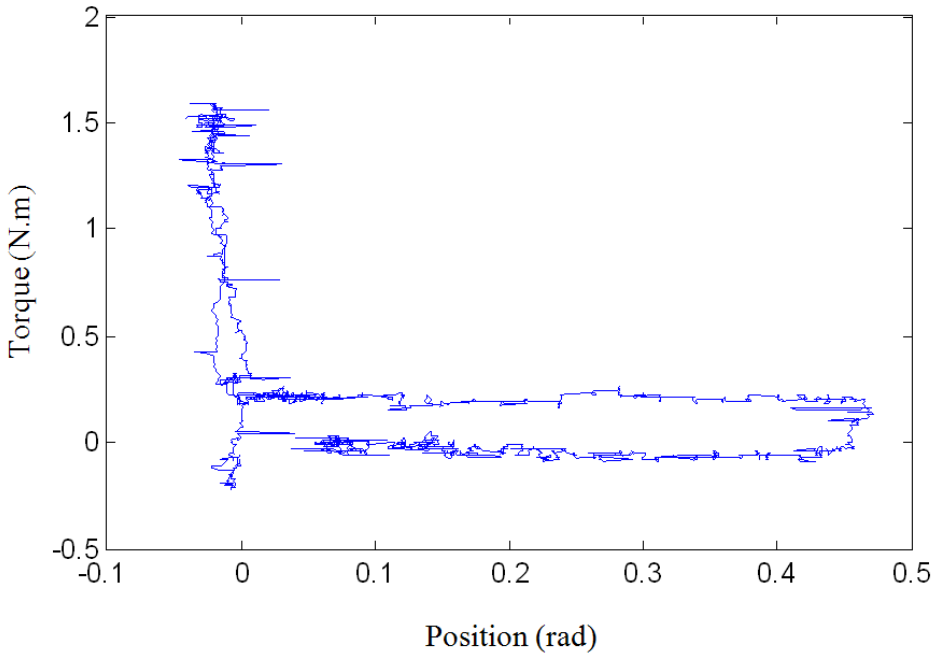

Figure 6.9. Simulation of collision with a virtual wall at position $\theta_x = 0$. The joystick handle is first pulled away from position zero through approximately 0.45 radians. Then, it is pushed back towards the virtual wall for the collision simulation.

6.2.3 Transient Response

The transient response was obtained using the wall collision simulation. The purpose of the experiment was to find the time constant of the brake and to explore the effect of input current on the response. The experiment was repeated for current levels of 0.5, 1 and 1.5A. Transient response was recorded after the initial contact with the wall. First order system behavior was observed, time constant was found as 170ms for all 3 current levels (Figure 6.10).

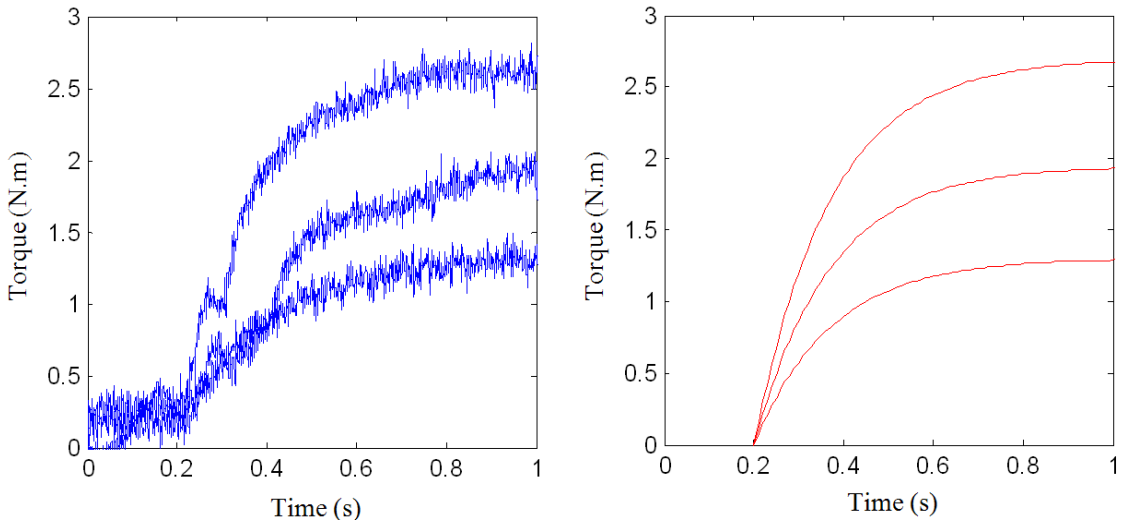

Figure 6.10. Transient response of spherical MR-brake (left). Simulated first order system responses used to estimate the time constant (right).

6.2.4 Damping Simulation

A linear analog servo amplifier was added to the setup. This enabled us to supply variable current to the brake. Closed loop PI current control was performed by the servo amplifier. The purpose of the experiment was to see how well the spherical MR-brake could represent a virtual damper. Equation 6.1 was used for denoting the relationship between angular velocity and torque. Damping ratio "b" was chosen as 1 N.m.s/rad and "*w*" was the angular velocity around the "y" axis.

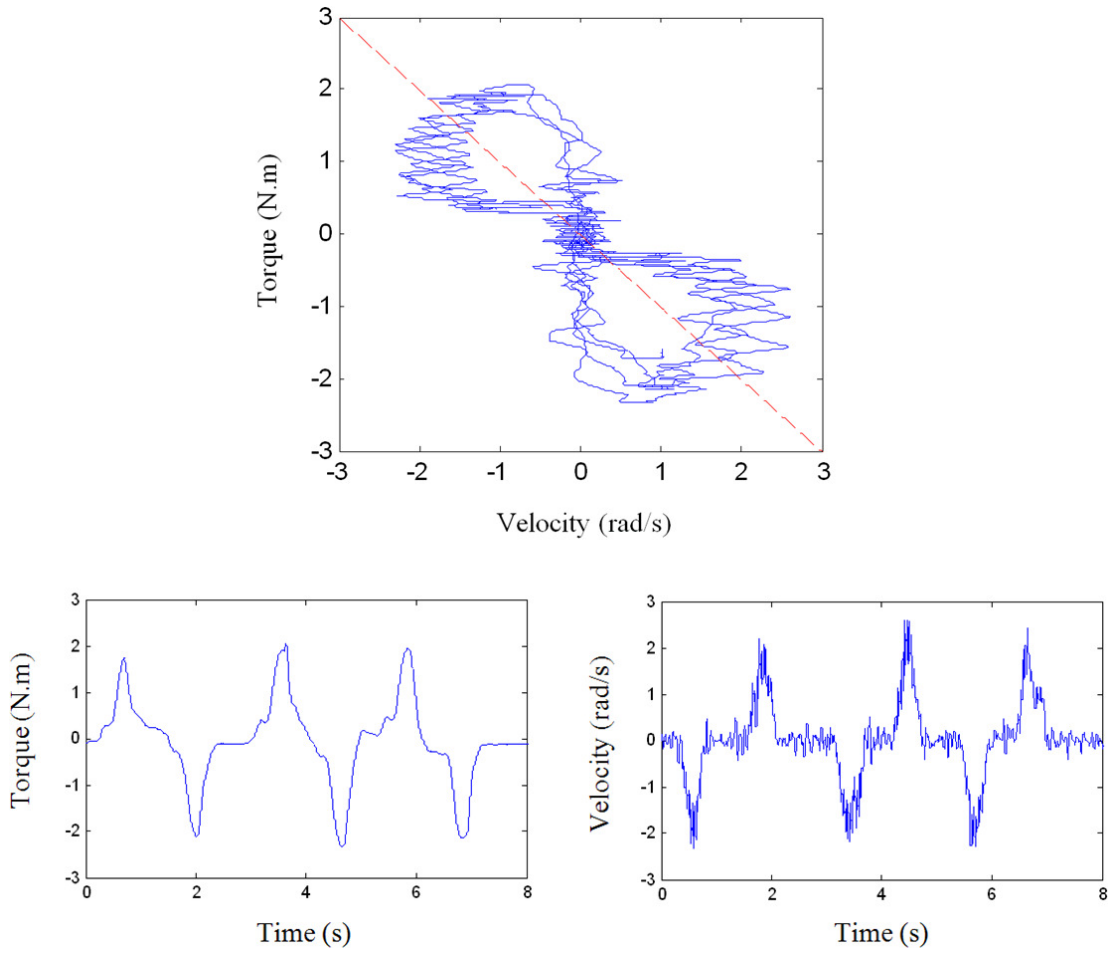

Figure 6.11. Viscosity simulation with the MR spherical brake as a damper (top). Breakdown of torque (left) and angular velocity around "y" axis (right) components of the viscosity simulation.

6.2.5 Coulomb Friction Simulation

The same setup as in the viscosity experiment was used to explore the ability of the brake to simulate Coulomb friction (Figure 6.12). Karnopp model was used to represent Coulomb friction [56]. Velocity-deadband (Δw) was selected as 0.3 rad/s and static friction torque (T_{static}) was set at 2.5 Nm. The dynamic friction torque ($T_{dynamic}$) was set at 0.5 Nm.

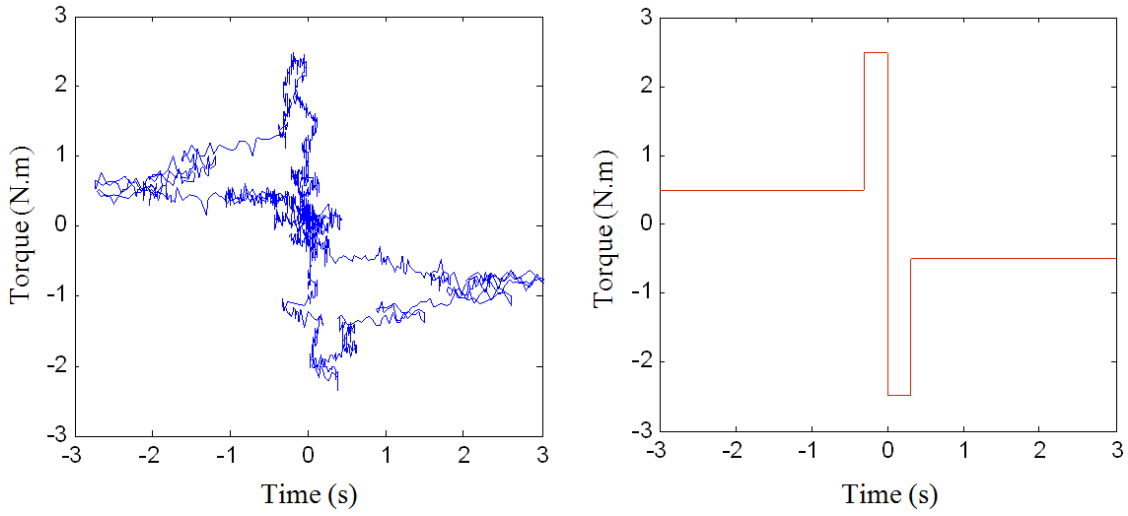

Figure 6.12. Spherical MR-brake simulating Coulomb friction along "x" axis (left), desired Coulomb friction (right).

6.2.6 Virtual Environment Simulation

Virtual environment simulations were conducted to verify the applicabilty of the MR spherical brake as a purely passive device. The objective of the experiment was to see the applicability of existing penalty based haptic rendering algorithms to a purely passive haptic device.

A virtual environment containing a manual gear shifter was constructed using X3D [58]. Graphical and haptic rendering of the environment was performed by H3DAPI. User's goal was to go through each gear and then return to the starting point, which is the straight up position of the joystick. The tracker was restricted using virtual walls seen in Figure 6.13. After the experiment was completed "x" and "y" angular position readings from the low level controller was compared to the geometry of the virtual gear shifter in order to observe the amount of wall penetration.

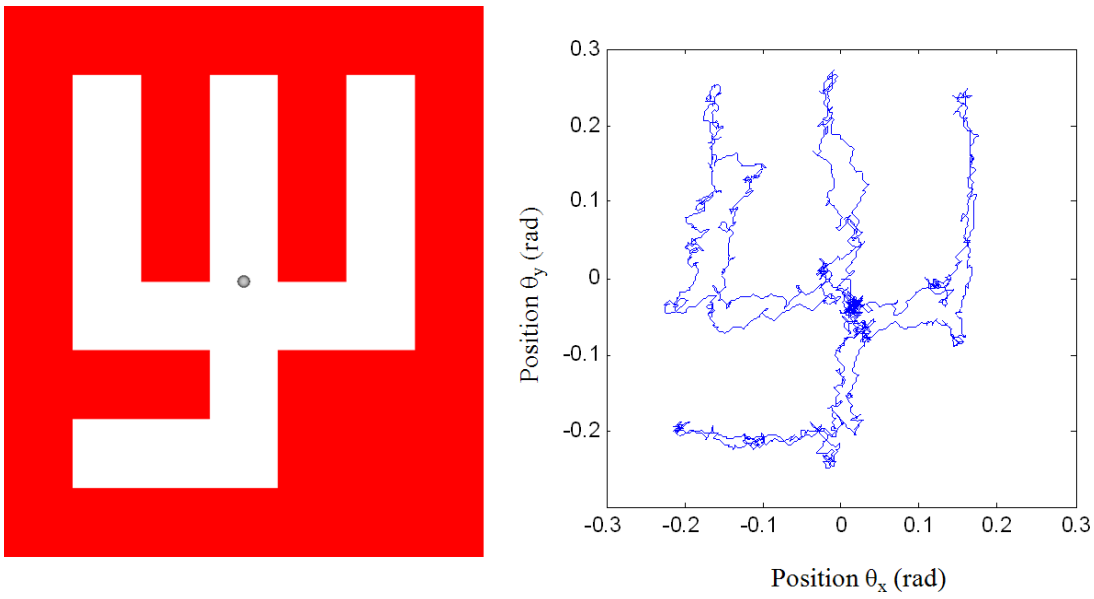

Figure 6.13. Virtual environment simulation for a manual gear shifter in an automobile (left). Recorded joystick positions as a user tries to shift gears with haptic feedback from the joystick (right).

6.2.7 Discussion

Similar to the rotary MR brake, hysteresis behavior can be observed in the torque/current curves (Figure 6.8). This behavior is due to the magnetization of steel elements in the MR brake [57]. Magnetization in ferromagnetic elements does not relax back to zero even if the magnetic field is removed. Unfortunately, this behavior not only adversely affects the controllability of the MR brake but also increases the off-state torque greatly. In our experiments the residual magnetization kept the off-state torque at 0.3 Nm after applying and removing 1.5A coil current. It caused unwanted off-state friction and reduced the backdrivability of the brake. To overcome this problem the controller was modified. At the instant the brake was turned off it was reactivated in the reverse direction with a very short impulse. An impulse with amplitude of 1A and 55 ms duration was found to be enough to collapse the residual magnetic field reducing the off-state torque to 0.1 Nm from 0.3 Nm.

Spherical MR brake was also able to simulate Coulomb friction with good accuracy (Figure 6.12).

Maximum torque that can be applied on "x" and "y" axes was found experimentally to be 3.7 Nm. FEM simulations predicted it to be 3.28 Nm. The 11.4% difference is probably due to friction forces from the O-Ring seal combined with the increased contact force between the ball and socket due to the present magnetic field.

First order system response was observed during the activation of the brake. Time constant was found to be approximately 170ms regardless of the applied current. At higher torques there was visible deflection on the joystick handle and it might have adversely affected the transient response of the system.

Virtual environment simulation using the manual gear shifter revealed that the joystick could create very realistic contact with the virtual surfaces. Our experiments with the virtual wall simulation produced a very crisp reaction force upon initial contact and very high rigidity at the quasi-static contact with the wall (vertical part of the curve in Figure 6.9). However several artifacts on force feedback were observed due to the purely passive nature of the device. The most significant was the high friction on the virtual surfaces. Since passive devices can only create forces against the user's direction of motion, it is impossible to create frictionless wall surfaces. After the initial contact with the wall, if the user wanted to slide on the wall surface, the brake had to be kept engaged in order to prevent further penetration into the wall. This resulted in friction forces that were as high as contact forces on virtual surfaces. Another artifact was the problem caused by noise in the optical positioning system. When the joystick was kept very close to the wall surface, the noise in the positioning system caused the tracker to penetrate the

wall surface even though no motion was present in that direction. Since demagnetization was performed after each wall collision to increase the backdrivability of the device, it resulted in slight magnetization in the opposite direction or friction due to the combined effect of the demagnetization pulses. This problem can be avoided in the future by using a different positioning system or using optical sensors with better noise characteristics.

6.3 Passive Haptic Interface Experiments

Two set of experiments were conducted with the developed dental implant aid system. The first set involved characterization of the device in displaying rigid virtual objects. The second set involved analysis of the overall accuracy of manipulation tasks with the system as a group of users tried to drill holes in polyurethane foam simulating the dental implant surgery.

6.3.1 Virtual Wall Collision

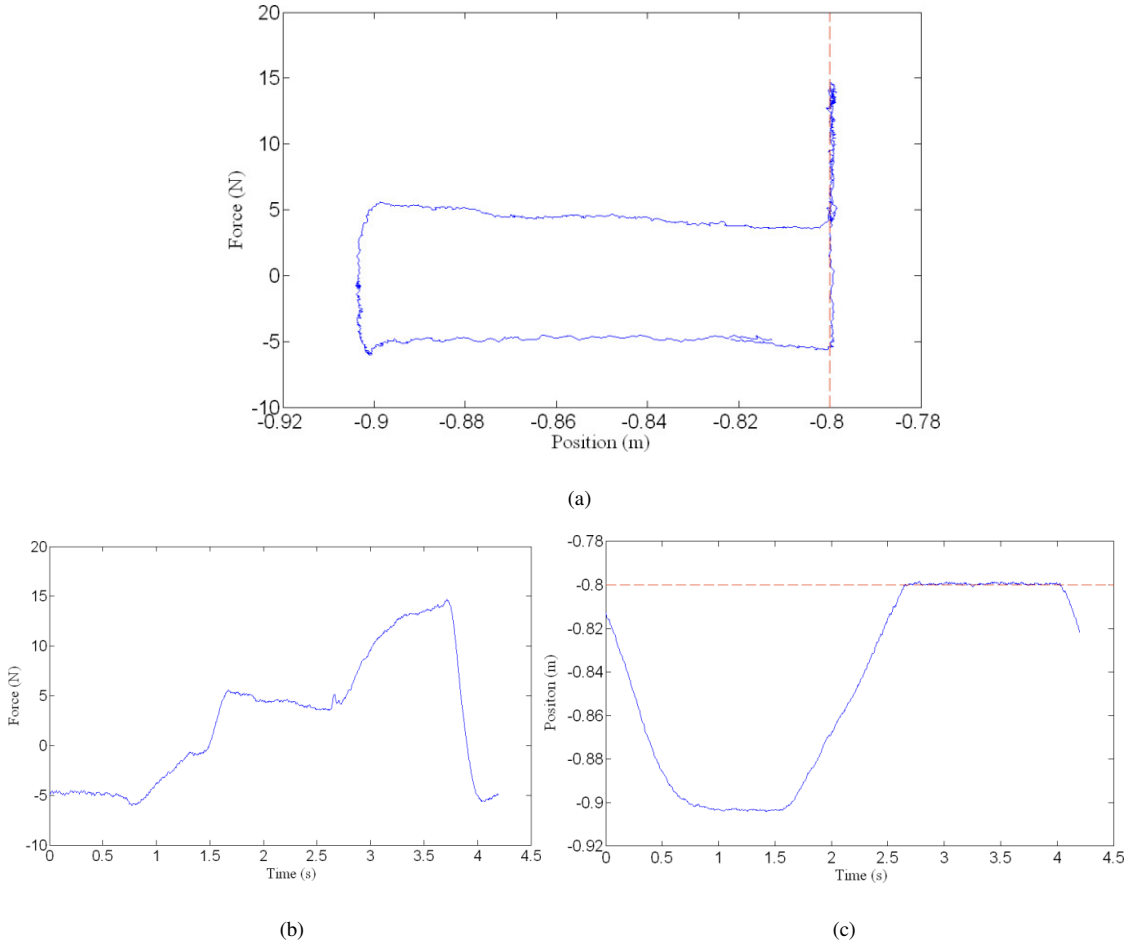

Figure 6.14. Collision of the tip with a virtual wall.

Wall collision experiments were conducted for a very stiff wall ($k = 10\ N/mm$). A wall surface was created at 0.8 m using H3DAPI (Figure 6.14). Starting at 0.9 m the hand-piece of the haptic arm was moved towards the wall until the tip made contact with the wall. As the tip was pressed into the wall, the force felt in the user's hand increased to about 15 N. Then, the contact with the wall was kept for about 1 second and the hand-piece was moved away from the wall back to the 0.9 m position.

The results show very rigid wall collision with clean release. However, as it can be seen on Figure (6.14) there is significant off-state friction. This off-state friction is mainly due to magnetization of steel elements inside the MR brake leaving a residual magnetic field over the MR fluid, hence higher off-state torques even when the current to the brake is turned off. Previously, we were able to collapse the residual magnetic field by giving a reverse current pulse to the brake (Figure 6.4a). This reduced the off-state torque from about 10% of the full torque range down to about 1%. This result was encouraging but had limitations. It is nearly impossible to implement this approach in applications where the MR-brake needs to apply variable torque as an actuator. In the duration of the reverse pulse the brakes cannot be engaged. Tasks such as wall following become very difficult since they require continuous brake control.

6.3.2 Virtual Wall Following

Wall following experiments were conducted to analyze the haptic arm's ability to simulate moving over a virtual wall surface. A virtual environment containing flat walls were created using H3DAPI. The experiment consisted of dragging the tracker (virtual arm tip) along the virtual wall surface.

Because of the force approximation in the control system, the haptic arm showed varying wall following performance at different locations in its work volume. If the mechanism was at a configuration such that the force vector created by the haptic device could be rendered normal to the virtual wall surface then frictionless walls could be rendered. However if the mechanism was in a configuration such that the force vector contained tangential and normal components, then the reality of the wall following task suffered. This was because of the passive MR brakes on the haptic arm, which limited the direction of the force vector to certain angles according to the wall and the user force vector directions.

In order to demonstrate this phenomenon the experiment was conducted at two different zones inside the work volume. In one zone the system could display smooth walls while in the other it could not.

6.3.2.1 Smooth Wall Display

A vertical virtual wall with ($k = 0.5\ N/mm$) was created on y = -0.8 m plane. The "y" and "z" coordinates of the wall following task can be seen in Figure 6.15.

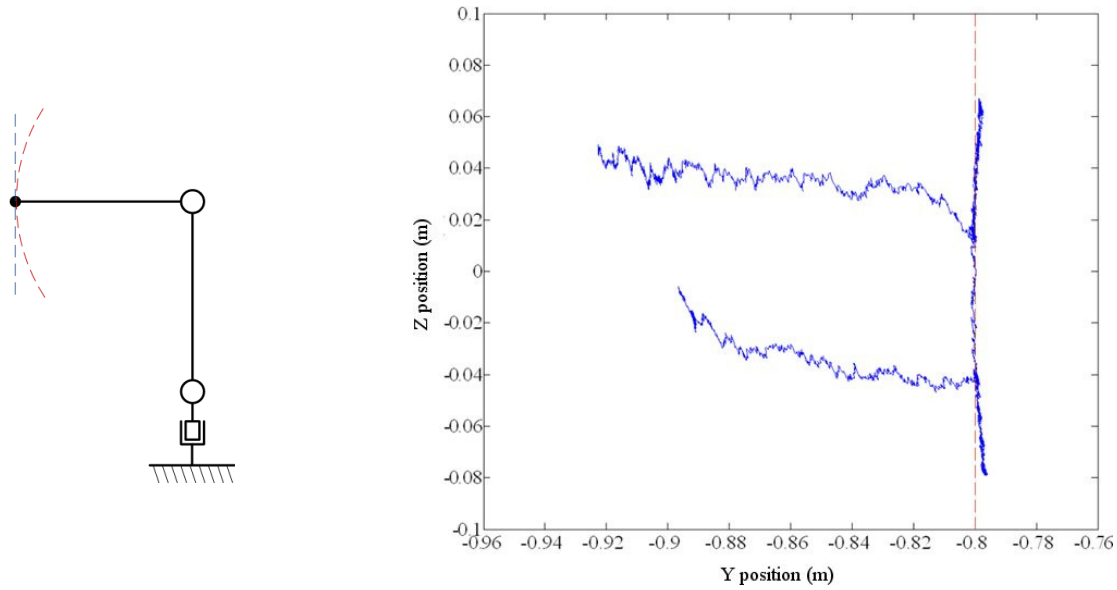

(a) (b)

Figure 6.15. Smooth wall display.

6.3.2.2 Unsmooth Wall Display

A horizontal virtual wall with ($k = 0.5\ N/mm$) was created on z = 0 plane. The "y" and "z" coordinates of the wall following task can be seen in Figure 6.16.

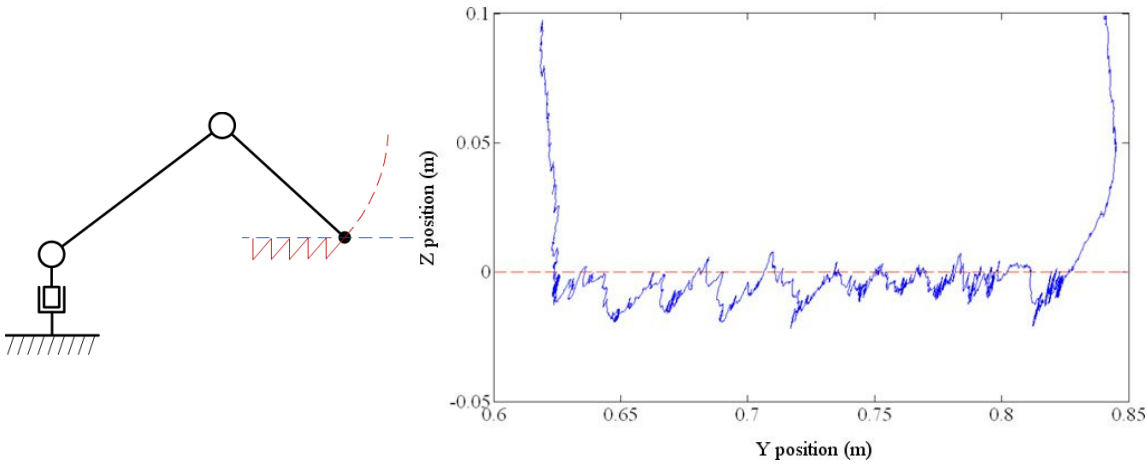

(a) (b)

Figure 6.16. Unsmooth wall display.

Figures 6.15b and 6.16b reveal a significant difference in the rendered wall quality. Figure 6.15b shows a smooth wall surface -albeit slightly curved-, whereas Figure 6.16b shows a "jagged" wall. Both of these shapes are the result of the force approximation algorithm. For the smooth wall display, the controller renders the wall almost frictionless by locking joint 2 at the same time releasing joints 1 & 3, resulting in the arc seen in Figure 6.15a. For the unsmooth wall display the controller does almost the same thing initially by locking joint 2 and releasing joints 1 & 3. However, the resulting arc is not parallel to the wall surface (Figure 6.16a). When the user drags the hand-piece along the wall surface, he/she is constrained on this arc, creating a much desired –although artificial- pullback action, at the same time giving the wall its "jagged" feeling.

6.3.3 Drilling with Haptic Feedback

6.3.3.1 Objective

The goal of this experiment was to analyze the overall accuracy of manipulation tasks with the system. The experiment involved drilling holes in polyurethane foam simulating the dental implant surgery. The hypothesis was that the passive haptic device would result in positioning accuracies similar to or better than the accuracies of other dental surgery systems.

6.3.3.2 Procedure

Twenty one users (18 male and 3 female) performed the usability experiment. Each user first went through a training session where the experiment setup was introduced. The users then performed a trial run where they placed holes at 3 different

locations. No data was collected during the trial run and the hole locations were different than the actual experiment.

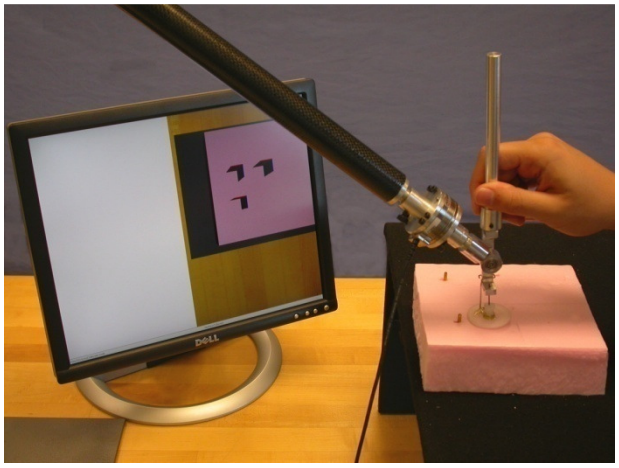

Figure 6.17. Usability experiments

Following the training, the real placement task was performed 3 times by each user. The hole placement order was randomized to prevent any task learning. There was no time constraint on the experiment. In between trials, the user was allowed to rest his/her arm for one minute. Users were instructed to drill three holes with the assistance of the haptic feedback coming from the device (Figure 6.17). Hole locations were guided by virtual constraints that resembled angle brackets in the virtual environment (Figure 6.18). The corner of each virtual bracket was aligned with the axis of a hole. The users moved the hand-piece to position the tracker (virtual tip) near a guide. After that, they pressed the tracker against both walls of the virtual bracket and felt the haptic feedback in their hand to locate the x and y positions of the hole. To successfully guide the drill bit along the axis, the users had to keep the tracker in contact with the bracket through haptic feedback in their hand as they moved the bit down towards the foam. The z-depth of the holes was fixed by a horizontal virtual wall inside the foam. As the user continued to

penetrate the foam, the arm locked up when the required depth was reached by the drill bit. A total of 3 holes had to be drilled for each placement task. The holes were located 50mm apart in an "L" shaped arrangement and the depth was limited at 4 mm.

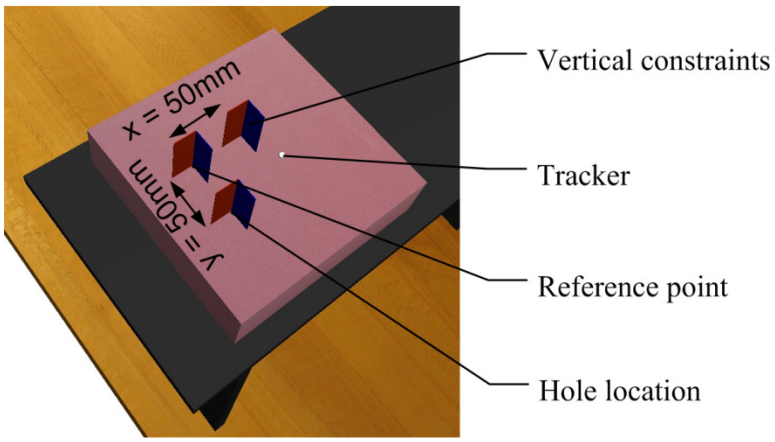

Figure 6.18. Virtual environment for haptic hole placement

6.3.3.3 Results

After the experiment the hole locations were carefully measured using a caliper. In each measurement deviation from actual dimensions ($x = y = 50mm$ & $z = 4mm$) was calculated as the positioning error. The average error for each dimension and the standard deviation are given in Table 6.1.

Table 6.1: Results of haptic drilling experiment

	Error	Standard deviation
x-axis	2.88mm	2.51mm
y-axis	1.90mm	1.46mm
z-axis	1.16mm	0.94mm

6.3.3.4 Discussion

An image-guided implantology system had an average error of 1.23 ± 0.28 mm and maximum error of 1.87 ± 0.47 mm [19]. Robot assistant systems report deviations of 1 - 2 mm [23, 24]. Our passive haptic system had errors below 2 mm for "y" and "z" axis and a little below 3 mm for the "x" axis. These results are on the same order of magnitude as the optical tracking system and other dental robots, hence passive haptic devices have potential to be a viable alternative to active (servo controlled) haptic devices.

Deflection was the primary cause for the errors. Although the haptic arm was built with deflection in mind by using materials such as steel, aluminum and carbon fiber as opposed to polymer based materials common in today's haptic devices, main cause of the errors was the deflection in the system. This became especially problematic in the x-axis direction as forces in this direction resulted in torsion of the mechanism out of the plane of the parallel links in the mechanism. This resulted in the highest average error among all three axes (2.88mm).

Another cause for the deviation –although not as significant as the first cause- was the lack of pull back action on the virtual walls. This is possible with haptic devices with active actuators such as motors. The passive actuators can only create resistance forces. If the user penetrated into the wall by pressing too hard, the system had no way of compensating for the error since it could not pull back the tip.

A final cause was the resistance force created by the foam due to the penetration of the drill bit. Some users mistook the haptic feedback for limiting the "z" depth as the resistance force of the foam and continued to press down looking for the haptic feedback

to stop. When the manipulator and the haptic master are the same device, haptic feedback forces and reaction forces from the environment are bound to overlap. This kind of effect would be more significant when drilling a more rigid object such as bone. A viable solution would be to measure the reaction forces coming from the environment and make necessary compensations in the haptic force feedback accordingly.

CHAPTER 7

CONCLUSIONS AND FUTURE RECOMMENDATIONS

A novel haptic interface with MR brakes for dental implant surgery has been built. As part of this research, rotary MR brakes with high torque output have been developed using the serpentine flux path technique. The design activates more surface area of the MR fluid in a given volume by weaving the magnetic flux through the MR fluid multiple times. Table 7.1 compares the design specifications of the rotary brake to a commercially available MR brake.

Table 7.1: Design Specifications of the Rotary MR-Brake

	Designed MR-Brake	(RD-2087-01 by LORD Corp.)
Diameter (mm)	63.5	96.6
Length (mm)	89.7*	43.7
Max. torque (Nm)	10.9	4.0
Max. off-state (Nm)	< 0.1	< 0.4
Max. current (A)	1.5	1.0
Time constant (ms)	60	-

*Includes ferro-fluidic seal end caps (27.0 mm).

The prototype MR brake is about 2.7 times more powerful than the commercially available RD-2087-01 rotary brake by Lord Corporation and about 33% smaller in diameter. Furthermore, with 10.9 Nm torque output, it is more powerful than the closest brake in the literature with 6.9 Nm torque [30] but only approximately half the diameter and requires 62.5% less current.

Another contribution of the research was a ferro-fluidic seal which reduced the

friction that would normally occur due to using conventional O-rings. The off-state friction was further reduced down to a negligible 0.08 Nm by applying a current pulse in the reverse direction. This improved the backdrivability of the brake which is much desired in haptics applications.

Current prototype is capable of rendering only 3-DOF (x-y-z position). In future studies, additional MR brakes can be added to the wrist joint to control the orientation, effectively building a 6-DOF haptic display. Potential solutions already exists where MR-brakes as small as a U.S. quarter [40] were previously designed. Another solution, which was explored in this research, is a spherical MR brake [25] that is capable of locking all 3-DOF at once. To the best of our knowledge, this design is the first ever multi-DOF spherical brake using MR fluid.

The prototype spherical MR brake has a diameter of 76.2 mm and can apply up to 3.7 Nm braking torque. Since the torque is proportional to the cube of the radius of the steel ball, the brake can scale up very well. Using this design it is possible to make much more powerful brakes without increasing the overall dimension of the brake significantly.

An optical position measurement system that eliminated the gimbal mechanisms that are typically used in spherical joints for position measurement was also developed as part of this research. However, the optical sensors turned out to be susceptible to noise leading to inaccuracies in the position measurements. Another method is necessary to measure the position of the steel ball in the brake.

Design options for the wrist joint using small rotary brakes or the spherical brake can be explored in a future study.

Experiments to identify the characteristics of the haptic interface for dental surgery have been conducted. Initial experiments show that passive haptic devices can be viable alternatives to active haptic devices.

During the haptic drilling experiments deflection caused positioning errors despite the rigid construction of the haptic arm. This is a challenging issue since the arm needs to be lightweight and the application requires very strict positioning accuracy. In the future we plan to explore options for closed loop position control using optical/magnetic trackers and/or a mathematical model of the deflection in order to compensate for the positioning error.

Passive haptic devices have advantages over active devices in terms of stability, rigid wall collision and inherent safety. They suffer from lack of pull back action on the virtual walls, unsmooth behavior at the wall surfaces and inability to compensate for positioning errors. All of these shortcomings can be overcome by designing devices that use hybrid passive-active actuators [26, 27, 56].

BIBLIOGRAPHY

[1] Fortin, T., Isidori, M., Blanchet, E., Perriat, M., Bouchet, H. and Coudert, J. L. "An image-guided system-Drilled surgical template and trephine guide pin to make treatment of completely edentulous patients easier: A clinical report on immediate loading." Clinical Implant Dentistry and Related Research. 6(2). Pages: 11-119. 2004

[2] Bartling, R., Freeman, K. & Kraut, R.A. "The incidence of altered sensation of the mental nerve after mandibular implant placement." Journal of Oral and Maxillofacial Surgery 57: 1408–1412. 1999

[3] Ellies, L.G. "Altered sensation following mandibular implant surgery: a retrospective study." Journal of Prosthetic Dentistry 68: 664–671. 1992

[4] Serhal, C. B., Steenberghe, D., Quirynen, M. and Jacobs, R. "Localisation of the mandibular canal using conventional spiral tomography: a human cadaver study." In Clinical Oral Implants Research. 12(3). Pages 230-236. 2001

[5] Berberi, A., Le Breton, G., Mani, J., Woimant, H. & Nasseh, I. "Lingual paresthesia following surgical placement of implants: report of a case." International Journal of Oral and Maxillofacial Implants 8: 580–582. 1993

[6] Berglundh, T., Persson L. and Klinge B. "A systematic review of the incidence of biological and technical complications in implant dentistry reported in prospective longitudinal studies of at least 5 years." Journal Of Clinical Periodontology. 29(3). Pages: 197-212. 2002

[7] Gray 's Anatomy. 20th US Edition. 1918

[8] Brief, J., Edinger, D, Hassfeld, S, Eggers, G. "Accuracy of image-guided implantology." Clinical Oral Implants Research, Volume 16, Number 4, August 2005 , pp. 495-501(7)

[9] Buser, D., Martin, W., Belser, U. C. "Optimizing esthetics for implant restorations in the anterior maxilla: Anatomic and surgical considerations." Int J Oral Maxillofac Implants. 19(7). Pages: 43–61. 2004

[10] Lal, K., White, G. S., Moreaand, D. N., Wright, R. F. "Use of stereolithographic templates for surgical and prosthodontic implant planning and placement." Part I. The Concept. Journal of Prosthodontics. 15(1). Pages 51-58. 2006

[11] SurgiGuide, Materialize Medical. Available: [Online] http://www.materialise.com Accessed: October, 2009

[12] CompuSurge Template, Implant Logic Systems. Available: [Online] http://www.ipr.ira.uka.de/compusurge/ Accessed: October, 2009

[13] Simplant, Materialize Medical. Available: [Online] http://www.materialise.com Accessed: October, 2009

[14] Klein, M., Abrams, M. “Computer-guided surgery utilizing a computer-milled surgical template.” Pract Proced Aesthet Dent. 2001 Mar;13(2):165-9

[15] Sarment, D. P., Sukovic, P., Clinthorne., N. “Accuracy of implant placement with a stereolithographic surgical guide.” The International Journal of Oral & Maxillofacial Implants. 18(4). 2003

[16] Ewers, R., Truppe, M., Reichwein, A., Wagner A. “Computer-aided navigation in dental implantology: 7 years of clinical experience.” Journal of Oral and Maxillofacial Surgery, Volume 62, Issue 3, Pages 329-334

[17] Robodent, Robodent GmbH. Available: [Online] http://www.robodent.com/ Accessed: October, 2009

[18] IGI Denx, Image Navigation Ltd. Available: [Online] http://www.denx.com/ Accessed: October, 2009

[19] Birkfellner, W., Solar, P., Gahleitner, A., Huber, K., Kainberger, F., Kettenbach, J., Homolka, P., Diemling, M., Watzek, G., Bergmann, H.. “In-vitro assessment of a registration protocol for image guided implant dentistry.” Clin Oral Implants Res.;12(1):69-78. 2001

[20] Lueth, T.C.; Hein, A.; Albrecht, J.; Demirtas, M.; Zachow, S.; Heissler, E.; Klein, M.; Menneking, H.; Hommel, G.; Bier, J., "A surgical robot system for maxillofacial surgery," Industrial Electronics Society, 1998. IECON '98. Proceedings of the 24th Annual Conference of the IEEE , vol.4, no., pp.2470-2475 vol.4, 31 Aug-4 Sep 1998

[21] Kusumoto, N., Sohmura, T., Yamada, S., Wakabayashi, K., Nakamura, T., Yatani, H. “Application of virtual reality force feedback haptic device for oral implant surgery.” Clinical Oral Implants Research, 17(6), Pages 708-713, 2006

[22] PHANToM, Sensable Technologies, Inc. Available: [Online] www.sensable.com Accessed: October, 2009

[23] Brief, J, Hassfeld, S, Redlich, T, et al. “Robot-assisted insertion of dental implants—a clinical evaluation.” Lemke HU, Vannier MW, Inamura K, Farman A, eds. Computer assisted radiology and surgery. Proceedings of the 14th International Congress and Exhibition, 28 June–1 July 2000, San Francisco, CA. Amsterdam: Elsevier, 2000: 932–937.

[24] Boesecke, R., Brief, J., Raczkowsky, J., Schorr, O., Daueber, S., Krempien, R., Treiber, M., Wetter, T., and Haßfeld, S. 2001. “Robot sssistant for dental implantology.” In Proceedings of the 4th international Conference on Medical Image Computing and Computer-Assisted intervention (October 14 - 17, 2001). W. J. Niessen and M. A. Viergever, Eds. Lecture Notes In Computer Science, vol. 2208. Springer-Verlag, London, 1302-1303.

[25] Senkal, D. and Gurocak, H.B. 2009. “Spherical brake with MR fluid as multi degree of freedom actuator for haptics”, Journal of Intelligent Material Systems and Structures (In press).

[26] An, J. and Kwon, D.S.. "Five-bar linkage haptic device with DC motors and MR brakes." In Journal of Intelligent Materials Systems and Structures, 00:1-12, 2008.

[27] An, J. and Kwon, D.S. "Haptic experimentation on a hybrid active/passive force feedback device." In Proceedings of the IEEE Int. Conf. on Robotics and Automation (Washington DC, May 2002).

[28] Nam, Y.J. and Park, M.K. "A hybrid haptic device for wide-ranged force reflection and improved transparency." In Proceedings of the Int. Conf. on Control, Automation and Systems (Seoul, Korea, October 17-20, 2007).

[29] Reed, M. and Book, W. "Modeling and control of an improved dissipative passive haptic display." In Proceedings of the Int. Conf. on Robotics and Automation (New Orleans, LA, April 2004).

[30] Carlson, J.D., Leroy, D.F., Holzheimer J.C., Prindle, D.R. and Marjoram R.H. "Controllable Brake." US Patent No.: 5,842,547 (December, 1998)

[31] Kavlicoglu, B., Gordaninejad, F., Evrensel, C., Cobanoglu, N., Liu, Y. and Fuchs, A. "A high-torque magneto-rheological fluid clutch." In Gregory S. Agnes editor, Smart Structures and Materials 2002: Damping and Isolation, Proceedings of SPIE (vol. 4867, 2002).

[32] Demersseman, R., Hafez M., Lemaire-Semail, B. and Clenet, S. "Magnetorheological brake for haptic rendering." In M. Ferre editor, Proceedings of the EuroHaptics 2008 (Spain, 2008).

[33] Li, W.H. and Du., H. "Design and experimental evaluation of magnetorheological brake." In Int. Journal of Manufacturing Technology, vol. 21, pages 508-515, 2003.

[34] Nam, Y.J, Moon Y.J. and Park. M.K. "Performance improvement of a rotary MR fluid actuator based on electromagnetic design." In Journal of Intelligent Materials Systems and Structures, vol. 19, pages 695-705, June 2008.

[35] Li, W.H., Liu, B., Kosasih, P.B. and Zhang, X.Z. 2007. "A 2-DOF MR actuator joystick for virtual reality applications," Sensors and Actuators A: Physical, 137(2):308-320.

[36] Yamaguchi, Y., Furusho, J., Kimura S. and Koyanagi K. 2005. "Development of high-performance MR actuator and its application to 2-D force display," International Journal of Modern Physics B, 19,(7-9):1485-1491.

[37] Han, Y.M., Kang, P.S., Sung, K.G. and Choi, S.B. 2007. "Force feedback control of a medical haptic master using an electrorheological fluid," Journal of Intelligent Material Systems and Structures, 18(12):1149-1154.

[38] Bose, H. and Berkemeier, H.J. 1999. "Haptic device working with an electrorheological fluid," Journal of Intelligent Material Systems and Structures, 10(9):714-717.

[39] Senkal, D. and Gurocak, H.B. 2009. "Compact MR-brake with serpentine flux path for haptics applications," World Haptics 2009 - Third Joint EuroHaptics conference and Symposium on Haptic Interfaces for Virtual Environment and Teleoperator Systems, Salt Lake City, Utah, 91-96

[40] Blake, J. and Gurocak, H.B. 2009. "Haptic glove with MR brakes for virtual reality," IEEE/ASME Transactions on Mechatronics (In press).

[41] H3DAPI, Sensegraphics AB. Available: [Online] http://www.sensegraphics.com/ Accessed: October, 2009

[42] Ruspini, D. C., Kolarov, K. and Khatib, O. 1997. "The haptic display of complex graphical environments," Proceedings of the 24th Annual Conference on Computer Graphics and interactive Techniques, ACM Press/Addison-Wesley Publishing Co., New York, NY, 345-352

[43] Cho, C., Kim, M. Song, J.B., "Direct control of a passive haptic device based on passive force manipulability ellipsoid analysis", International Journal of Control, Automation and Systems. 2(2). Pages 238-246. 2004

[44] Cho, C., Song, J.B., Kim, M, Hwang, C.S., "Energy-based control of a passive haptic device," Robotics and Automation, 2004. Proceedings. ICRA '04. 2004 IEEE International Conference on , vol.1, no., pp. 292-297 Vol.1, 26 April-1 May 2004

[45] Infolytica Corp. [Online]. Available: http://www.infolytica.com/ Accessed: October, 2009

[46] Lord Corp. [Online]. Available: http://www.lord.com/ Accessed: October, 2009

[47] Tsumaki, Y., Naruse, H., Nenchev, D.N. and Uchiyama, M. 1998. "Design of a compact 6-DOF haptic interface," Proceedings of the 1998 IEEE International Conference on Robotics & Automation, Leuven, Belgium, vol.3, 2580-2585

[48] Rosenberg, L. B. and Adelstein, B. D. 1993 "Perceptual decomposition of virtual haptic surfaces," Proceedings, IEEE Symposium on Research Frontiers in Virtual Reality, IEEE Computer Society Press, Los Alamitos CA, 46-53

[49] MathWorks Inc. [Online]. Available: http://www.mathworks.com/

[50] Bourns, Inc. Available: [Online] http://www.bourns.com/ Accessed: October, 2009

[51] Quanser. Available: [Online] http://www.quanser.com/ Accessed: October, 2009

[52] ATI Industrial Automation, Inc.. Available: [Online] http://www.ati-ia.com/ Accessed: October, 2009

[53] National Instruments. Available: [Online] http://www.ni.com/ Accessed: October, 2009

[54] Sakaguchi, M.; Furusho, J.; Takesue, N., "Passive force display using ER brakes and its control experiments," Virtual Reality, 2001. Proceedings. IEEE , vol., no., pp.7-12, 17-17 March, 2001

[55] Advanced Motion Controls. [Online]. Available: http://www.a-m-c.com Accessed: October, 2009

[56] An J. and Kwon D.S., "Stability and Performance of Haptic Interfaces with Active/Passive Actuators – Theory and Experiments." In Int. Journal of Robotics Research, vol. 25, no.11, pages 1121-1136, November, 2006

[57] Liu B.,Li WH., Kosasih P. B. and Zhang X. Z.. "Development of an MR-brake-based haptic device." In Smart Materials and Structures. vol. 15, no 6, pages 1960-1966, 2006.

[58] Web3D Consortium. [Online]. Available: http://www.web3d.org/ Accessed: October, 2009

APPENDIX A: ASSEMBLY DRAWINGS

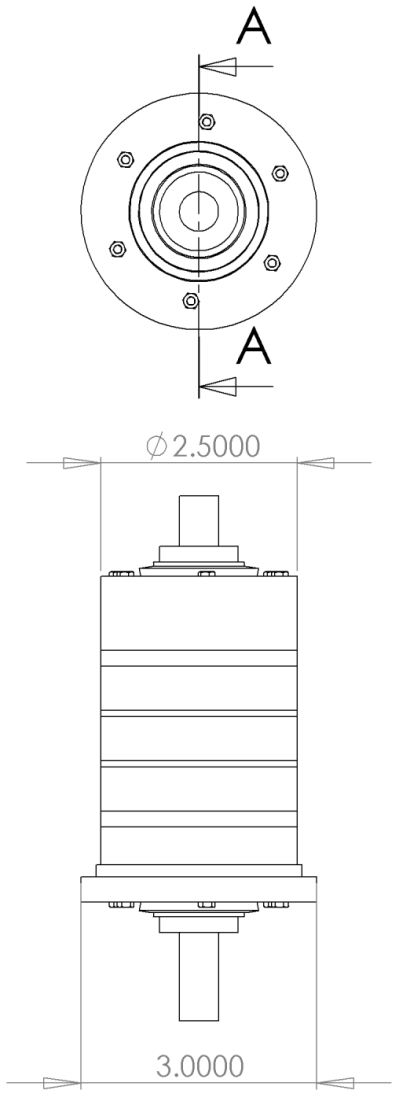

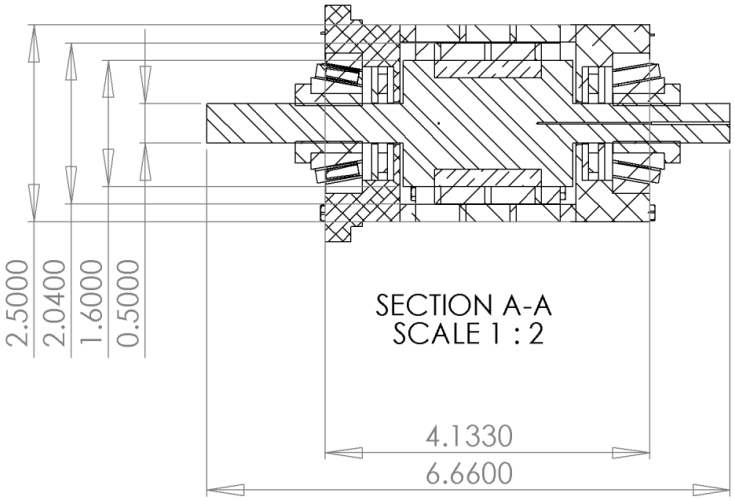

Serpentine MR Brake	
Washington State University	
Scale: 1:2	Drawn by: Doruk Senkal
Cross section	Date: 10/6/2009

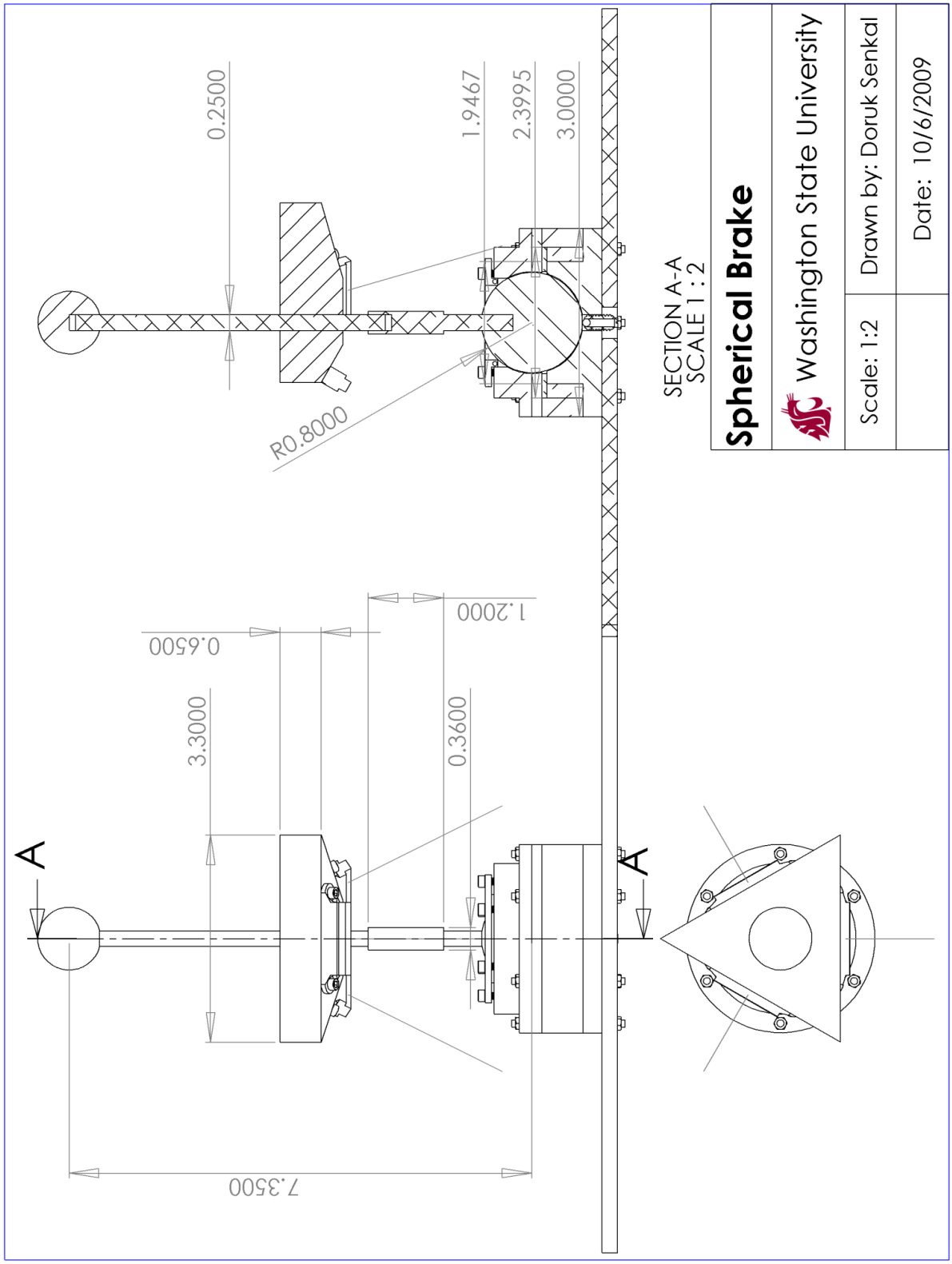
Spherical Brake
Washington State University
Scale: 1:2
Drawn by: Doruk Senkal
Date: 10/6/2009
SECTION A-A
SCALE 1 : 2
0.2500
1.9467
2.3995
3.0000
R0.8000
1.2000
0.6500
3.3000
0.3600
7.3500
A
A

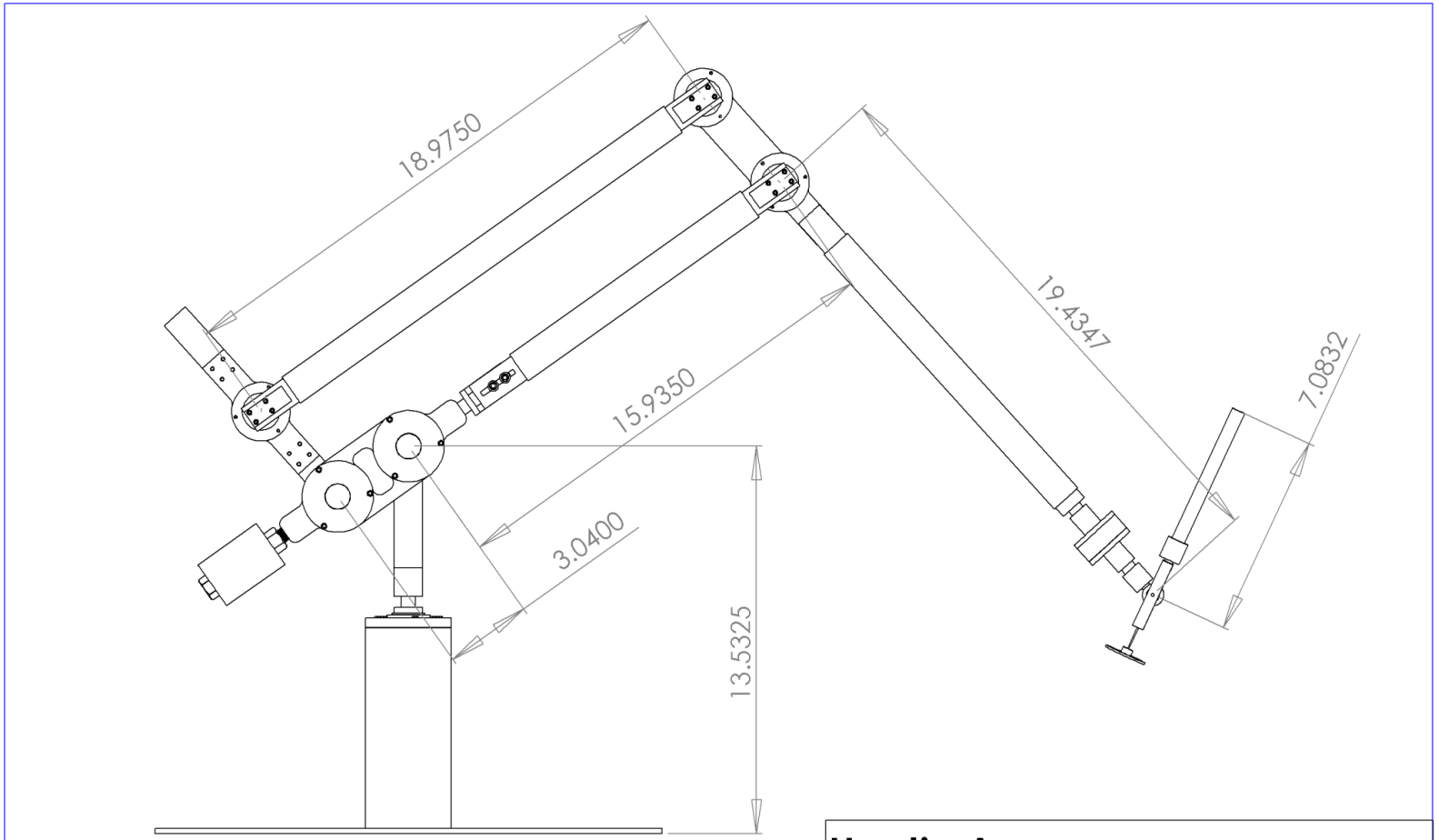

Haptic Arm	
Washington State University	
Scale: 1:5	Drawn by: Doruk Senkal
Front View	Date: 10/6/2009

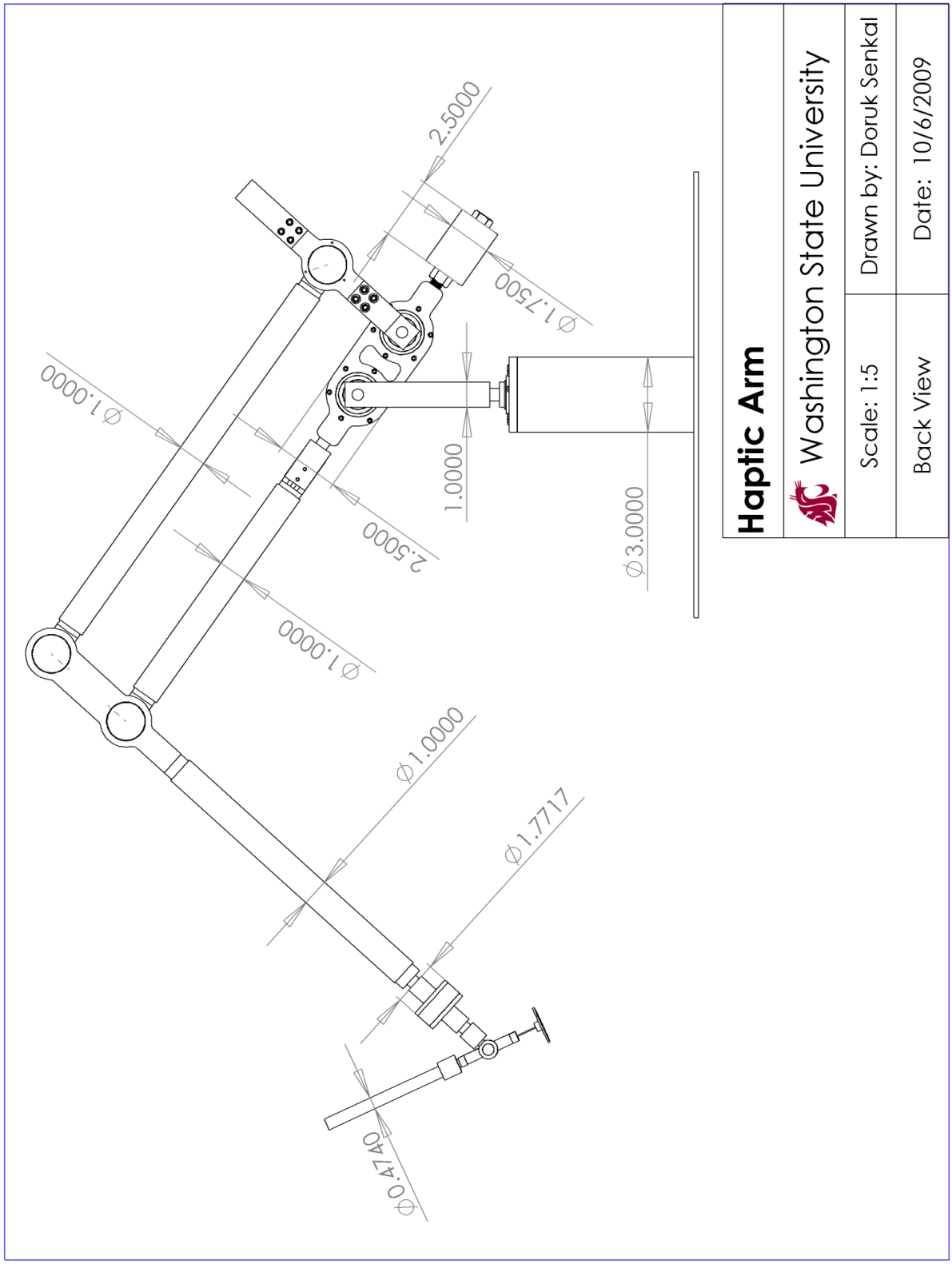
Haptic Arm
Washington State University
Scale: 1:5
Drawn by: Doruk Senkal
Back View
Date: 10/6/2009
2.5000
Ø1.7500
Ø1.0000
1.0000
2.5000
Ø1.0000
Ø3.0000
Ø1.0000
Ø1.7717
Ø0.4740

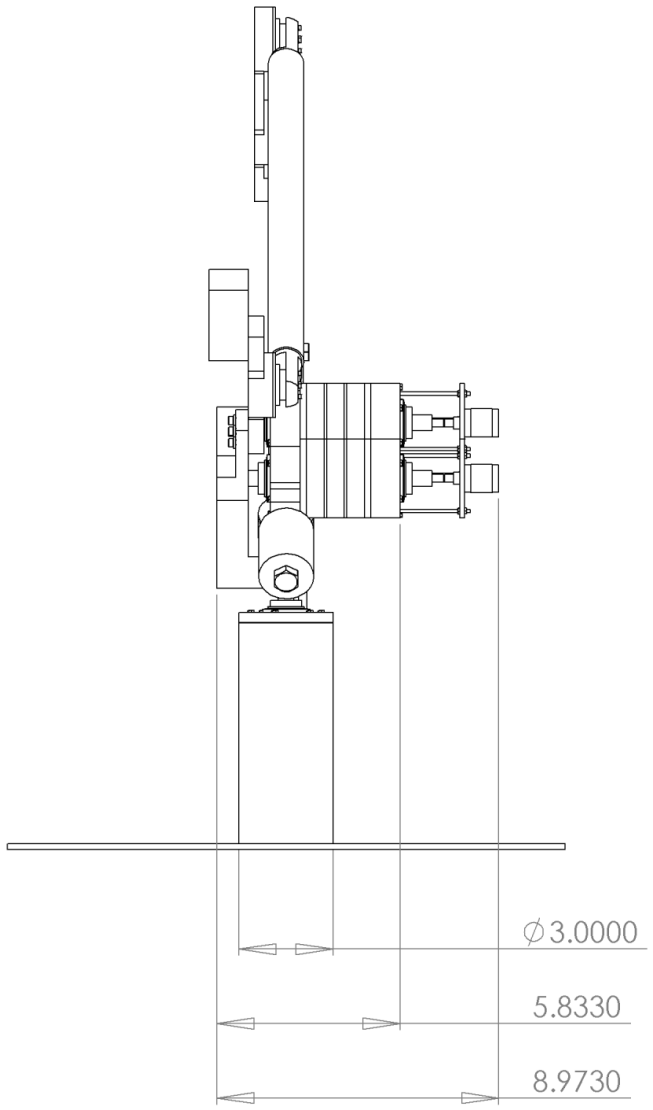

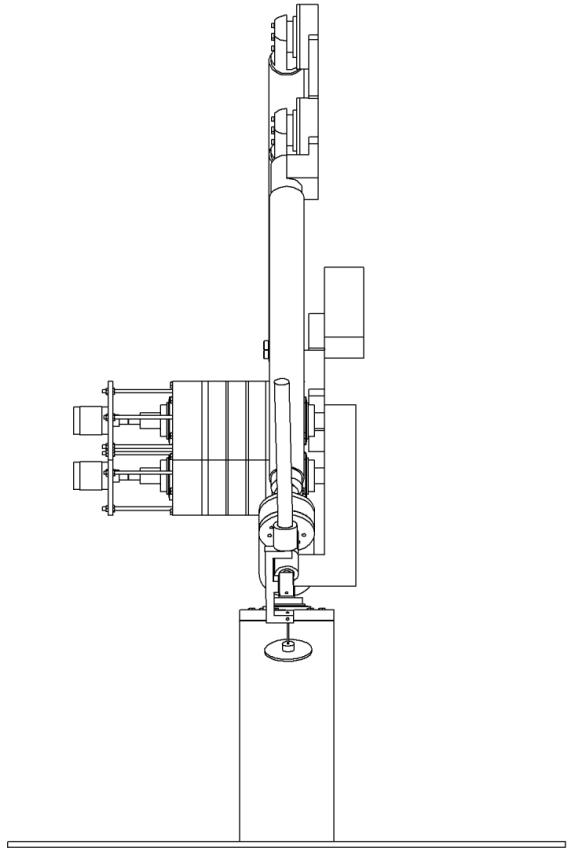

Haptic Arm	
Washington State University	
Scale: 1:5	Drawn by: Doruk Senkal
Left & Right View	Date: 10/6/2009

Rev.	Description	Initiator	Date
01	Initial Drawing	JCP	4/20/2007
02	Reduced TAP interface depth, change dowel pos'tol	PPF	8/6/2007

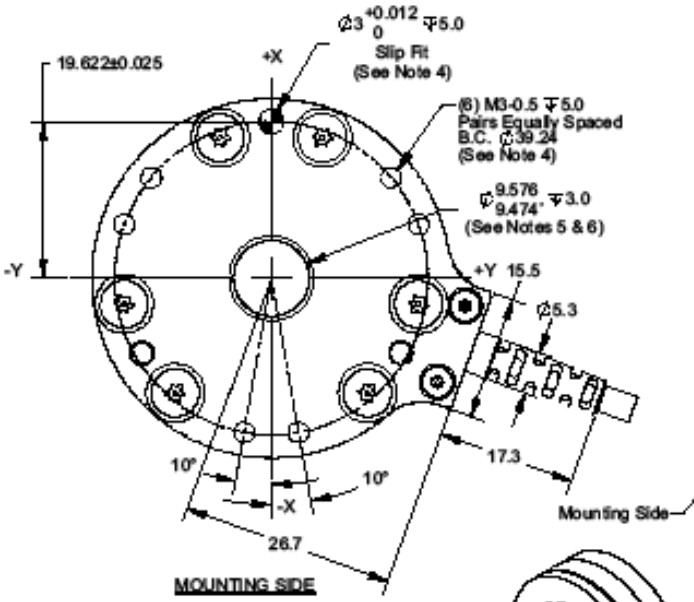

MOUNTING SIDE

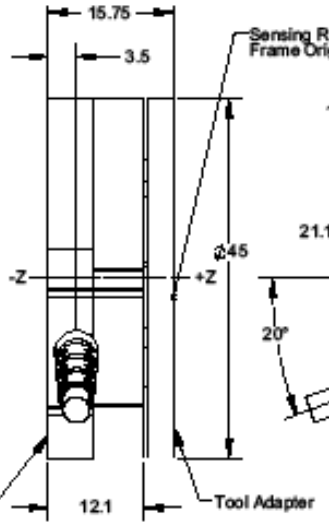

SIDE VIEW

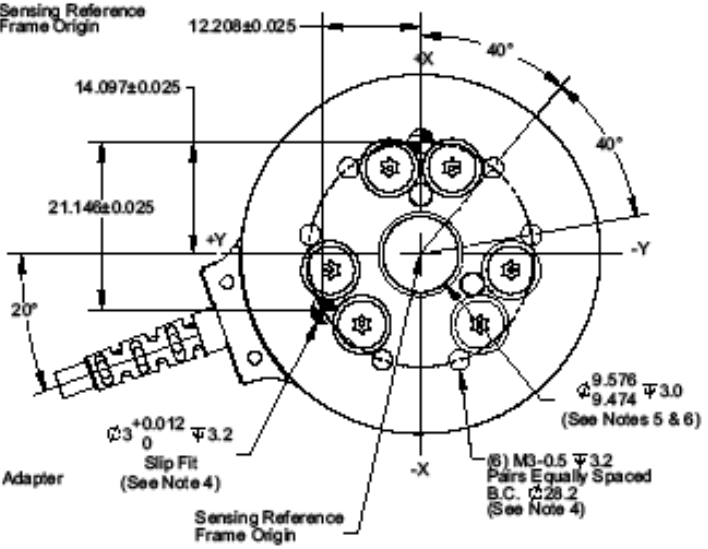

TOOL SIDE

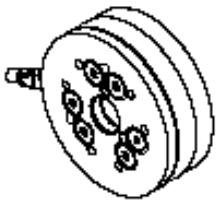

ISOMETRIC VIEW

NOTES:
1. Mounting and tool adapter made of aluminum. Transducer made of hardened stainless steel.
2. Use M3 tapped holes, dowel pin holes and center hole for mounting adapter interfacing. Use M3 tapped holes and dowel pin holes for tool adapter interfacing.
3. **WARNING: DO NOT LOOSEN OR REMOVE INTERFACE PLATES DUE TO POTENTIAL DAMAGE**
4. **DO NOT EXCEED INTERFACE DEPTH MAY CAUSE DAMAGE.**
5. Thru hole diameter is 9.4mm. Specified tolerances are for mating to a boss.
6. Do not allow items passing through to contact either side of transducer. Contact will affect reading accuracy.
7. Connector (not shown) has 17mm diameter and is 67.5mm long.

NOTES: UNLESS OTHERWISE SPECIFIED

DO NOT SCALE DRAWING. DRAWN IN SOLIDWORKS.
ALL DIMENSIONS ARE IN MILLIMETERS.

3rd ANGLE PROJECTION

ATI INDUSTRIAL AUTOMATION
1031 Goodworth Drive, Apex, NC 27539, USA
Tel: +1.919.772.0115 Email: info@ati-ia.com
Fax: +1.919.772.8259 www.ati-ia.com
ISO 9001 Registered Company

DRAWN BY:	J. Parker 1/10/07
CHECKED BY:	P. Fusco 1/10/07
WEIGHT LBS:	
ASSEMBLY SW:	
TITLE:	Mini45-E Transducer with Strain Relieved Cable
SCALE:	2:1
SIZE:	B
DRAWING NUMBER:	9230-05-1315-02
PRODUCT RELEASE #	
DATE:	
SHEET	1 OF 1

APPENDIX B: SOFTWARE

B.1 SOFTWARE FOR SPHERICAL MR BRAKE

B.1.1 Spherical Brake Simulink Diagram

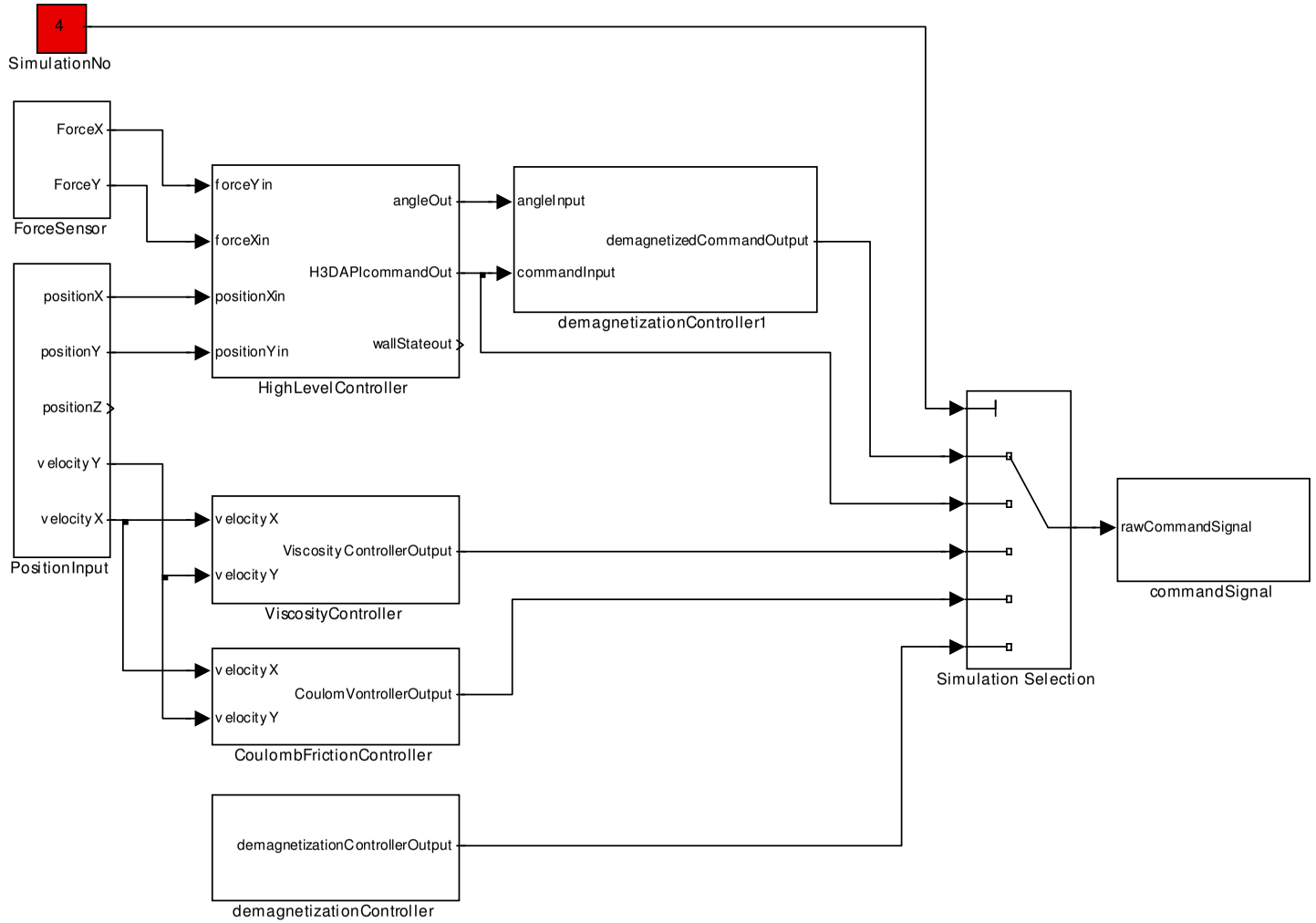

B.1.1.1 Force Sensor Sub-system

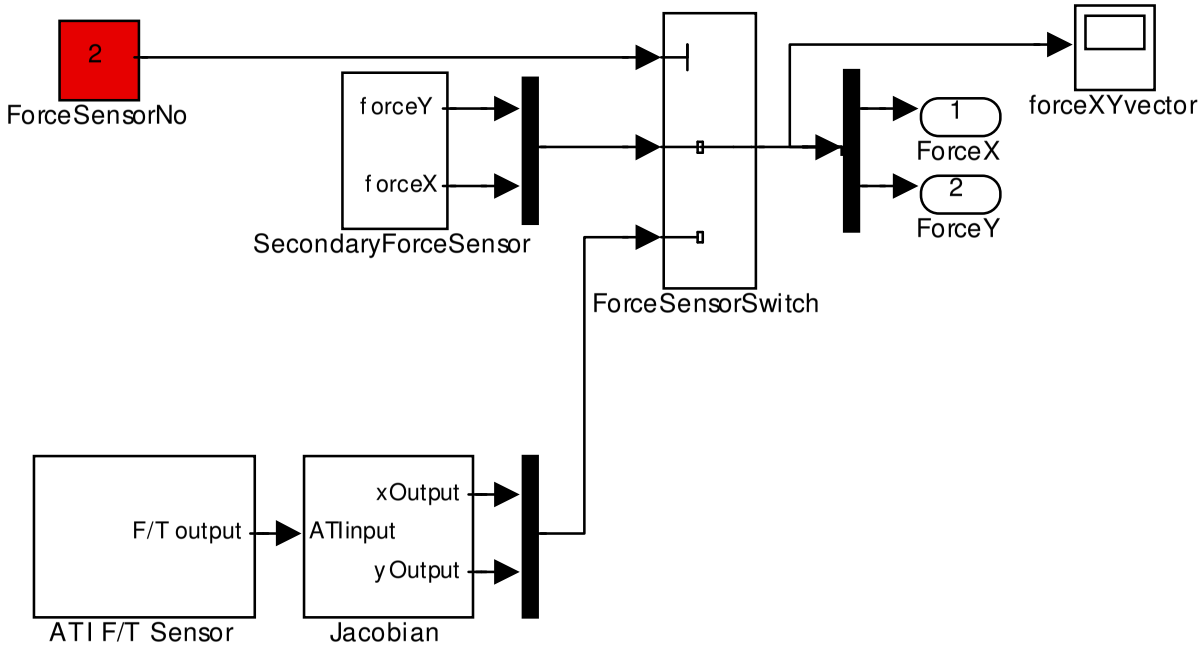

B.1.1.2 SecondaryForceSensor Sub-system

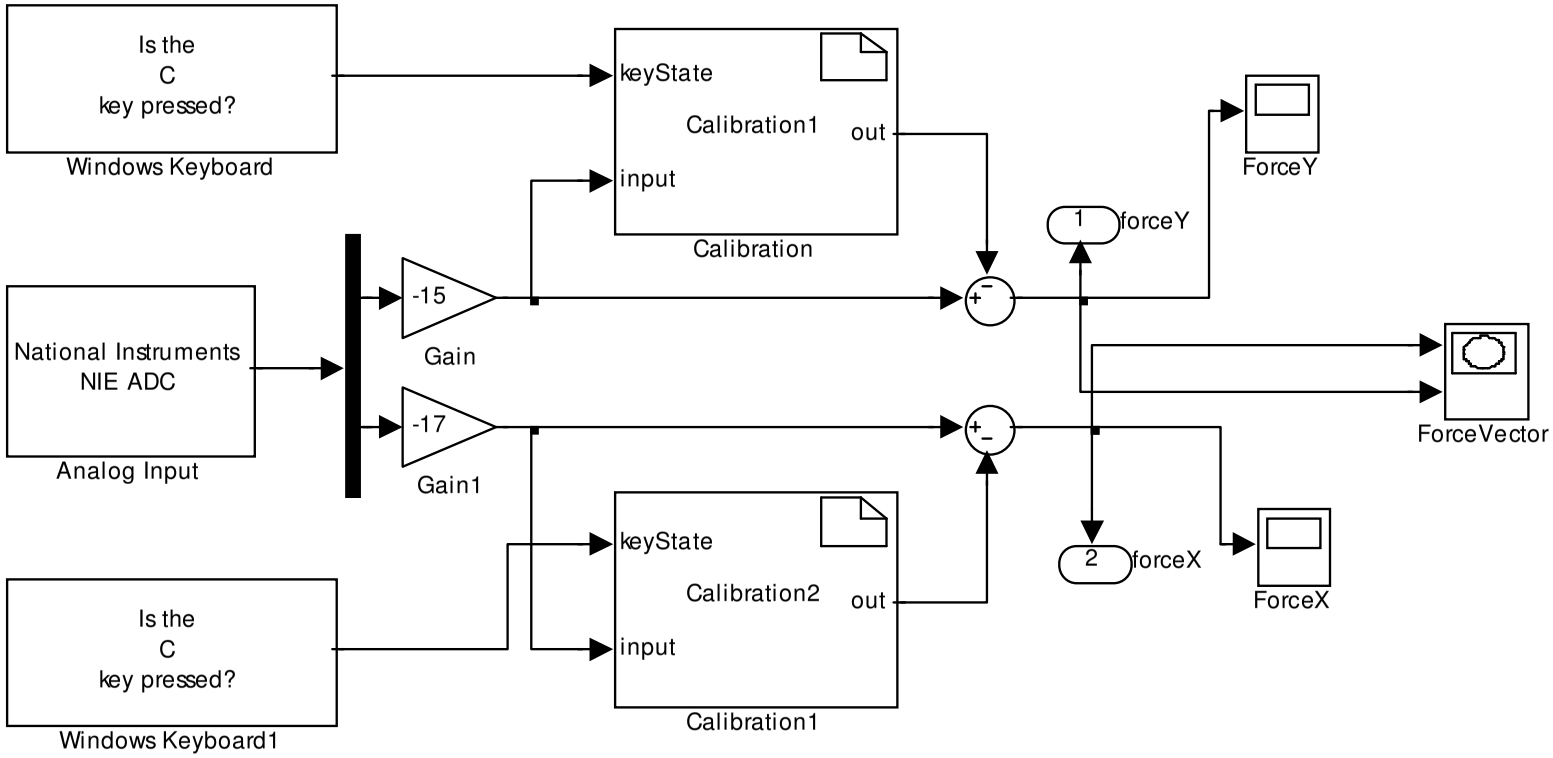

B.1.1.3 ATI F/T Sensor Sub-system

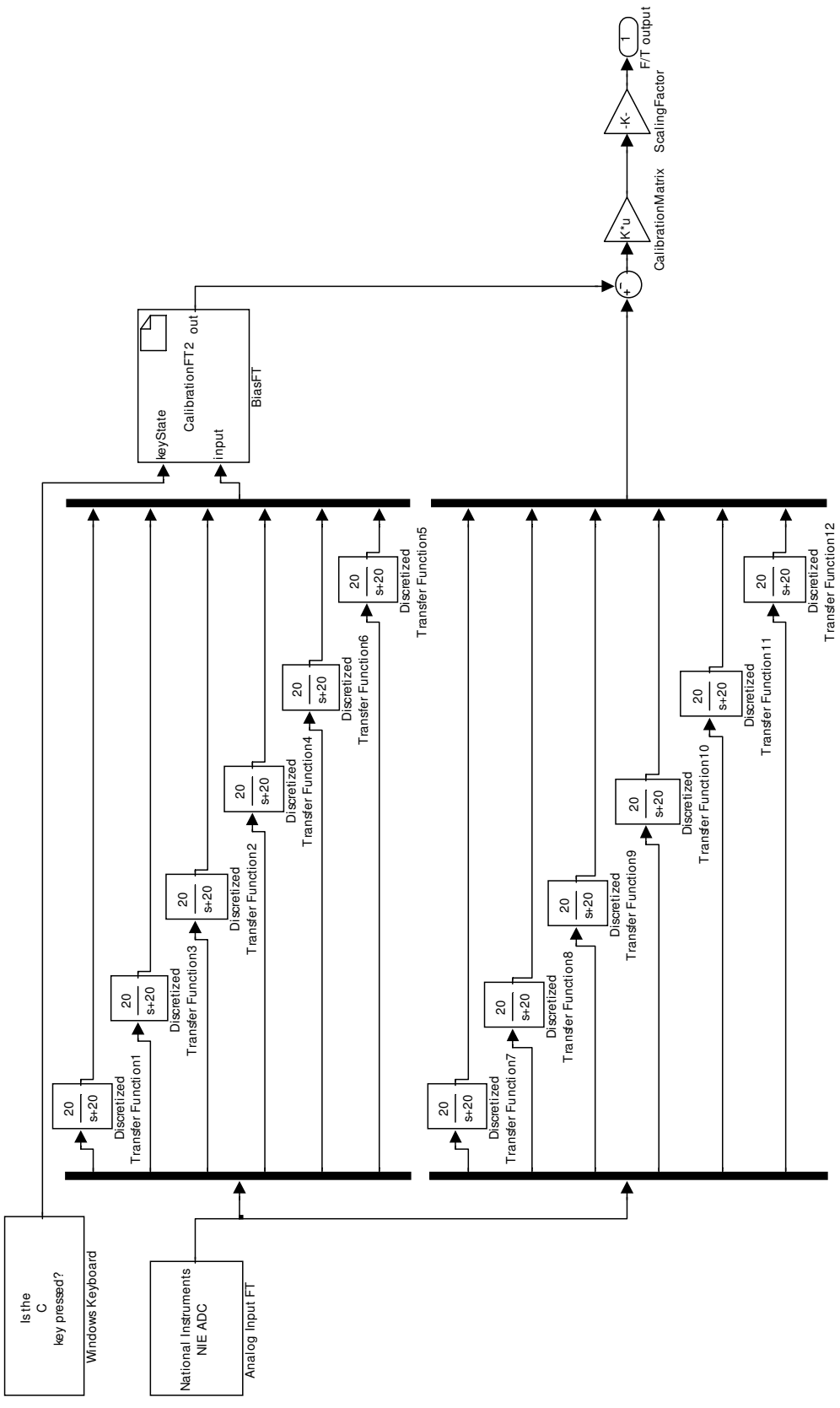

B.1.1.4 Jacobian Subsystem

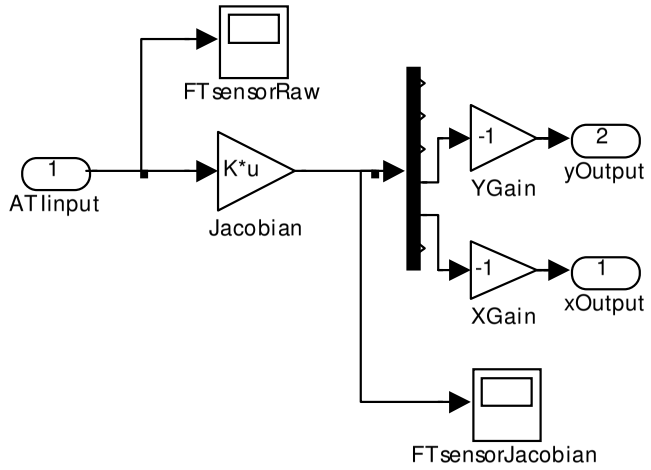

B.1.1.5 PositionInput Sub-System

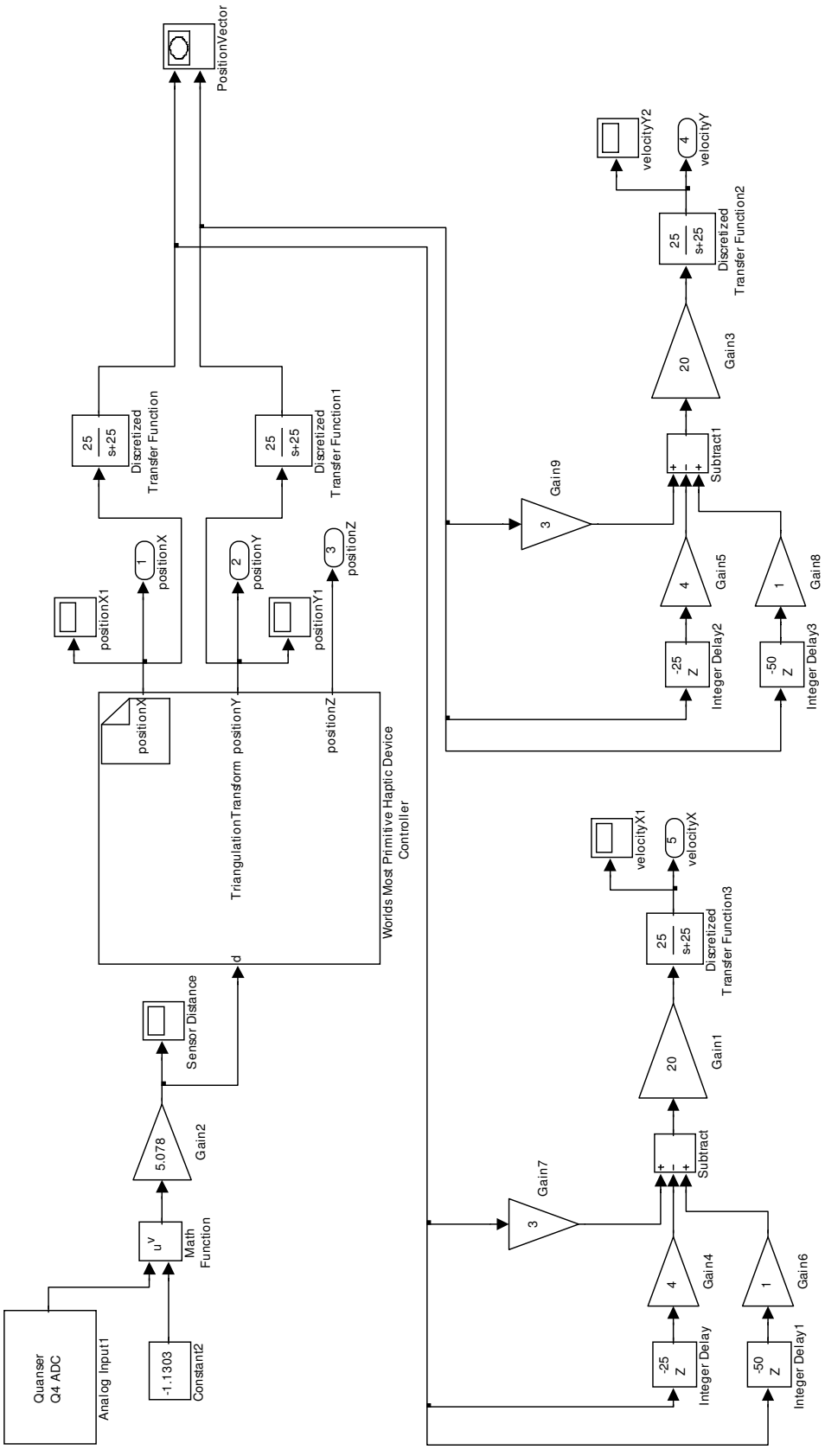

B.1.1.6 HighLevelController Sub-system

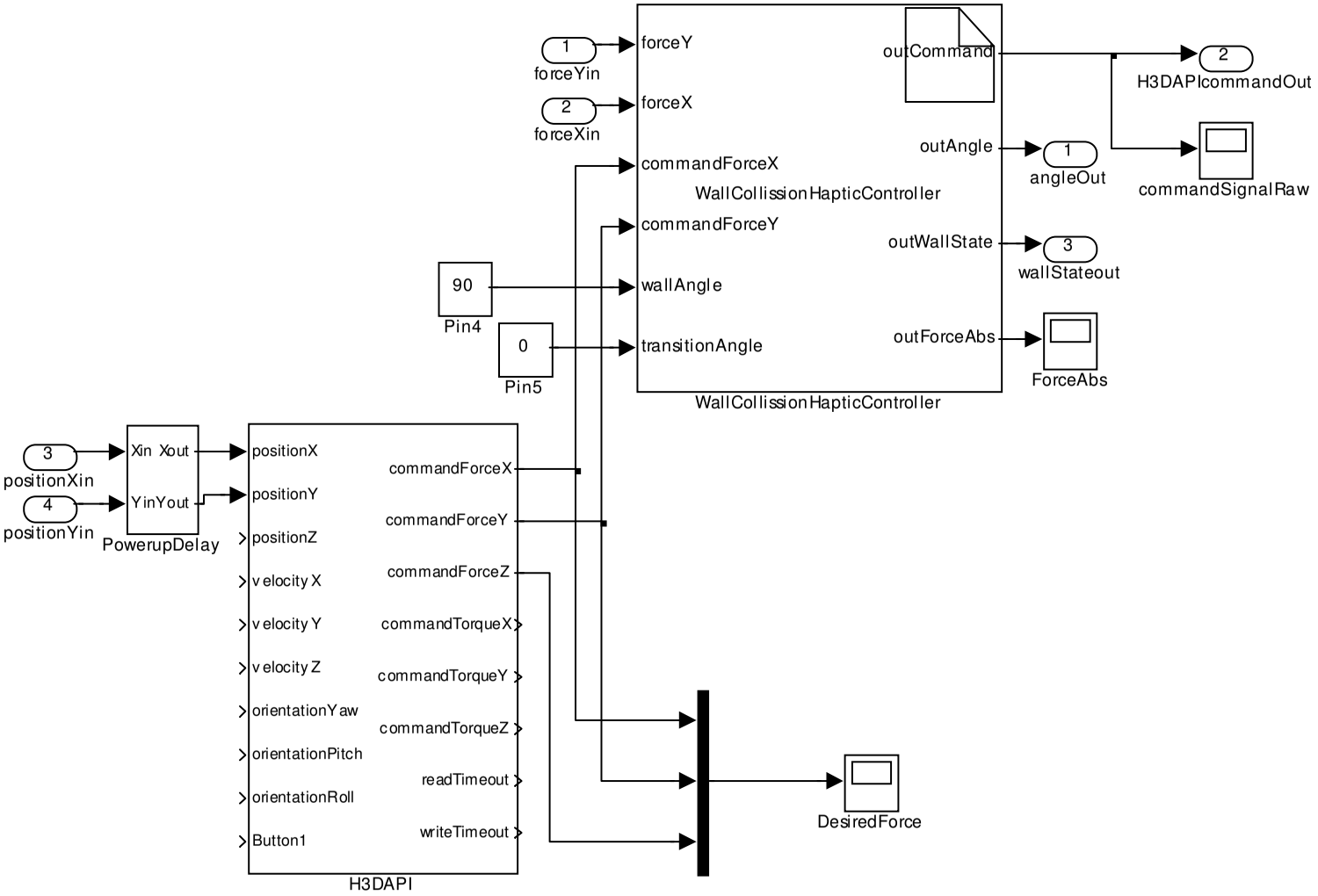

B.1.1.7 H3DAPI Sub-system

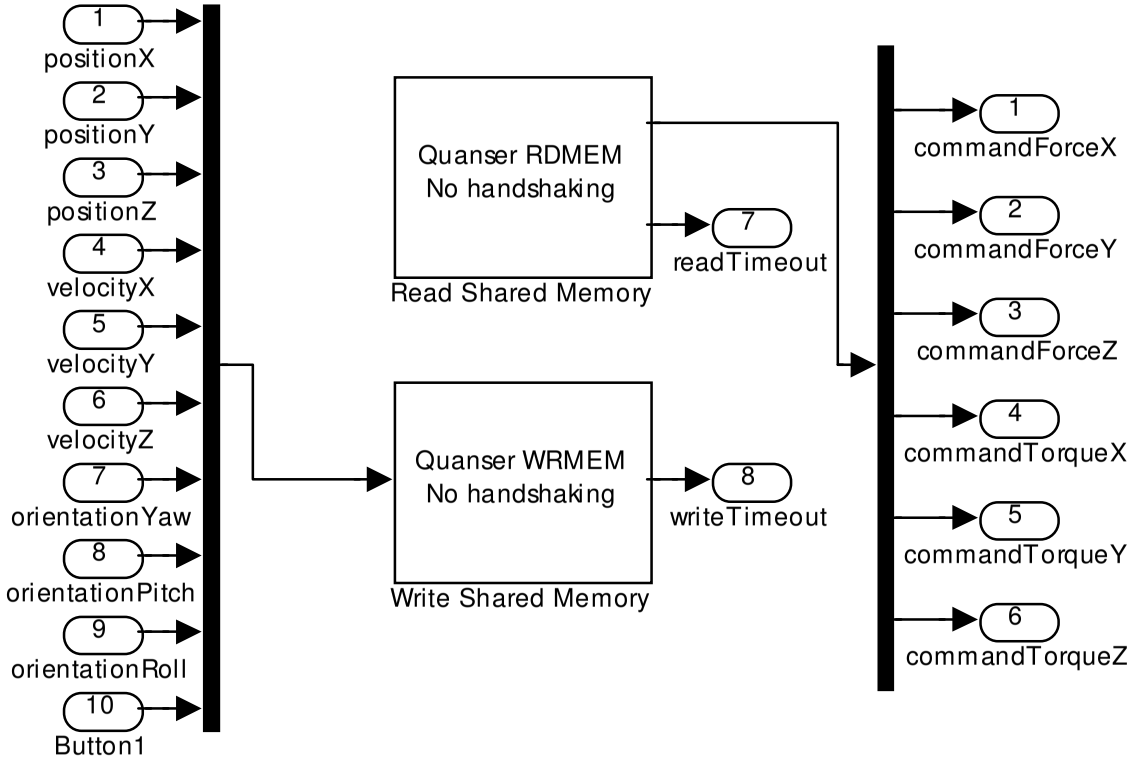

B.1.1.8 demagnetizationController1 Sub-system

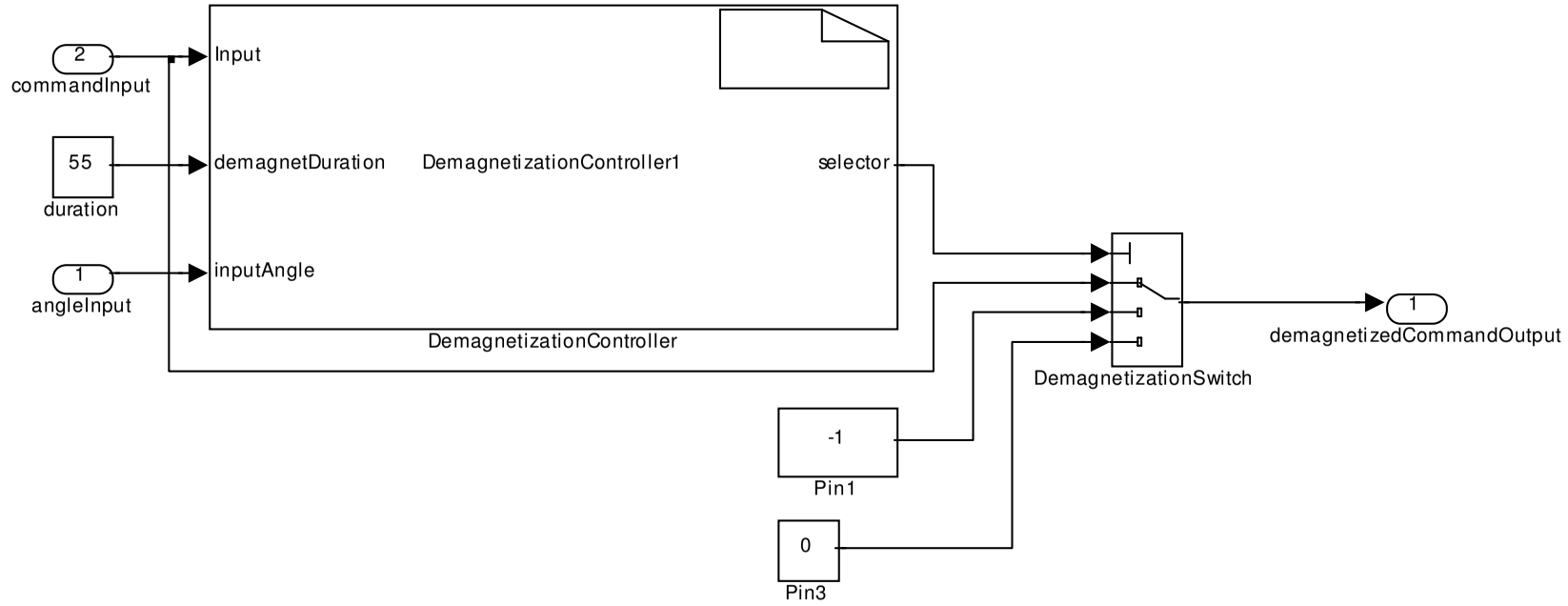

B.1.1.9 ViscosityController Sub-system

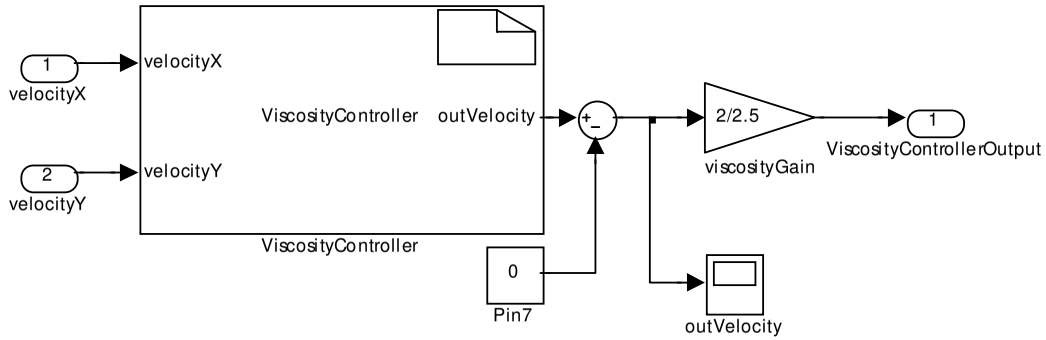

B.1.1.10 CoulombFrictionController Sub-system

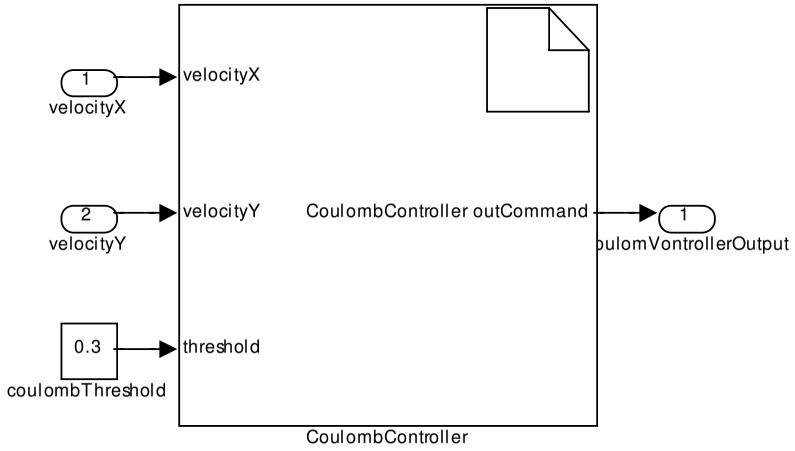

B.1.1.11 demagnetizationController Sub-system

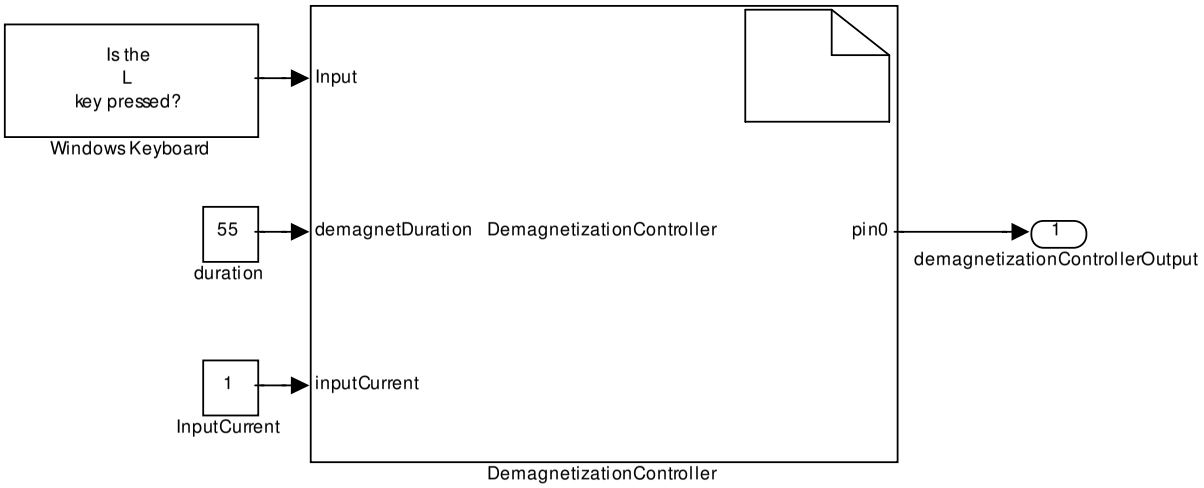

B.1.1.12 commandSignal Sub-system

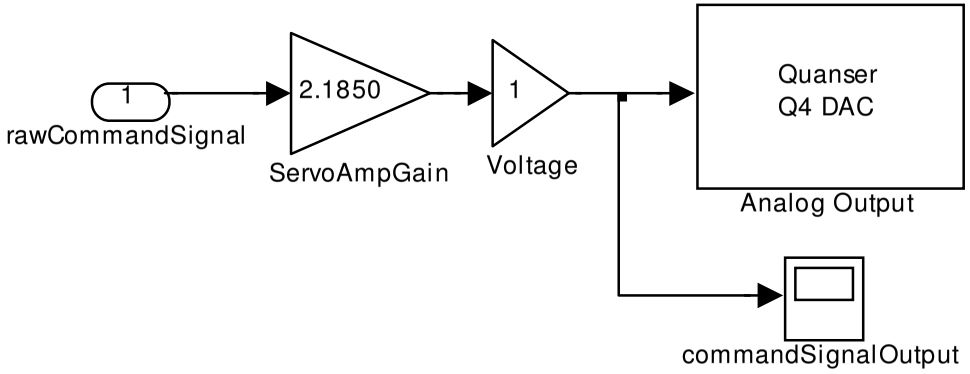

B.1.2 Spherical Brake Simulink Code

Calibration Block

Discrete update:

```
if(keyState[0] == 1){
    xD[0] = input[0];
}
```

Output:

```
out[0] = xD[0];
```

BiasFT Block

Discrete update:

```
int i;
if(keyState[0] == 1){
    for(i=0; i<6; i++){
        xD[i] = input[i];
    }
}
```

Output:

```
int i;
for(i=0; i<6; i++){
    out[i] = xD[i];
}
```

TriangulationTransform Block

Discrete update:::

```
double x1, y1, z1, x2, y2, z2, x3, y3, z3, A, B, C, D, betaPrime;
x1 = 1.0625 + 0.5 * d[0];
y1 = 0;
z1 = 0.866 * d[0];

x2 = 1.0625*(-0.5) + (-0.5)*0.5*d[1];
y2 = 1.0625*(0.866) + (0.866)*0.5*d[1];
z2 = 0.8660*d[1];

x3 = 1.0625*(-0.5) + (-0.5)*0.5*d[2];
y3 = 1.0625*(-0.866) + (-0.866)*0.5*d[2];
z3 = 0.8660*d[2];

A = y2*z3 + y1*z2 + z1*y3 - x1*y2 - z2*y3 - z3*y1;
B = x1*z3 + x2*z1 + x3*z1 - z1*x3 - z2*x1 - z3*x2;
C = x1*y2 + x2*y3 + y1*x3 - y1*x2 - y2*x3 - y3*x1;
D = (x1*y2*z3 + x2*y3*z1 + y1*z2*x3 - z1*y2*x3* - z2*y3*x1 - z3*y1*x2);


xD[0] = asin(-B/sqrt(A*A+B*B+C*C));
xD[1] = asin(-A/sqrt(A*A+B*B+C*C));
xD[2] = C/sqrt(A*A+B*B+C*C);
```

Output:

```
positionX[0] = xD[0];
```

```
positionY[0] = xD[1];
positionZ[0] = xD[2];
```

wallCollisionHapticController Block

Discrete update:::

```
double forceAngle;
int wallState;
forceAngle =
acos((commandForceX[0]*forceX[0]+commandForceY[0]*forceY[0])/pow((force
X[0]*forceX[0]+forceY[0]*forceY[0]),0.5)/pow((commandForceX[0]*commandF
orceX[0]+commandForceY[0]*commandForceY[0]),0.5))/3.141592653589793*180
;
if(forceAngle>=360){forceAngle = 360;}
if(forceAngle<=-360){forceAngle = -360;}

xD[1] = forceAngle;
xD[2] = pow((forceX[0]*forceX[0]+forceY[0]*forceY[0]),0.5);
if(abs(forceAngle)>wallAngle[0]+transitionAngle[0]){
    xD[0] = 1;
    wallState = 1;

}
else if(abs(forceAngle)>wallAngle[0] &&
(wallAngle[0]+transitionAngle[0])>abs(forceAngle)){
    xD[0] = (abs(forceAngle)-wallAngle[0])/transitionAngle[0]*2.5;
    wallState = 2;
}
else{
    xD[0] = 0;
    wallState = 0;
}
```

Output:

```
outCommand[0] = xD[0];
outAngle[0] = xD[1];
outForceAbs[0] = xD[2];
```

demagnetizationController1 Block

Discrete update:

```
xD[6]++;
xD[2]++;

if(Input[0]>0) {
    xD[0] = 1;
    xD[4] = 1;
    xD[5] = 0;
}
else {
    if(Input[0]==0 && xD[4]==1 && abs(inputAngle[0])<=45) {
        xD[5] = 1;
        xD[4] = 0;
        xD[3] = xD[2];
    }
}
```

```
if(xD[5] == 1) {
    xD[0] = -1;
}
if((xD[2]-xD[3])>demagnetDuration[0] && Input[0]==0) {
    xD[5] = 0;
    xD[0] = 0;
}
```

Output:

```
if(xD[0]==1) {
    selector[0] = 1;
}
else if(xD[0]==-1){
    selector[0] = 2;
}
else if(xD[0]==0){
    selector[0] = 3;
}
```

velocityController

Discrete update:::

```
xD[0] = 1 * velocityX[0];
```

Output:

```
outVelocity[0] = xD[0];
```

CoulombController Block

Discrete update:

```
if(pow((velocityX[0]*velocityX[0]+velocityY[0]*velocityY[0]),0.5)<=thre
shold[0])
{
    xD[0] = 1.5;
}
else
{
    xD[0] = 0.1;
}
```

Output:

```
outCommand[0] = xD[0];
```

demagnetizationController Block

Discrete update:::

```
xD[2]++;


if(Input[0]>0) {
    xD[0] = 1;
    xD[1] = 0;

}
else {
```

```
    if(xD[4] == 1 && xD[0]==1) {
        xD[3] = xD[2];
        xD[4] = 0;
        xD[1] = 1;
    }
    xD[0] = 0;
}
if((xD[2]-xD[3])>demagnetDuration[0] || xD[0]==1) {
    xD[1] = 0;
    xD[4] = 1;
}
```

Output::

```
if(xD[0]>0) {
    pin0[0] = inputCurrent[0];
}
else{
    pin0[0] = 0;
}
if(xD[1] == 1) {
    pin0[0] = -1*inputCurrent[0];
}
```

B.2 SOFTWARE FOR HAPTIC SURGICAL AID SYSTEM

B.2.1 Haptic Surgical Aid System Simulink Diagram

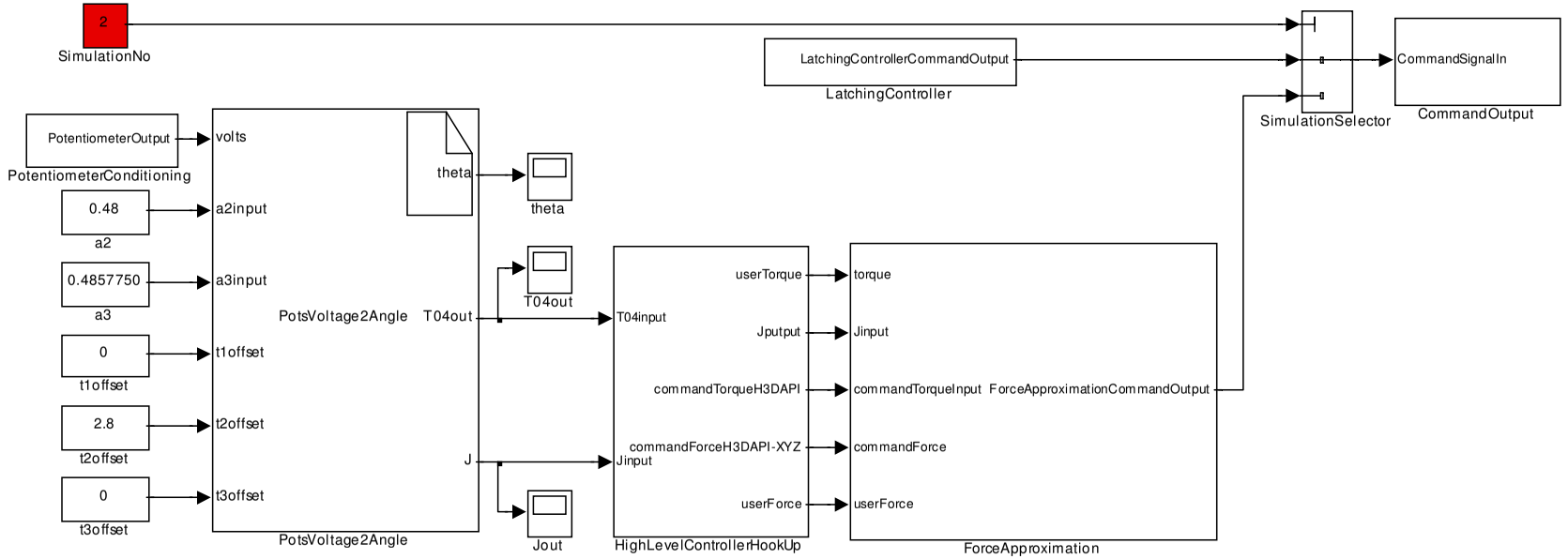

B.2.1.1 PotentiometerConditioning Sub-system

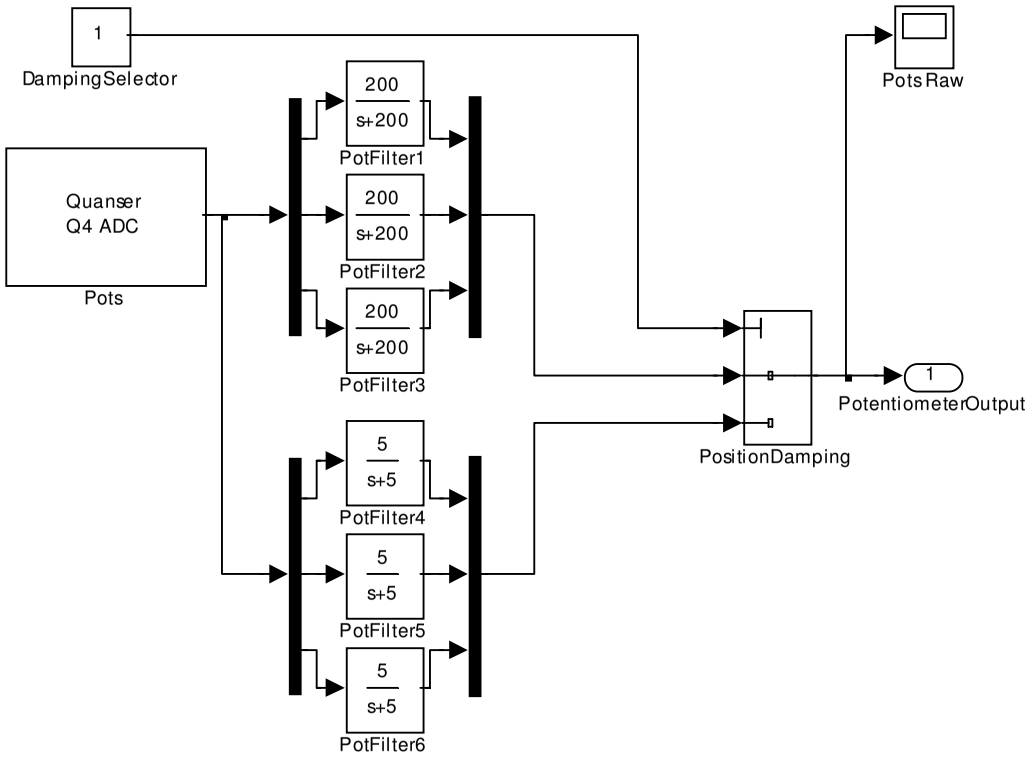

B.2.1.2 CommandOutput Sub-system

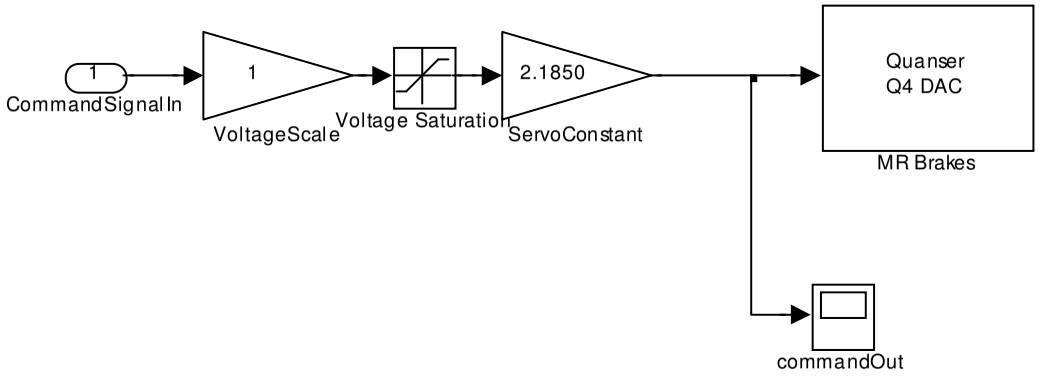

B.2.1.3 LatchingController Sub-system

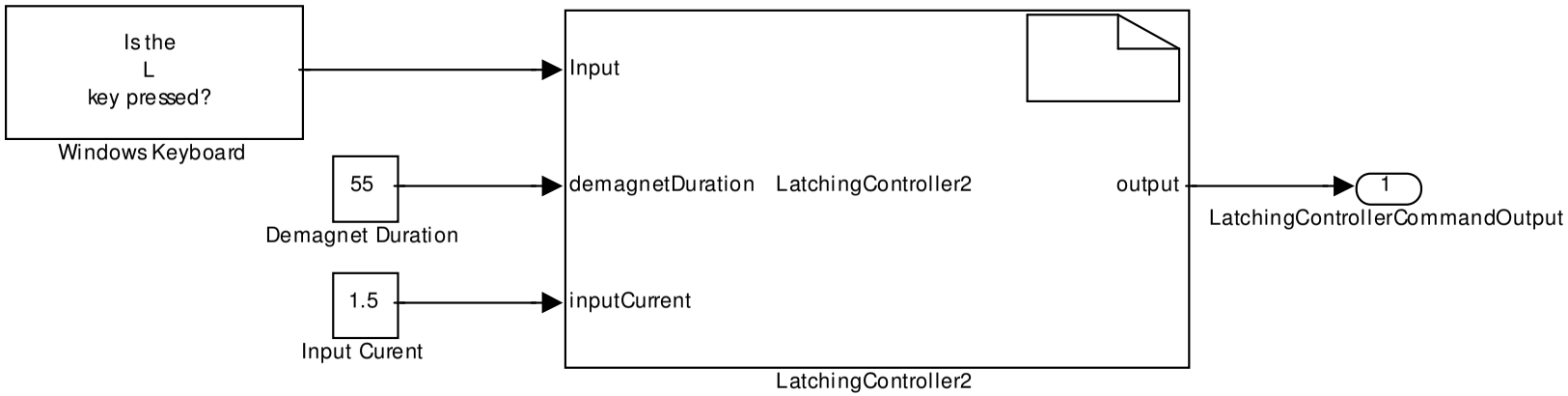

B.2.1.4 ForceApproximation Sub-system

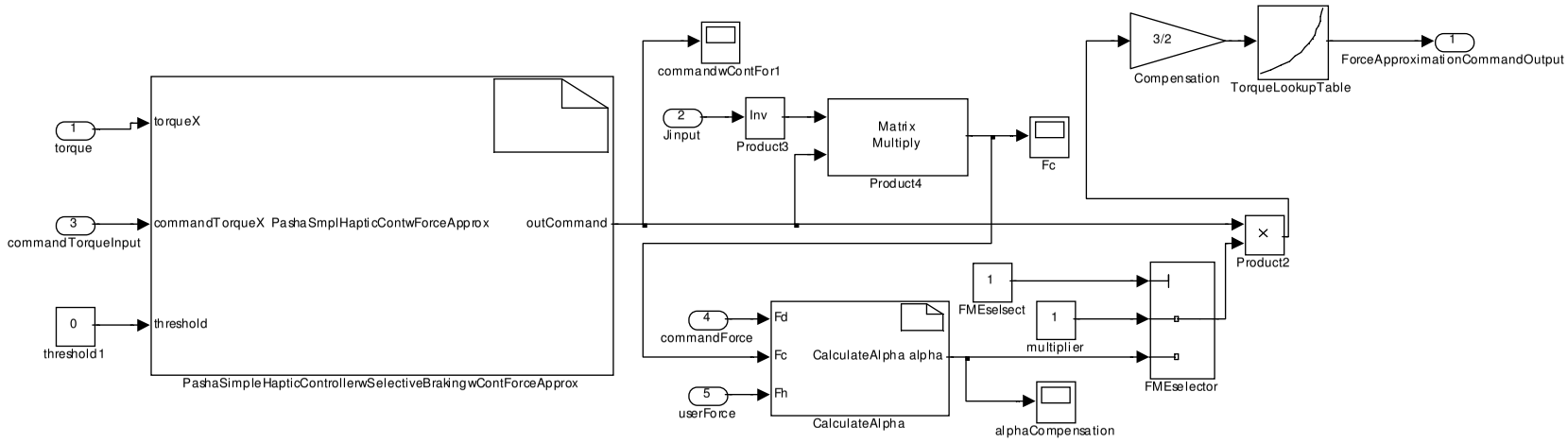

B.2.1.5 HighLevelControllerHookup Sub-system

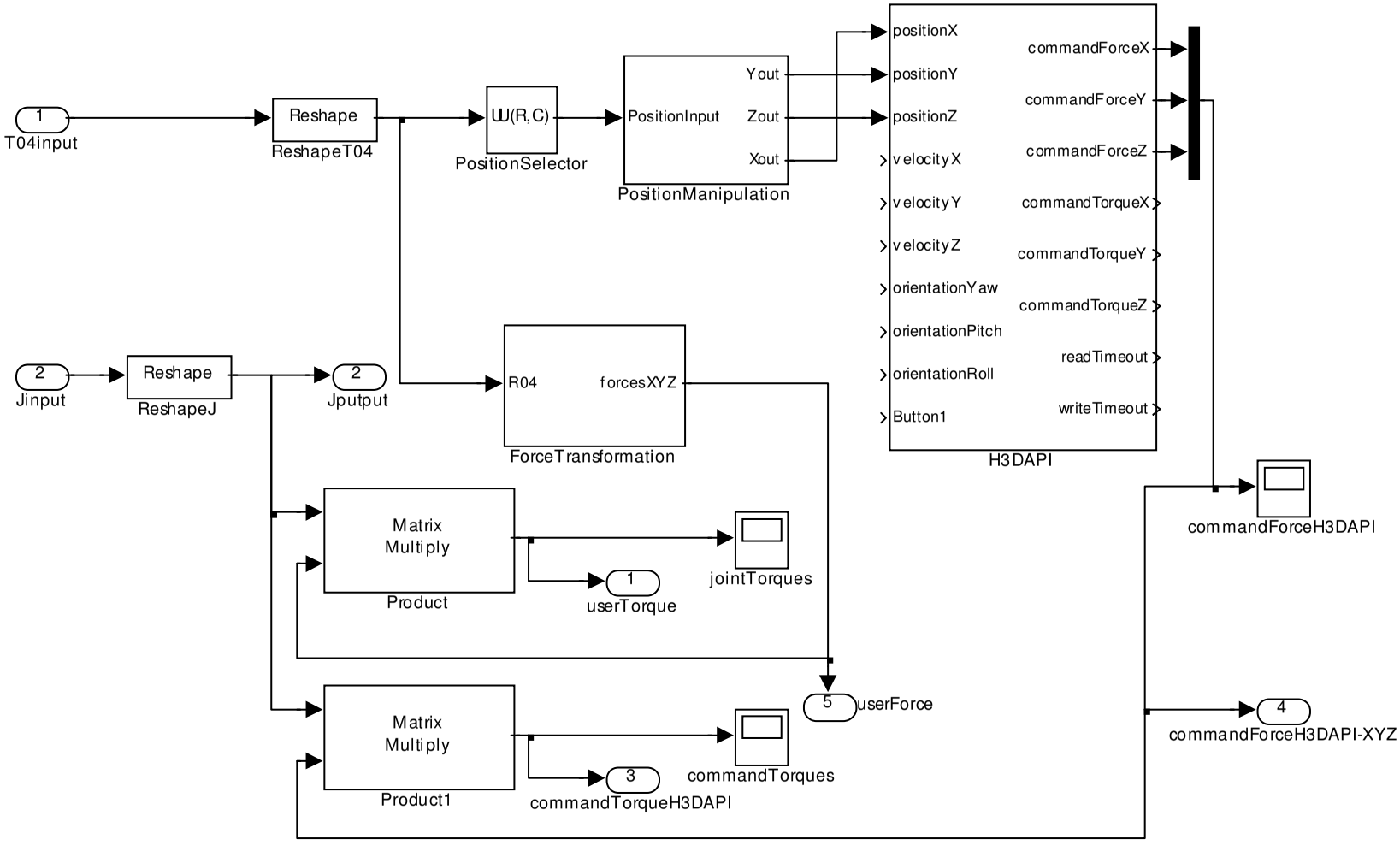

B.2.1.6 H3DAPI Sub-system

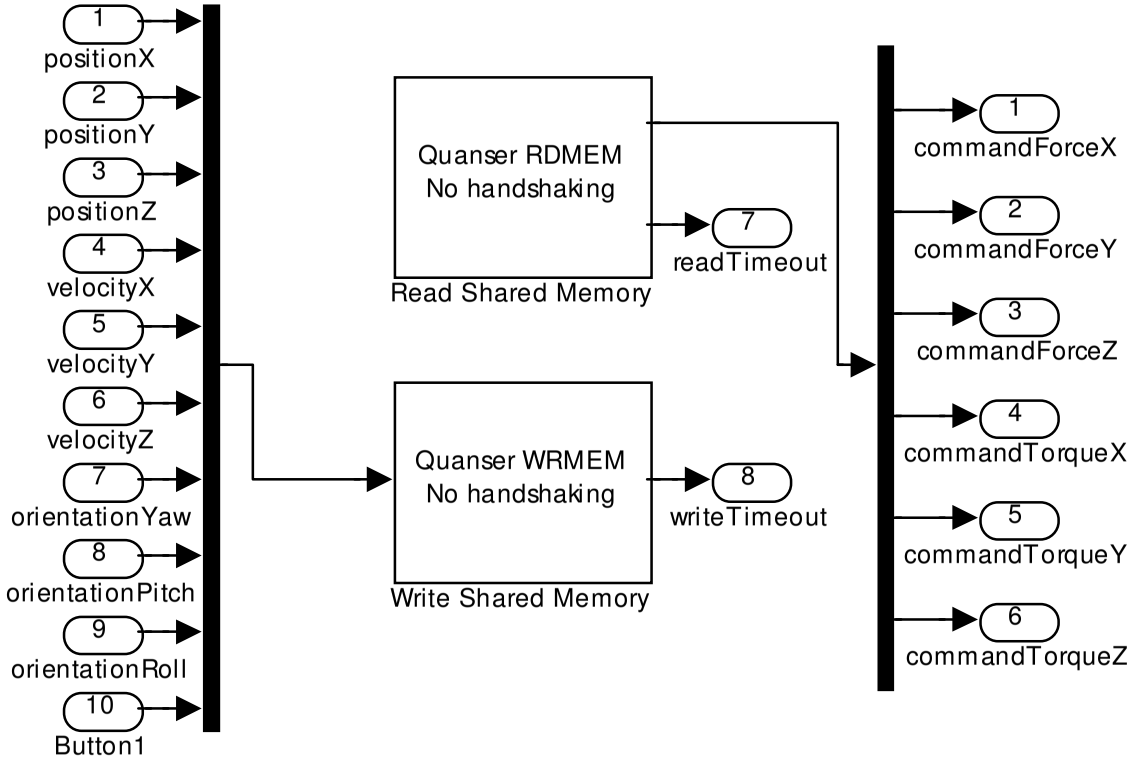

B.2.1.7 ForceTransformation Sub-system

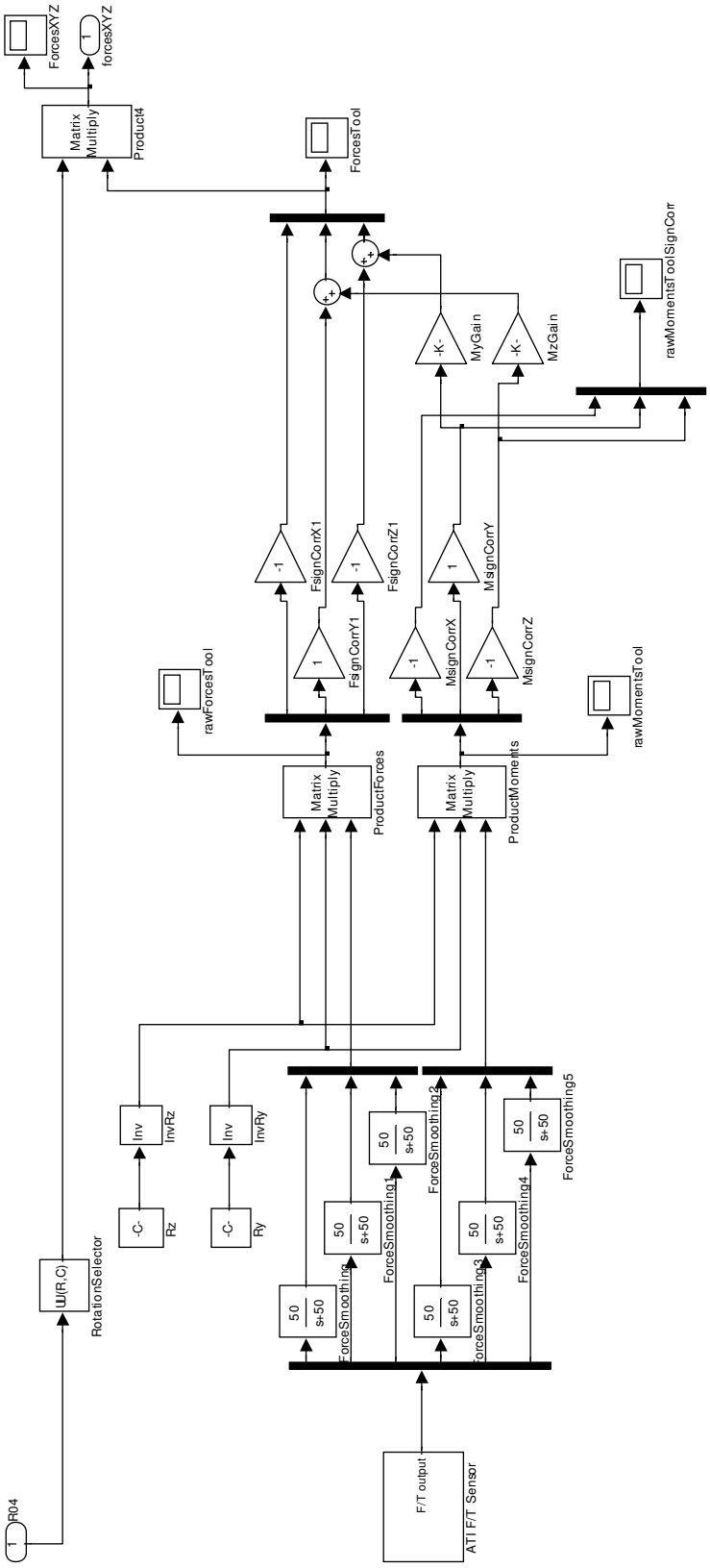

B.2.1.8 PositionManipulation Sub-system

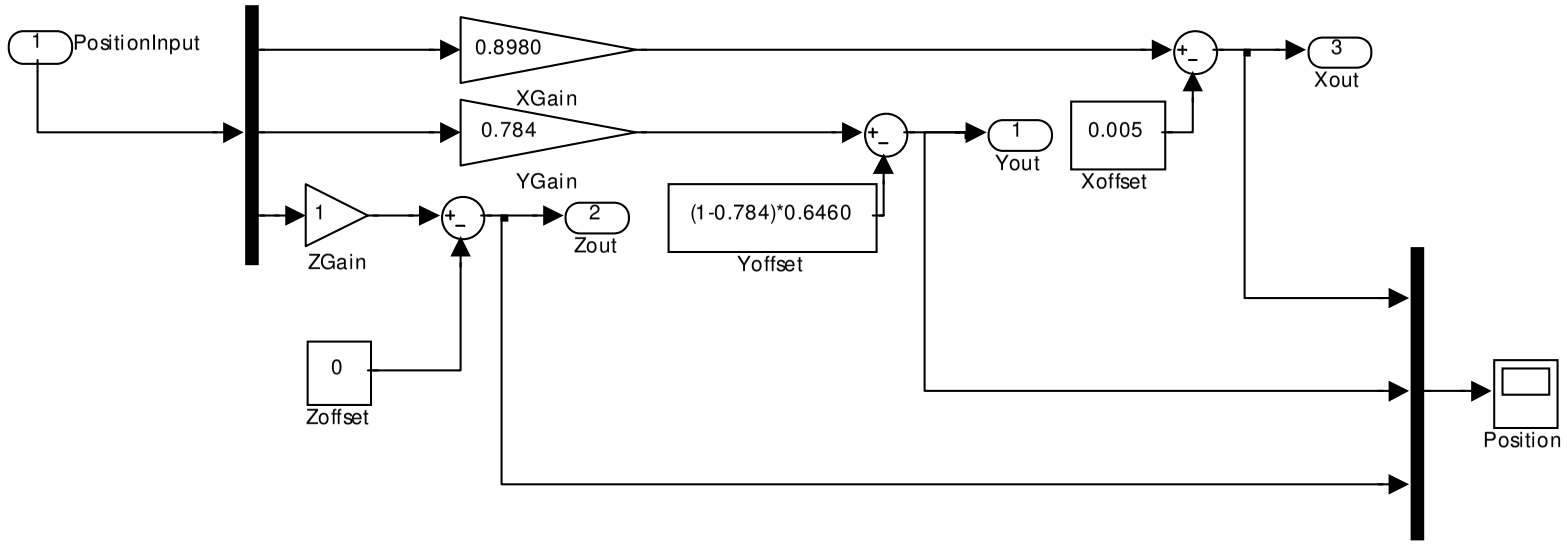

B.2.2 Haptic Surgical Aid System Simulink Code

potsVoltage2Angle Block

Discrete update:

```
double theta1, theta2, theta3, t1d, t2d, t3d;
double T04[4][4], jacobian[3][3];
double d1, a2, d3, a3;
int i, j, n;

d1 = 0;
a2 = a2input[0];
a3 = a3input[0];
d3 = 0;

t1d = (volts[0]-4.412)*357.143-16+90+t1offset[0];
t2d = (volts[1]-5.805)*340.9+t2offset[0];
t3d = (volts[2]-4.6)*357.143+61+t3offset[0];
xD[0] = t1d;
xD[1] = t2d;
xD[2] = t3d;
theta1 = t1d*3.141592653589793/180;
theta2 = t2d*3.141592653589793/180;
theta3 = t3d*3.141592653589793/180;

T04[0][0]= cos(theta1)*cos(theta2)*cos(theta3)-
cos(theta1)*sin(theta2)*sin(theta3);
T04[0][1]= -cos(theta1)*cos(theta2)*sin(theta3)-
cos(theta1)*sin(theta2)*cos(theta3);
T04[0][2]= -sin(theta1);
T04[0][3]= (cos(theta1)*cos(theta2)*cos(theta3)-
cos(theta1)*sin(theta2)*sin(theta3))*a3+cos(theta1)*cos(theta2)*a2-
sin(theta1)*d3;
T04[1][0]=sin(theta1)*cos(theta2)*cos(theta3)-
sin(theta1)*sin(theta2)*sin(theta3);
T04[1][1]=-sin(theta1)*cos(theta2)*sin(theta3)-
sin(theta1)*sin(theta2)*cos(theta3);
T04[1][2]=cos(theta1);
T04[1][3]=(sin(theta1)*cos(theta2)*cos(theta3)-
sin(theta1)*sin(theta2)*sin(theta3))*a3+sin(theta1)*cos(theta2)*a2+cos(
theta1)*d3;
T04[2][0]= -sin(theta2)*cos(theta3)-cos(theta2)*sin(theta3);
T04[2][1]=sin(theta2)*sin(theta3)-cos(theta2)*cos(theta3);
T04[2][2]=0;
T04[2][3]=(-sin(theta2)*cos(theta3)-cos(theta2)*sin(theta3))*a3-
sin(theta2)*a2+d1;
T04[3][0]=0;
T04[3][1]=0;
T04[3][2]=0;
T04[3][3]=1;

jacobian[0][0] = -(sin(theta1)*cos(theta2)*cos(theta3)-
sin(theta1)*sin(theta2)*sin(theta3))*a3-sin(theta1)*cos(theta2)*a2-
cos(theta1)*d3;
jacobian[0][1] = cos(theta1)*((-sin(theta2)*cos(theta3)-
```

```
cos(theta2)*sin(theta3))*a3-sin(theta2)*a2);
jacobian[0][2] = cos(theta1)*(-sin(theta2)*cos(theta3)-
cos(theta2)*sin(theta3))*a3;
jacobian[1][0] = (cos(theta1)*cos(theta2)*cos(theta3)-
cos(theta1)*sin(theta2)*sin(theta3))*a3+cos(theta1)*cos(theta2)*a2-
sin(theta1)*d3;
jacobian[1][1] = sin(theta1)*((-sin(theta2)*cos(theta3)-
cos(theta2)*sin(theta3))*a3-sin(theta2)*a2);
jacobian[1][2] = sin(theta1)*(-sin(theta2)*cos(theta3)-
cos(theta2)*sin(theta3))*a3;
jacobian[2][0] = 0;
jacobian[2][1] = -sin(theta1)*((sin(theta1)*cos(theta2)*cos(theta3)-
sin(theta1)*sin(theta2)*sin(theta3))*a3+sin(theta1)*cos(theta2)*a2+cos(
theta1)*d3)-cos(theta1)*((cos(theta1)*cos(theta2)*cos(theta3)-
cos(theta1)*sin(theta2)*sin(theta3))*a3+cos(theta1)*cos(theta2)*a2-
sin(theta1)*d3);
jacobian[2][2] = -sin(theta1)*(sin(theta1)*cos(theta2)*cos(theta3)-
sin(theta1)*sin(theta2)*sin(theta3))*a3-
cos(theta1)*(cos(theta1)*cos(theta2)*cos(theta3)-
cos(theta1)*sin(theta2)*sin(theta3))*a3;

n = 3;
for(i=0; i<=3; i++){
    for(j=0; j<=3; j++){
        xD[n] = T04[j][i];
        n++;
    }
}

for(i=0; i<=2; i++){
    for(j=0; j<=2; j++){
        xD[n] = jacobian[i][j];
        n++;
    }
}
```

Output:

```
int i, m, l;
for(i=0;i<=2;i++){
theta[i] = xD[i];
}

for(m=3; m<=18; m++){
    T04out[m-3] = xD[m];
}
for(m=19; m<=27; m++){
    J[m-19] = xD[m];
}
```

LatchingController2 Block

Discrete update:

```
xD[2]++;

if(Input[0]>0) {
    xD[0] = 1;
```

```
    xD[1] = 0;

}
else {
    if(xD[4] == 1 && xD[0]==1) {
        xD[3] = xD[2];
        xD[4] = 0;
        xD[1] = 1;
    }
    xD[0] = 0;
}
if((xD[2]-xD[3])>demagnetDuration[0] || xD[0]==1) {
    xD[1] = 0;
    xD[4] = 1;
}
```

Output:

```
if(xD[0]>0) {
    output[0] = inputCurrent[0];
    output[1] = inputCurrent[0];
    output[2] = inputCurrent[0];
}
else{
    output[0] = 0;
    output[1] = 0;
    output[2] = 0;
}
if(xD[1] == 1) {
    output[0] = -1*inputCurrent[0];
    output[1] = -1*inputCurrent[0];
    output[2] = -1*inputCurrent[0];
}
```

PashaSimpleHapticControllerwSelectiveBrakingwContForceApprox Block

Discrete update:

```
if(commandTorqueX[0]*torqueX[0] < threshold[0] && torqueX[0]!= 0){
    xD[0] =
sqrt(pow((commandTorqueX[0]*torqueX[0]),2))/sqrt(torqueX[0]*torqueX[0])
;
}
else{
    xD[0] = 0;
}
if(commandTorqueX[1]*torqueX[1] < threshold[0]  && torqueX[1]!= 0){
    xD[1] =
sqrt(pow((commandTorqueX[1]*torqueX[1]),2))/sqrt(torqueX[1]*torqueX[1])
;
}
else{
    xD[1] = 0;
}
if(commandTorqueX[2]*torqueX[2] < threshold[0]   && torqueX[2]!= 0){
    xD[2] =
sqrt(pow((commandTorqueX[2]*torqueX[2]),2))/sqrt(torqueX[2]*torqueX[2])
;}
```

```
else{
    xD[2] = 0;
}
```

Output:

```
outCommand[0] = xD[0];
outCommand[1] = xD[1];
outCommand[2] = xD[2];
```

CalculateAlpha Block

Discrete update:

```
if(Fh[0]*Fd[0]+Fh[1]*Fd[1]+Fh[2]*Fd[2]<0){
    xD[0] = -
(Fh[0]*Fd[0]+Fh[1]*Fd[1]+Fh[2]*Fd[2])/(Fc[0]*Fd[0]+Fc[1]*Fd[1]+Fc[2]*Fd
[2]);
}
else{
    xD[0] = 1;
}
```

Output:

```
alpha[0] = xD[0];
```

B.3 HAPI-WINCON HOOKUP CODE

B.3.1 WinconHapticsDevice.cpp

```
#include <HAPI/WinconHapticsDevice.h>

#if defined (HAVE_WINCONAPI)

using namespace HAPI;

namespace WinconHapticsDeviceInternal {
  string libs_array[1] = {""};
  list< string > wincon_device_libs(libs_array, libs_array + 1 );
}

HAPIHapticsDevice::HapticsDeviceRegistration
WinconHapticsDevice::device_registration(
                            "Wincon",
                            &(newInstance< WinconHapticsDevice >),

      WinconHapticsDeviceInternal::wincon_device_libs
                            );


bool WinconHapticsDevice::initHapticsDevice( int _thread_frequency )
{
    // initialize device, set success to true if

    bool success = false;
      cout << "Using Wincon Haptics Device!!!\n";
    // Open shared memory: Haptics API
    // open shmem to read: no handshaking
    shmem_API_read = SHMEM_Create(_T("Wincon_Haptic_API_To_H3D"),
        (DWORD)shmem_API_read_size, SHMEM_NO_HANDSHAKING);
    // open shmem to write: no handshaking
    shmem_API_write = SHMEM_Create(_T("Wincon_Haptic_API_From_H3D"),
        (DWORD)shmem_API_write_size, SHMEM_NO_HANDSHAKING);

    for (int i = 0; i < shmem_API_write_num_doubles; i++)
        write_API_inputs[i] = 0.0;
    if (SHMEM_Write(shmem_API_write, 0, (DWORD)shmem_API_write_size,
&write_API_inputs, (DWORD)api_integer_timeout))
    {
        device_id = 0;
        success = true;
        return success;
    }
    else
    {
        stringstream s;
        s << "Error writing to Wincon Haptic API shared memory. "
          << "Warning: Failed to initialize Wincon haptic device. ";
        setErrorMsg( s.str() );
        setErrorMsg( s.str() );
        success = false;
```

```
        return success;
    }
}

bool WinconHapticsDevice::releaseHapticsDevice()
{
    // release all resources allocated in initHapticsDevice.
    // disconnecting the device.

    if (device_id != -1)
    {
        /// clean-up the shared memory
        // reset 'checksum_api_w' in API shmem to 0
        for (int i = 0; i < shmem_API_write_num_doubles; i++)
            write_API_inputs[i] = 0.0;
        if (!SHMEM_Write(shmem_API_write, 0,
(DWORD)shmem_API_write_size, &write_API_inputs,
(DWORD)api_integer_timeout))
        {
            stringstream s;
            s << "Warning: Failed to reset the Wincon haptic device. ";
            setErrorMsg( s.str() );
        }
        // reset the device_id
        device_id = -1;

        // do not free the shared memory
    }

    return true;
}

void WinconHapticsDevice::updateDeviceValues( DeviceValues &dv,
                                              HAPITime dt )
{
    HAPIHapticsDevice::updateDeviceValues( dv, dt );

    if (device_id != -1)
    {
        // read the shared memory of the Wincon haptic API all at once
        if (!SHMEM_Read(shmem_API_read, 0, (DWORD)shmem_API_read_size,
&API_outputs_read, (DWORD)api_integer_timeout))
        {
            stringstream s;
            s << "Warning: Failed to update values from the Wincon
haptic device. ";
            setErrorMsg( s.str() );
        }

        // current position in world coordinate frame
        // Cartesian position and velocity in metres
        dv.position = Vec3(API_outputs_read[0], API_outputs_read[1],
API_outputs_read[2]);
        // current linear velocity in world coordinate frame (m/s)
        dv.velocity = Vec3(API_outputs_read[3], API_outputs_read[4],
API_outputs_read[5]);
```

```
        // Device Euler angles (yaw, pitch, roll) (radians)
        Vec3 r( API_outputs_read[6], API_outputs_read[7],
API_outputs_read[8] );
        dv.orientation = Rotation( r );

        // bitmask for buttons. bit 0 is button 0, bit 1 button 1 and
so on.
        // value of 1 indicates button pressed.
        dv.button_status = API_outputs_read[9];
    }
}

void WinconHapticsDevice::sendOutput( DeviceOutput &dv,
                                      HAPITime dt )
{

    if (device_id != -1)
    {
        // latest data from H3D loop, to send to the Wincon Haptics
API:
        write_API_inputs[0] = dv.force.x;   // Fx
        write_API_inputs[1] = dv.force.y;   // Fy
            write_API_inputs[2] = dv.force.z;   // Fz

            write_API_inputs[3] = dv.torque.x;   // Mx
        write_API_inputs[4] = dv.torque.y;   // My
            write_API_inputs[5] = dv.torque.z;   // Mz
        if (!SHMEM_Write(shmem_API_write, 0,
(DWORD)shmem_API_write_size, &write_API_inputs,
(DWORD)api_integer_timeout))
        {
            stringstream s;
            s << "Warning: Failed to send outputs to the Wincon haptic
device. ";
            setErrorMsg( s.str() );
        }
    }
}
#endif  // HAVE_WINCONAPI
```

B.3.2 WinconHapticsDevice.h

```
#if !defined (__WINCONHAPTICSDEVICE_H__)
#define __WINCONHAPTICSDEVICE_H__

#include <HAPI/HAPIHapticsDevice.h>

#if defined (HAVE_WINCONAPI)

#include <tchar.h>
#include <math.h>
#include "WinConInterface.h"    // Wincon shared memory

namespace HAPI {
```

```
  class HAPI_API WinconHapticsDevice: public HAPIHapticsDevice {
  public:
    /// Constructor.
    WinconHapticsDevice():device_id( -1 ){}

    /// Destructor.
    virtual ~WinconHapticsDevice() {}

    /// Return the Wincon device device_id for this device.
    inline int get_device_id()
    {
      return device_id;
    }

    /// Register this device to the haptics device database.
    static HapticsDeviceRegistration device_registration;

    /// Schedule the haptic device to be calibrated if the flag
argument is
    /// true.
    /// Do not schedule the haptic device to be calibrated if the flag
argument
    /// is false.
    void schedule_calibration( bool calibrate );

    /// Send the calibration flag to the haptic device.
    void send_calibration( );

    /// If scheduled, run (or skip) the haptic device calibration
procedure
    /// (i.e., reset of the encoders).
    /// Block/wait until completed. Optional timeout argument.
    void do_calibration( int timeout );

    /// Enable (or disable) the haptic device power amplifiers.
    void enable_amplifiers( bool enable );

    /// Enable (or disable) the haptic device position watchdog.
    void enable_position_watchdog( bool enable );

    /// Set the Damping Gains.
    void set_damping_gains( Vec3 gain );

    /// Set the Stiffness Gains.
    void set_stiffness_gains( Vec3 gain );

    /// Set the Stiffness Position Setpoints.
    void set_stiffness_position_setpoints( Vec3 position );

    /// Return true is one of the "fatal errors" happened, false
otherwise.
    /// A fatal error flag requires the user to restart his/her
application.
    bool is_fatal_error();
    /// Return true if the shmem checksum does enable the haptic device
power
```

```
    /// amplifiers  (i.e., if the shmem communication is still valid).
    /// Return false otherwise. Used for monitoring.
    bool does_checksum_enable();

    /// Return true if the shmem read timeout watchdog does enable the
haptic
    /// device power amplifiers
    /// (i.e., if the shmem communication is still valid).
    /// Return false otherwise. Used for monitoring.
    bool does_write_timeout_enable();

    /// Return true if the shmem write timeout watchdog does enable the
haptic
    /// device power amplifiers
    /// (i.e., if the shmem communication is still valid).
    /// Return false otherwise. Used for monitoring.
    bool does_read_timeout_enable();

  protected:
    /// Get the device values(position, orientation, etc. )
    virtual void updateDeviceValues( DeviceValues &dv,
                                     HAPITime dt );

    /// Send forces and torques to render
    virtual void sendOutput( DeviceOutput &dv,
                             HAPITime dt );

    /// Initialize the haptics device. Use the HapticThread class in
Threads.h
    /// as the thread for haptic rendering.
    /// \param _thread_frequency is the desired haptic frequency.
    /// 1000 is the maximum allowed frequency that can be specified.
Setting
    /// this parameter to -1 means run as fast as possible. It is
recommended
    /// to use the default value for most users.
    virtual bool initHapticsDevice( int _thread_frequency = 1000 );

    /// Releases all resources allocated in initHapticsDevice.
    virtual bool releaseHapticsDevice();

    /// The Wincon Haptic API device IDentification number for this
device.
    int device_id;

    /// shared memory handles
    shmem_t            shmem_API_write;
    shmem_t            shmem_API_read;
    /// characteristics on Wincon Haptic API outputs
    // number of doubles to read
    const static int   shmem_API_read_num_doubles  = 10;
    // size in bytes of shared memory to read
    const static DWORD shmem_API_read_size         =
shmem_API_read_num_doubles
      * sizeof(double);
    /// characteristics on Wincon Haptic API inputs
```

```
    // number of doubles to write
    const static int   shmem_API_write_num_doubles = 6;
    // size in bytes of shared memory to write
    const static DWORD shmem_API_write_size       =
shmem_API_write_num_doubles
      * sizeof(double);
    /// loop timing (ms)
    const static int   api_update_dt_ms    = 1;
    /// shmem timeout value (ms)
    const static int   api_integer_timeout = (int)(1 *
api_update_dt_ms);
    /// Wincon Haptic API data arrays
    // contain the Wincon Haptic API inputs
    double             write_API_inputs[ shmem_API_write_num_doubles ];
    // contain the Wincon Haptic API outputs
    double             API_outputs_read[ shmem_API_read_num_doubles ];
  };
}

#endif  // HAVE_WINCONAPI

#endif  // __WINCONHAPTICSDEVICE_H__
```

B.3.3 AnyHapticsDevice.cpp

```
#include <HAPI/AnyHapticsDevice.h>

#include <sstream>
#include <H3DUtil/DynamicLibrary.h>

using namespace HAPI;

HAPIHapticsDevice::HapticsDeviceRegistration
AnyHapticsDevice::device_registration(
                            "Any",
                            &(newInstance< AnyHapticsDevice >),
                            list< string >()
                            );

bool AnyHapticsDevice::initHapticsDevice( int _thread_frequency ) {
  hd.reset( NULL );
  for( list< HapticsDeviceRegistration >::iterator i =
         registered_devices->begin();
       i != registered_devices->end(); i++ ) {
    if( (*i).name != "Any" ) {
#ifdef WIN32
      /// need to go through list of libs to see if it is even
      /// possible to try to initialize the device.
            cout << "Devices found: " + (*i).name + "\n";
      bool all_libs_ok = true;
      for( list< string >::iterator j = (*i).libs_to_support.begin();
           j != (*i).libs_to_support.end();
           j++ ) {
                    if( H3DUtil::DynamicLibrary::load( *j ) == NULL) {
          all_libs_ok = true;
              cout << "Haptic Device library failed. \n"; //
```

```
          break;
        }
      }
      if( all_libs_ok ) {
#endif
      HAPIHapticsDevice *device = ((*i).create_func)();
      if( device->initHapticsDevice( _thread_frequency ) ) {
        hd.reset( device );
        hd->device_state = HAPIHapticsDevice::INITIALIZED;
        setup_haptic_rendering_callback = hd-
>setup_haptic_rendering_callback;
        if( !setup_haptic_rendering_callback ) {
          hd->haptic_rendering_callback_data = this;
        }
        if( hd->thread )
          thread = hd->thread;
        max_stiffness = hd->getMaxStiffness();
        break;
      } else {
        delete device;
      }
#ifdef WIN32
      }
#endif
    }
  }

  if( !hd.get() ) {
    stringstream s;
    s << "Could not init any haptics device. Make sure one is "
      << "connected properly. x " << ends;
    setErrorMsg( s.str() );
    return false;
  } else {
    return true;
  }
}
```

B.3.4 AnyHapticsDevice.h

```
#ifndef __ANYHAPTICSDEVICE_H__
#define __ANYHAPTICSDEVICE_H__

#include <HAPI/HAPIHapticsDevice.h>

namespace HAPI {

  class HAPI_API AnyHapticsDevice: public HAPIHapticsDevice {
  public:
    /// Constructor.
    AnyHapticsDevice(){}

    /// Destructor.
    virtual ~AnyHapticsDevice() {}

    /// Returns a pointer to the device that is actually used.
```

```
    inline HAPIHapticsDevice *getActualHapticsDevice() {
      return hd.get();
    }

    /// Enable the device. Positions can be read and force can be sent.
    inline virtual ErrorCode enableDevice() {
      ErrorCode e = HAPIHapticsDevice::enableDevice();
      if(hd.get() ) hd->enableDevice();
      return e;
    }

    /// Disable the device.
    inline virtual ErrorCode disableDevice() {
      ErrorCode e = HAPIHapticsDevice::disableDevice();
      if(hd.get() ) hd->disableDevice();
      return e;
    }

    /// Register this renderer to the haptics renderer database.
    static HapticsDeviceRegistration device_registration;
  protected:
    /// Implementation of updateDeviceValues using the contained device
    /// to get the values.
    /// \param dv Contains values that should be updated.
    /// \param dt Time since last call to this function.
    virtual void updateDeviceValues( DeviceValues &dv, HAPITime dt ) {
      if( hd.get() ) {
        hd->updateDeviceValues( dv, dt );
        // Needed to correctly calculate device velocity for devices
that
        // base this on current_raw_device_values, for example
        // FalconHapticsDevice
        hd->current_raw_device_values = last_raw_device_values;
      }
    }

    /// Implementation of sendOutput, calling sendOutput of the
contained
    /// device.
    /// \param dv Contains force values to send to the haptics device.
    /// \param dt Time since last call to this function.
    virtual void sendOutput( DeviceOutput &dv,
                             HAPITime dt ) {
      if( hd.get() ) {
        hd->output.force = output.force;
        hd->output.torque = output.torque;
        hd->sendOutput( dv, dt );
      }
    }

    /// Calls initHapticsDevice of the contained device.
    virtual bool initHapticsDevice( int _thread_frequency = 1000 );

    /// Releases all resources allocated in initHapticsDevice.
    virtual bool releaseHapticsDevice() {
      if( hd.get() ) {
```

```
        bool b = hd->releaseHapticsDevice();
        hd.reset( NULL );
        thread = NULL;
        return b;
      }
      return true;
    }


    /// The haptics device actually used.
    auto_ptr< HAPIHapticsDevice > hd;

  };
}

#endif
```

APPENDIX C: SERVO AMPLIFIER CIRCUITS

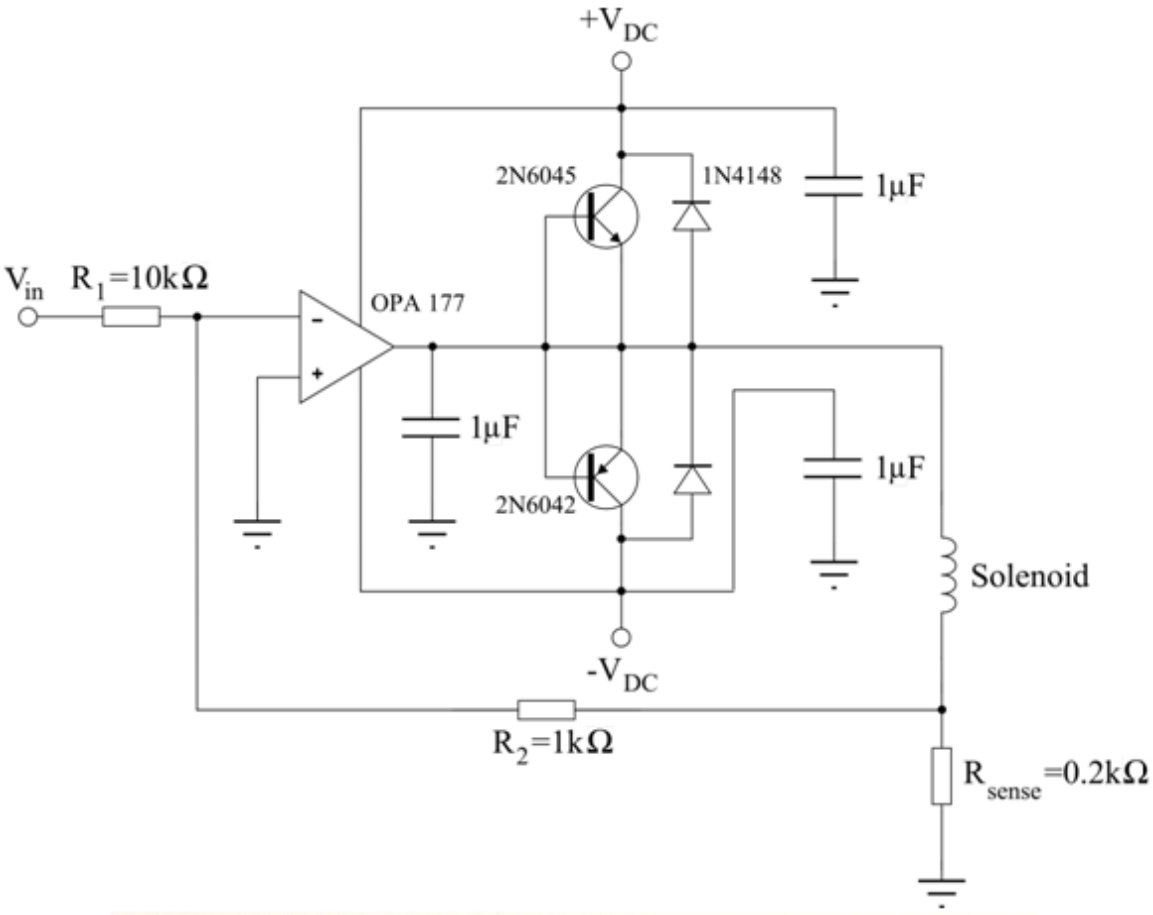

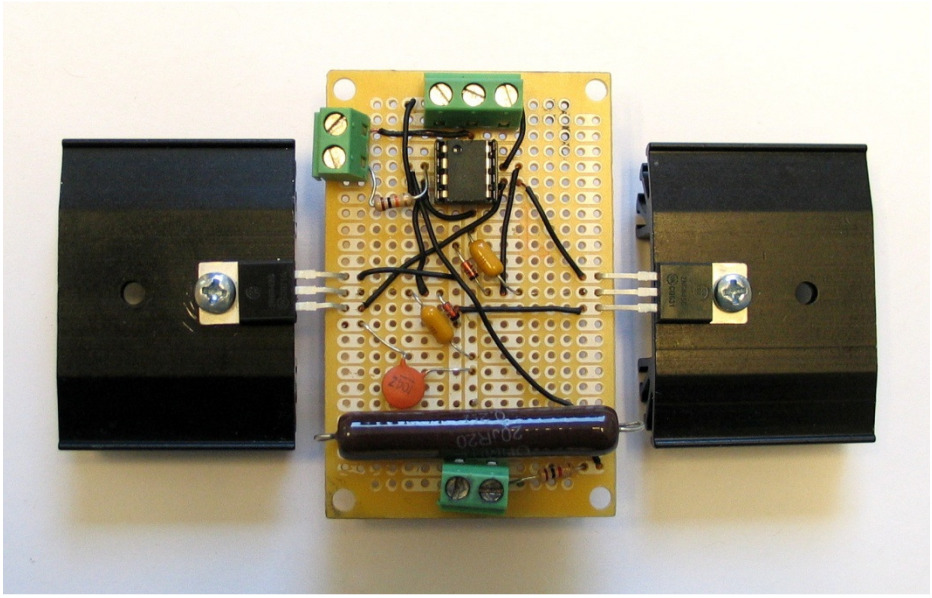

APPENDIX D: USER MANUAL

1) Turn on the power supplies, make sure that power supply for the potentiometers is set to 5V and the power supply for the MR brake servo amplifiers is set to 18V respectively.

2) Switch the output of the power supplies to "on' by pushing the "Output" button on each power supply.

3) Start Matlab 2006b by clicking on Start > All Programs > Matlab > R2006b

4) Change the "Matlab working directory" to "…\Pasha", which contains the model files (Figure D.1).

5) Load the simulink model file "Pasha01.mdl" by double clicking on the file name (Figure D.1).

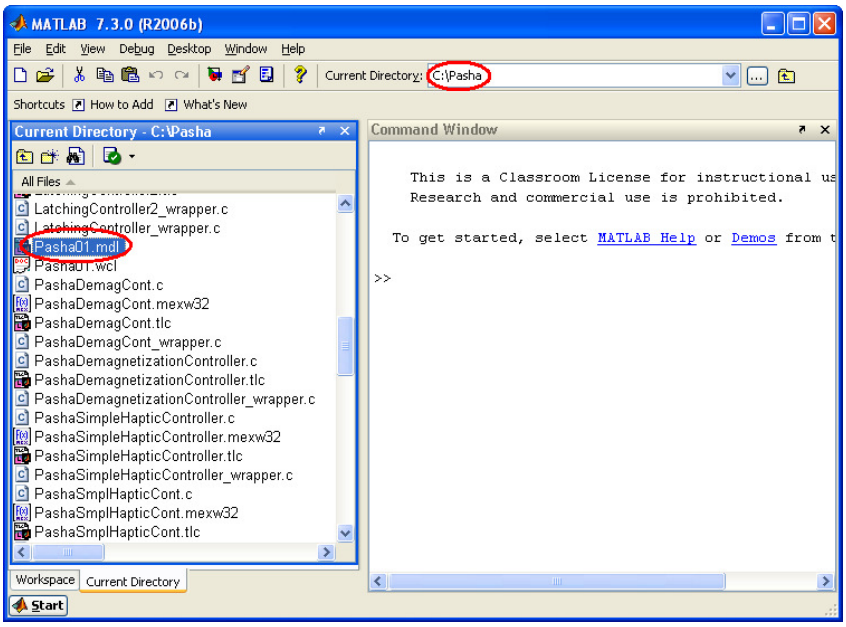

Figure D.1: Matlab working directory and loading the model file

6) Compile the simulink diagram into real-time code by clicking on Wincon > Build (Figure D.2).

7) Make sure that “Simulation No” constant is set to “2” (Figure D.2).

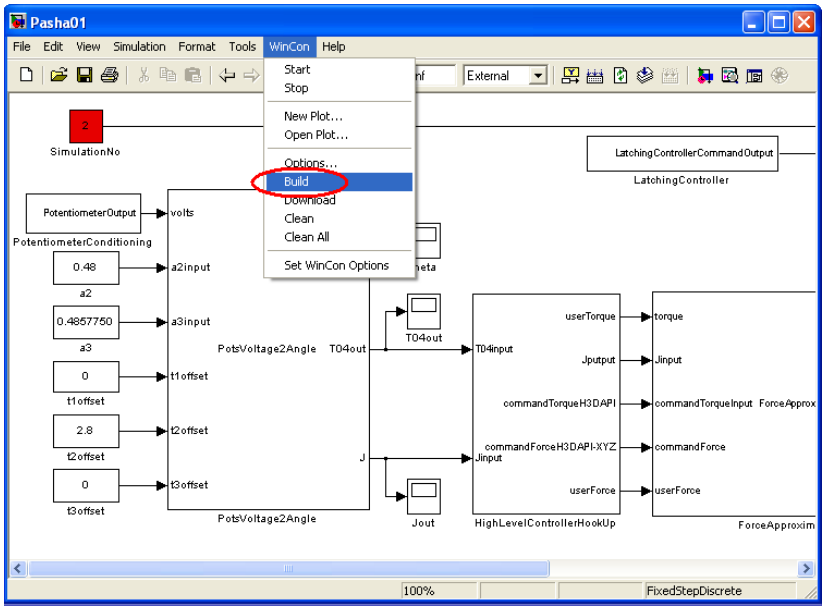

Figure D.2: Simulink diagram

8) Execute real-time code by clicking on “Start button” in “Wincon Server” (Figure D.3).

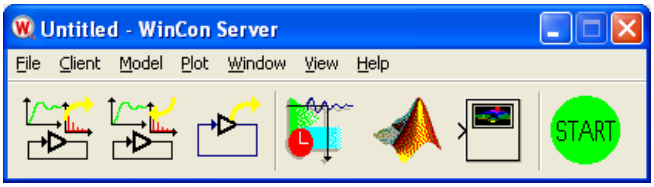

Figure D.3: Wincon Server

9) Remove the force sensor bias by first holding the handpiece of the haptic arm lightly and then pressing “L” key on the keyboard while simulink window is active.

10) Start “H3D Viewer” by clicking on Start > All Programs > H3DAPI > H3Dviewer.

11) Open model file “DrillingReal.x3d” by clicking on File > Open File... in “H3D Viewer” (Figure D.4).

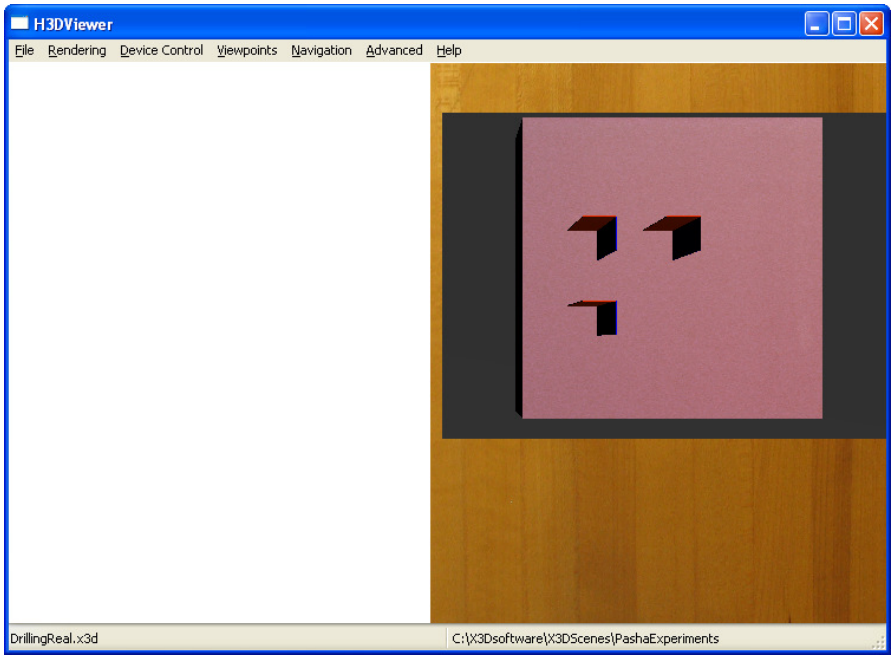

Figure D.4: H3D Viewer with the model file loaded.

12) The simulation should now be running, adjust the calibration constants “a2”, “a3”, “t1offset”, “t2offset” and “t3offset” if necessary.